DESIGN AND DEVELOPMENT OF GRAPHENE BASED METASURFACE FOR X-BAND APPLICATIONS

THESIS SUBMITTED IN PARTIAL FULFILLMENT OF THE REQUIREMENT FOR THE DEGREE OF

MASTER OF ENGINEERING
IN
ELECTRONICS AND TELE-COMMUNICATION ENGINEERING

THESIS SUBMITTED BY

MAHESH DUMPALA

University Registration No: 160217 of 2021-2022

Exam Roll No: M4ETC23004

Class Roll No: 002110702021

UNDER THE SUPERVISION OF

Prof. SAYAN CHATTERJEE

DEPARTMENT OF ELECTRONICS AND TELE-COMMUNICATION ENGINEERING

JADAVPUR UNIVERSITY

KOLKATA – 700032

INDIA

2021 - 2023

FACULTY OF ENGINEERING AND TECHNOLOGY
ELECTRONICS AND TELE-COMMUNICATION ENGINEERING
JADAVPUR UNIVERSITY

CERTIFICATE OF RECOMMENDATION

This is to certify that the thesis entitled "***DESIGN AND DEVELOPMENT OF GRAPHENE BASED METASURFACE FOR X- BAND APPLICATIONS*** " has been carried out by ***MAHESH DUMPALA*** (**University Registration No***: 160217 of 2021-2022*) under my guidance and supervision and be accepted in partial fulfillment of the requirement for awarding the degree of "***MASTER OF ENGINEERING IN ELECTRONICS and TELE COMMUNICATION ENGINEERING***". The research results presented in this thesis have not been included in any other paper submitted for the award of any degree to any other Institute or University.

Sayan Chatterjee 13/6/23

Prof. SAYAN CHATTERJEE

THESIS SUPERVISOR

Dr. Sayan Chatterjee
Professor
Electronics & Telecomm. Engg. Dept.,
Jadavpur University, Kolkata - 700032.

DEPT. OF ELECTRONICS AND TELECOMMUNICATION ENGINEERING
JADAVPUR UNIVERSITY
KOLKATA-700032

Manotosh Biswas 13/06/23

Prof. MANOTOSH BISWAS

MANOTOSH BISWAS
Professor and Head
Electronics & Communication Engineering
University, Kolkata - 32

HEAD OF THE DEPARTMENT

DEPT. OF ELECTRONICS AND
TELE COMMUNICATION ENGINEERING

JADAVPUR UNIVERSITY
KOLKATA-700032

Ardhendu Ghoshal 14/06/23

Prof. ARDHENDU GHOSHAL

DEAN

FACULTY OF ENGINEERING
AND TECHNOLOGY

JADAVPUR UNIVERSITY
KOLKATA-700032

DEAN
Faculty of Engineering & Technology
JADAVPUR UNIVERSITY
KOLKATA-700 032

FACULTY OF ENGINEERING AND TECHNOLOGY

ELECTRONICS AND TELECOMMUNICATION ENGINEERING

JADAVPUR UNIVERSITY

CERTIFICATE OF APPROVAL#

The foregoing THESIS is hereby approved as a creditable study of an Engineering Subject carried out and presented in a manner of satisfactory to warrant its acceptance as a pre-requisite to the DEGREE for which it has been submitted. It is to be understood that by this approval, the undersigned do not necessarily endorse or approve any statement made, opinion expressed or conclusion drawn therein but approve the THESIS only for the purpose for which it has been submitted.

Committee on final examination for the evaluation of the Thesis

_____

(Signature of the Supervisor)

_____

(Signature of the Examiner1)

_____

(Signature of the Examiner2)

only in case the thesis is approved.

FACULTY OF ENGINEERING AND TECHNOLOGY
ELECTRONICS AND TELECOMMUNICATION ENGINEERING
JADAVPUR UNIVERSITY

DECLARATION OF ORIGINALITY AND COMPLIANCE OF ACADEMIC ETHICS

I hereby declare that this thesis contains literature survey and original research work done by the undersigned candidate, as a part of his degree of "***MASTER OF ENGINEERING IN ELECTRONICS AND TELE-COMMUNICATION ENGINEERING***". All information in this document has been obtained and presented in accordance with academic rules and ethical conduct. I also declare that as required by these rules and conduct, I have fully cited and referenced all materials and results that are not original to this work.

Thesis Title

DESIGN AND DEVELOPMENT OF GRAPHENE BASED METASURFACE FOR X- BAND APPLICATIONS

MAHESH DUMPALA

University Registration No: 160217 of 2021-2022

Exam Roll No: M4ETC23004

Class Roll No: 002110702021

DEPT. OF ELECTRONICS AND TELECOMMUNICATION ENGINEERING

JADAVPUR UNIVERSITY

KOLKATA – 700032

INDIA

Date: 13/06/23

(MAHESH DUMPALA)

ACKNOWLEDGEMENT

Firstly, I wish to take this opportunity to thank my Master's supervisor Prof. Sayan Chatterjee and acknowledge the deep impact he has had in cultivating within me the interest and curiosity that I have developed towards the Nanotechnology, especially on graphene. His patience, the immense knowledge he shares with us and the relationship he has with all his students clearly brings out the best inthem. I am very thankful that I have been able to do my Master's thesis under the guidance of such an able and well established professor.

I would like to thank Prof. Bhaskar Gupta for all his comments and discussions which have very often helped clear many of my doubts and helped me look at things from a different perspective. I wish to express my gratitude to the head of the department Prof. Manotosh Biswas and other faculty members for always extending their helping hand whenever needed. I also thank Mr. Ashoke Kr. Mondal, Sr. Technical Assistant, Mr.Probir Mondal, Sr. Technical Assistant, IC center helping and encourage me in the graphene making process.

This thesis would not have been complete without the help and cooperation of Soham Ghosh, all my other seniors and classmates of JU Microwave specialization who took the time and effort to help me immensely with all my fabrications and indulge in very knowledgeable discourse which helped me learn a plethora of things regarding my subject that I was previously unaware of. I would also like to thank Dr. Chandan Kumar Ghosh, Assistance Professor and his research scholar Panchanan Sahoo of School of Material science and Nanotechnology, Jadavpur University for sharing their knowledge, clearing my doubts whenever required and helped in testing part of my work.

Lastly, but most importantly, I would like to thank my father, mother, wife, all my other family members and friends for encouraging me to pursue the subject I love and for their constant and unwavering faith in my abilities. Without their support, I would definitely not be where I am today.

Date: 13/06/23

(MAHESH DUMPALA)

ABSTRACT

This thesis mainly focused on the design and development of graphene based metasurface and production of graphene with characterization. In present existing systems, the copper was conventional radiating material which was mostly used; it has some disadvantages like oxidation, low working temperature range, circuit instability, dielectric problems, not that much flexible and less conductivity. The demand for miniaturization, energy efficiency, flexibility, long life, bio-degradable and non-toxicity properties of device were now given high priority in research to give sustainable life to future generations.

The above most of the goals were full filled by Nano-materials, mainly using graphene which has excellent electrical and thermal conductivity, ballistic massless transport, excessive electron mobility, dynamic tuneability by applying chemical potential, zero band gap structure, supports spoof surface plasma polariton, transparency, mechanical robustness and flexibility, strongest and thinnest material, large surface area, high melting point and light weight material. So making of the graphene in our lab using Chemical Vapour Deposition and characterized using FTIR spectroscopy was done and got results that shows C=C bonding along with some other bonds on substrate which denote alkane, carbon dioxide, alcohol, Cyclic alkene and ester compounds were grown on Substrates and finally concluded that graphene was not formed on any substrate. The design and fabrication of a graphene based metasurface with four leg Jerusalem shape was done and the resonance frequency 10.16GHz result was matched with reduced band width.

CONTENTS

List of Figures

List of Tables

CHAPTER -1
INRODUCTION

1.1 Chapter overview

This chapter presented the brief history, definition, basic properties and applications of Nano materials (section 1.2). In section 1.3 mainly dealt with the definition of graphene, special characteristics and applications of graphene. In section 1.4 focused on the motivation behind the thesis and finally in section 1.5 gave the details of organisation of thesis.

1.2 Introduction to Nano materials

1.2.1 History of Nano materials

Nano-materials (NMs) were used for the first time in the fourth century AD with the iconic Lycurgus cup, which was composed of dichroic glass, as shown in fig. 1.1[1]. It displayed red in light that was transmitted (because to the gold nanoparticle) and green in light that reflected (thanks to the silver nanoparticle). Later, it became clear that NMs were utilized in 18th-century Tipu Sultan's sward (made with wootz steel) and Damascus swards (made with Au & Ag) [2]. Michel Faraday investigated various gold solutions in 1857 and came to the conclusion that the diverse hues were caused by various gold particle sizes [3]. Gustav Mie outlined the optical characteristics of gold nanoparticles in 1908, and subsequent mie theory describes how homogenous spherical nanoparticles deflect electromagnetic waves [4].

Fig 1.1: [1] A) Green colour due to reflected light from silver, B) Red colour due to transmitted light from gold.

When Rechard Zsigmondy used a microscope to calculate the dimension of gold colloidal particles in 1925, he coined the term "Nanometre" [5]. The eminent scientist Rechard Feynman initially proposed the concept of nanotechnology during his 1959 address, "There is a plenty of room at the bottom," delivered at the American-Physical-Society meeting at the California Institute of Technology [6]. He described the potential for producing tiny devices and items with atomic precision. Taniguchi, a Japanese physicist, coined the word "nanotechnology" for the first time in 1974 [7]. The primary processes involved in nanotechnology involve the separation, consolidation, and manipulation of materials by a single atom or molecule. At the IBM Zurich Research Laboratory, Gerd Binning and Heinrich Rohrer developed the scanning tunnelling microscope, which gave rise to modern nanotechnology [8].

1.2.2 Definition, properties and application areas of Nano materials

Sustainable development was that meet the needs of the present without harming or compromising the ability of future generations to meet their own needs, to achieve this goal, technologies evolving day to day. Since recent developments in material theory and manufacturing technology in NMs which had at least one dimension in between 1-100nm with size dependent variation in properties, i.e with their special properties like small in size (Nano scale), speed of operation, low operating power, highly-integration, bio degradable and environmental friendly (some of NMs) this led to use of NMs in various fields such as electronics, communication, physics, chemistry, energy storage – production – conversion, agricultural productivity enhancement, water treatment and remediation, disease diagnosis and screening, drug delivery systems, health monitoring, food processing and storage, air pollution remediation, construction and biology of modern science. There were so many Nano materials found in this world after invention of scanning tunnelling microscope. One of such a material was graphene.

1.3 Definition, special characteristics and applications of graphene

Graphene was a first 2D-documented honeycomb shaped mono layered SP^2 hybridized semi metal natured carbon allotrope material discovered by using method of scotch tape from graphite by Novoselov and AK Giem [9-11] in MIT lab in 2004 for which they got Nobel Prize in 2010. This discovery led scientist to open new area of research in 2D Nano materials which was a remarkable revolution in electronics.

The highlights of the graphene was that, it had excellent electrical and thermal conductivity, ballistic massless transport, excessive electron mobility, dynamic tuneability by applying chemical potential, zero band gap structure, supports spoof surface plasma polariton [SSPP], transparency, mechanical robustness and flexibility, strongest and thinnest material, large surface area, high melting point and light weight material led to prominent applications in different fields of science.

Due to its high carrier mobility at room temperature it was used in making of transistors [12] which exhibits high cut off frequencies. It had best electrical-mechanical-optical properties led to application as a photocatalyste [13-15]. It was used in solar cells, storage batteries and super capacitors as it had high surface area [16-17]. As it was Nano material i.e small in size it's used as membrane in water filter technology [18]. It had excellent thermal-electrical-optical properties, so it was used in biosensors [19, 20]. Due to its special properties like high conductivity and biocompatible nature it was used in drug delivery system [21]. With low toxicity and strong absorbance at near infrared property of graphene, it was used in photo thermal therapy and imaging applications [22]. Duo to its thinnest and anti-corrosion property it could be used in coating and paintings [23]. Graphene had best conductance duo to its high carrier mobility and also had flexibility, transparency and Spoof Surface Plasmon Polariton (SSPP) properties, it has different frequency applications in microwave-frequency range and in terahertz frequency range. In microwave-frequency range, like Wearable antennas [24, 25], RFID antennas [26, 27], Sensors [28], Filtering power divider [29], Attenuators [30], Absorbers [31] and EMI shielding [32]. In terahertz range also it used as Absorbers [33, 34], Antenna [35-38], Filters [39, 40], FSS [41-43] and metasurfaces [44-46].

1.4 Motivation

As the world travelled toward the most advanced technologies like 6G communications and internet of everything with applications in civil, military, air traffic control, maritime vessel traffic control, defence tracking, satellite communication and weather monitoring in X-band, as the X-band had advantages like lower chance for atmospheric interference, great spectral efficiency, handle with high power, less rain fading and reducing antenna size. These technologies frequently used Frequency selective surfaces and metasurfaces to achieve goals like high coverage area, high efficiency, eco-friendly, bio

degradable, low weight, heat dissipation capability, low power consumption, dynamic controllability. The copper was generally a conventional radiating material which was mostly used in above applications but it had some disadvantages like oxidation, low working temperature range, circuit instability, dielectric problems, not that much flexible and less conductivity compared to graphene. There were also other conventional materials like gold and silver which exhibit plasmon property with higher plasma frequency without tuneability. Therefore graphene selected as material to overcome above disadvantages, and try to manufacture graphene using chemical vapour deposition method and designed a graphene based metasurface for X-band applications.

1.5 Outline of thesis

This introduction chapter discussed the brief history, definition, features and applications of both Nano materials and graphene along with motivation behind the work. In chapter 2 discussed the some literature reviews regarding history & basics of graphene and frequency based applications of graphene from microwave to terahertz. Chapter 3 presented the detail background of graphene i.e its basic structure, kubo formula for graphene conductivity, preparation of graphene, characterization of graphene and finally discuss about metasurfaces. Chapter 4 was about making of graphene using chemical vapour deposition and FTIR spectrum of graphene grown samples. Chapter 5 was about simulation of graphene based X-band metasurface and making metasurface with results. The conclusion comments along with future scope of this work presented in chapter 6.

CHAPTER -2
LITERATURE REVIEW

2.1 Chapter overview

This chapter discussed about the brief history of graphene in section 2.2. In section 2.3 explains the general applications of graphene. Section 2.4 emphasised the concepts of basics of Plasmon in metals and surface waves and Spoof Surface Plasmon Polariton concepts. In section 2.5 dealt with the applications of graphene from microwave frequency to terahertz range in section.

2.2 Brief history of graphene

The existence of purely two-dimensional (2D) Nano-crystals was disputed by Landau and Peierls due to their thermodynamic instability [47]. According to their idea, thermal variations in flat dimensional crystal structures should cause atom displacements that were similar to interatomic lengths at any limited temperature. Mermin [48] later expanded the thesis, and his findings from experiments provide a compelling counter argument. In fact, thin films lost their ability to melt quickly as their thickness declines, and at an average thickness of tens of atomic layers, they start to breakdown or split into islands [49, 50]. Due to this, atomic single layers were only ever fully understood as a component of larger three-dimensional structures, typically produced epitaxially on the top of single crystals with complementary crystal lattices. Before 2004, it was believed that 2D materials did not exist since they lacked a 3D foundation.

As semiconductor industry come to end of the performance improvement, with background knowledge of Nano materials like fullerenes, carbon Nano tubes, K.S. Novoselov and AK Giem of Russian scientists invented the few layered graphene (FLG) by repeatedly peeling of carbon layers from structurally arranged pyrolytic graphite surface [9] in 2004. With this invention they designed a field effect transistor and found that carrier mobility of FLG was depend on applied gate voltage so that the conductivity also varied. They also observed that small overlap between valance and conduction band of this type of thin layered (2D materials) metal structures which depends on the electric field doping. Following fig 2.1 shows atomic force microscope and scanning electron beam microscope images of FLG and designed field effect transistor on oxidised SI wafer. In 2005 K.S. Novoselov et.al

investigated the possibility of stability of 5 different single layered 2D crystals and found that they exhibit high crystal quality under ambient conditions [10]. In the same year the authors [11] found that the conductivity in the graphene due to massless Dirac fermions with effective speed of 10^6 m/s and also linear dispersion relation in band diagram.

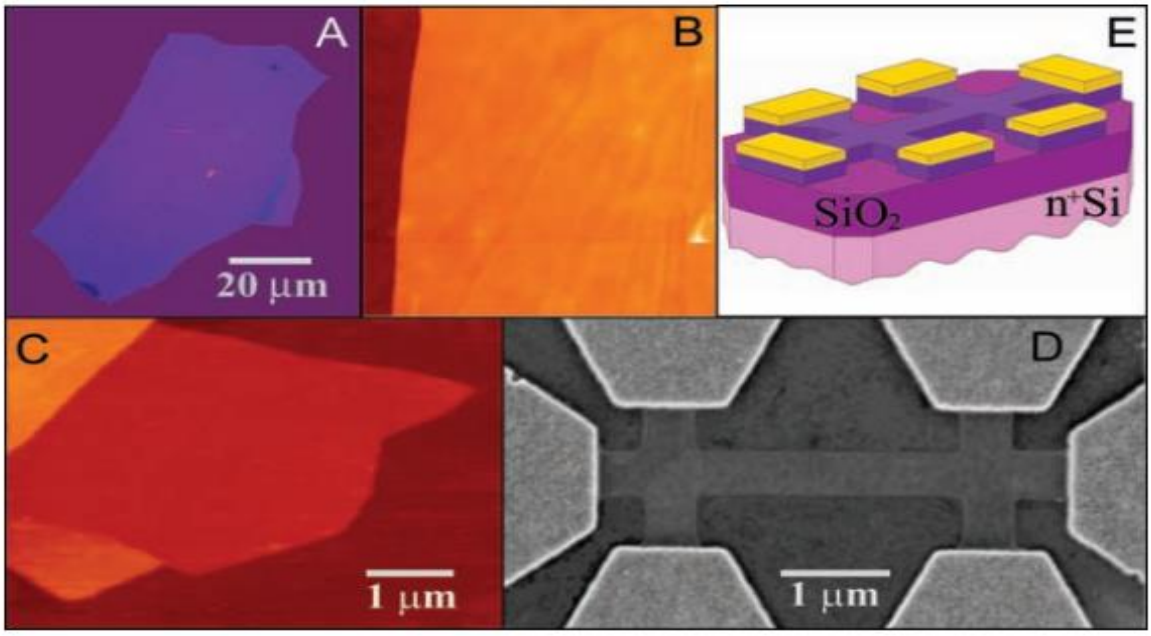

Fig.2.1: [9] Graphene films. (A) Photograph of multilayer graphene flake on top of an oxidized Si wafer. (B) Atomic force microscope (AFM) image of flake near its edge (C) AFM image of single-layer graphene. (D) Scanning electron microscope image of experimental devices prepared from FLG. (E) Schematic view of the device in (D).

2.3 General applications of graphene

Frank schwierz [12] summarised that the application of graphene in transistors and how graphene based FETs were evolved and compered the band gap structures of single and bi layered graphene transistors with semiconductor based transistors, He also analysed the cut off frequency of above different transistor, finally concluded that as graphene was 2D structured material with high conductivity, so it offers thinnest possible channel when compared to others.

Li et al. [13] used their experiment to demonstrate the catalyst property of graphene composites and came to the conclusion that on graphene–$Zn_xCd_{1-x}S$ composites with controlled composition, high-efficiency visible light driven photo catalytic H_2 production was accomplished without the aid of precious-metal kind catalysts. Under exposure to visible

light and without the use any kind of co-catalyst, the H_2-production efficiency achieves its greatest value of 1.06 mmol $h^{-1}g^{-1}$ in the combination with a graphene concentration of 0.5 wt%. Later, Qin Li et al [14] summarised the Nano composite material photocatalyste characteristics of CdS/graphene and noted that due to the strong synergetic connection among graphene and the CdS, the CdS/graphene mixtures exhibited greater photo-catalytic behaviour and photo-stability compared to the bare CdS-semiconductor. The studies were continued on the r-graphene oxide and as it has a greater area of contact and a higher electron density than other semiconductor specimens, when it was mixed with $ZnIn_2S_4$ properly and then used as a photocatalyst's that gave greater efficiency in order to strengthen the capacity to produce hydrogen gas [15].

In this article [16], the authors built a wide-spectrum solar cell using a substrate made of refractory metal and shell-shaped graphene based hollow Nano-pillars (HNPs). The refractory metal was used for impedance matching and HNPs were used for obstruct the transmission, which resulted in effective energy absorption with 95%. The authors further claimed that the aforementioned equipment was heat and weather-resistant. The graphene was also used for the electrode and storage applications [17] Maher F. El-Kad et.al explained use of graphene as electrode and in energy storage device with special features like flexible, stretchable and twistability with long life. Graphene also used in super capacitors without compromising high energy density with crystal stability and it can also recyclable and long lasting energy storage device.

The Nano porous graphene layers can able to oppose the salt-ions while passing the water flow at permeable several order of magnitude greater than existing RO membranes. By modelling saltwater circulation across various chemical functionalization and pore diameters, David Cohen-Tanugi and Jeffrey C. Grossman [18] developed that desalination processes performance was most susceptible to pore chemistry and pore size.

The graphene was also used in much application in medical science. With the help of graphene Nano-meshes, Omid Akhavan and Elham Ghaderi [19] have developed an incredibly effective in vivo photo-thermal cancer therapy. In order to achieve 100% efficiency, scientists concurrently irradiated an in vivo tumour with an ultralow power of the laser and an ultralow percentage of infused rGO-based composites. The results of their research showed that the most potential nanomaterial for the creation of extremely effective

cancer detection and treatment with minimal side effects was rGONM-PEG-Cy7-RGD (graphene composite). Bio sensors were designed using graphene oxide, Because graphene oxide exhibited unique properties like being capable of directly interact with biomolecules, chemical substances and electronic configuration with heterogeneity, the capacity to operate in solution and the potential to be altered as an insulator, semi-metal, or semiconductor, Mercosi et.al [20] utilised graphene oxide as the lattice structure for bio sensing. A number of unheard-of optical bio sensing uses were now possible thanks to GO, which was photoluminescence with the transfer of energy between donor/acceptor particles exposed on a surface that was planar. Sun x et.al [21] addressed the fact of environmentally friendly Nano-GO in a variety of sizes was produced for use in medication delivery systems. The visible to infrared photoluminescence characteristic of an NGO was discovered and utilised for cellular imaging. Anti-cancer drugs had been loaded upon high-capacity NGO and transported to specific cancer cells by utilising antibody directed targeting. Zhang H et.al [22] explained that strong near-IR absorbance and good photo-thermal effect of GO/$BaGdF_5$/PEG composite made it an excellent photo-thermal agent in in-vivo photo-thermal cancer treatment. From their work they suggested that the GO/$BaGdF_5$/PEG Nano-composite have great potential application in MR/CT biomedical imaging-guided photo-thermal therapy of cancer.

The graphene composites were also used for anti-corrosion element as it had strong chemically stable property. Yuan-Hsiang Yu et.al [23] conducted a series of electrochemical studies on the protection of corrosion properties of the Polystyrene (PS)/graphene-based Nano-composite films; they found that the PS/pv-GO Nano-composites provide substantial improvements in corrosion protection efficiency over that provided by pure PS.

2.4 Reviews on Plasmon-Surface wave-Spoof Surface Plasmon Polariton

R.H Richie [51] assumed that in a metal, the Fermi Dirac gas was constituted by conduction electrons, fast electrons going through less fractional energy and small amount of momentum change. With these assumptions he highlighted that angular-energy distribution of fast electron was losing energy to conduction electron. This distribution explained that both individual and collective interaction characteristics of electron in thick foils of metals. As foil thickness decreases energy losses increased per unit thickness. The fourth state of material was called plasma. Plasmon was the oscillations of electrons in plasma. C.J Powell and J.B Swan [52] examined the energy loss of electron in thick layers of aluminium with

high surface purity by transmission and Reflection (for surface properties) type experiments, they explained that the loss had two components, first loss was due to bulk material plasma excitation find in transmission type experiment and second loss called low-layer loss due to surface layer phenomena. If graph drawn between the ratio of plasma loss to the low-laying loss to average thickness for electron energies 760eVand 1510eV as shown in fig 2.2

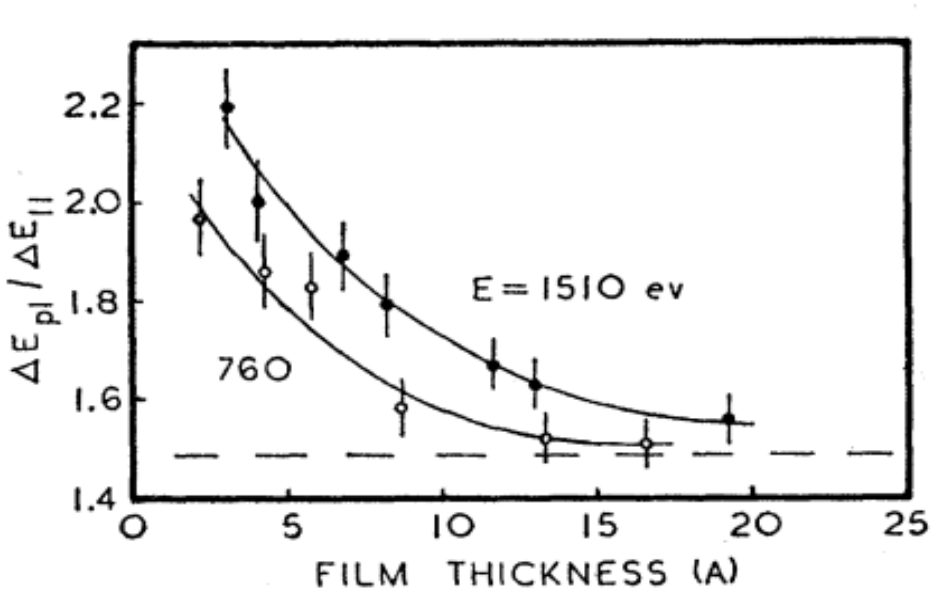

Fig 2.2: [52] The ratio of plasma loss to low laying loss was function of thickness. Dashed line was for much thicker films.

For thin films energy ratio was high and as thickness increases the energy ratio decreased and finally becomes constant for any electron energies.

Surface waves that were exist at the interface between two different materials (free space/dielectric to metals) with their field components decaying evanescently (shown in right side of fig 2.4 (a)) away from the interface as shown in fig 2.3. In metals the normal component of these waves were vanished by losing energy to the particles of metals. Wave particle interaction was a process of exchange of energy takes place between waves and particles in plasma at some constant frequency. This constant frequency was called plasma frequency of that metal. Electrons in metal collectively excited by this wave particle interaction process Surface Plasmon were formed.

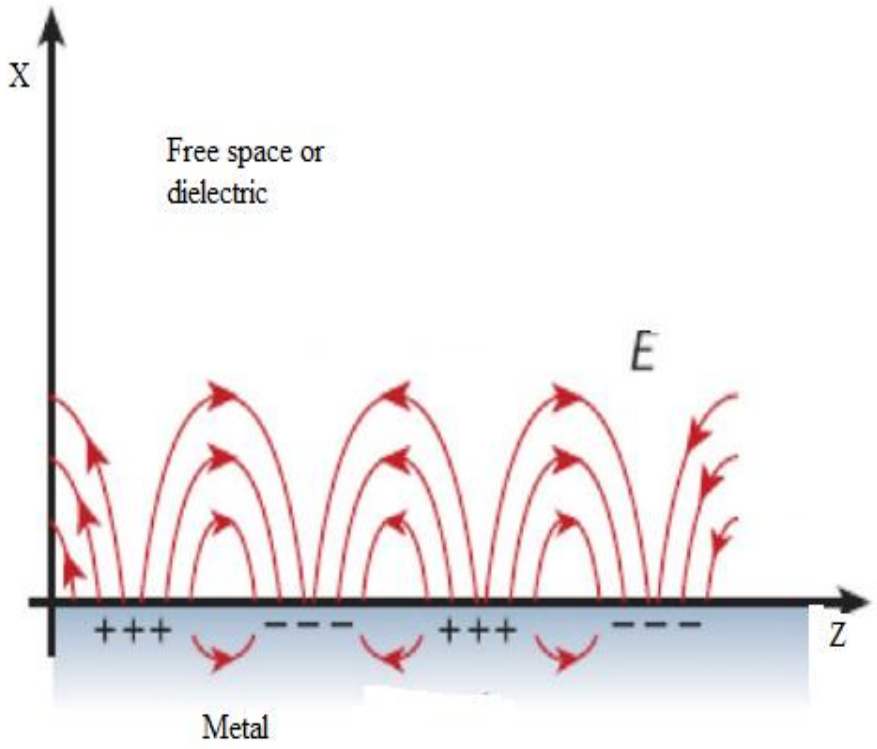

Fig 2.3: Surface waves and surface charge at interface between metal and free space/dielectric.

When EM radiated wave (TM mode excitation) was incident on metal dielectric interface as shown in fig 2.4 (a) with suitable incident angle, then this wave was interact with electrons in metal and energy transfer takes place by wave particle interaction. Now free electrons in metal were excited and try to come out from atom, but at the same time positive ions were attracted these excited electrons in opposite direction resulting electron coherent oscillations occurred as shown in fig 2.4 (b). Maximum energy transfer when the incident EM wave frequency was equal to surface Plasmon resonance of metal. Surface Plasmon (SP) was an electron coherent oscillation that exists at the interface between two materials where real part of the permittivity changes sign across the metal-dielectric interface.

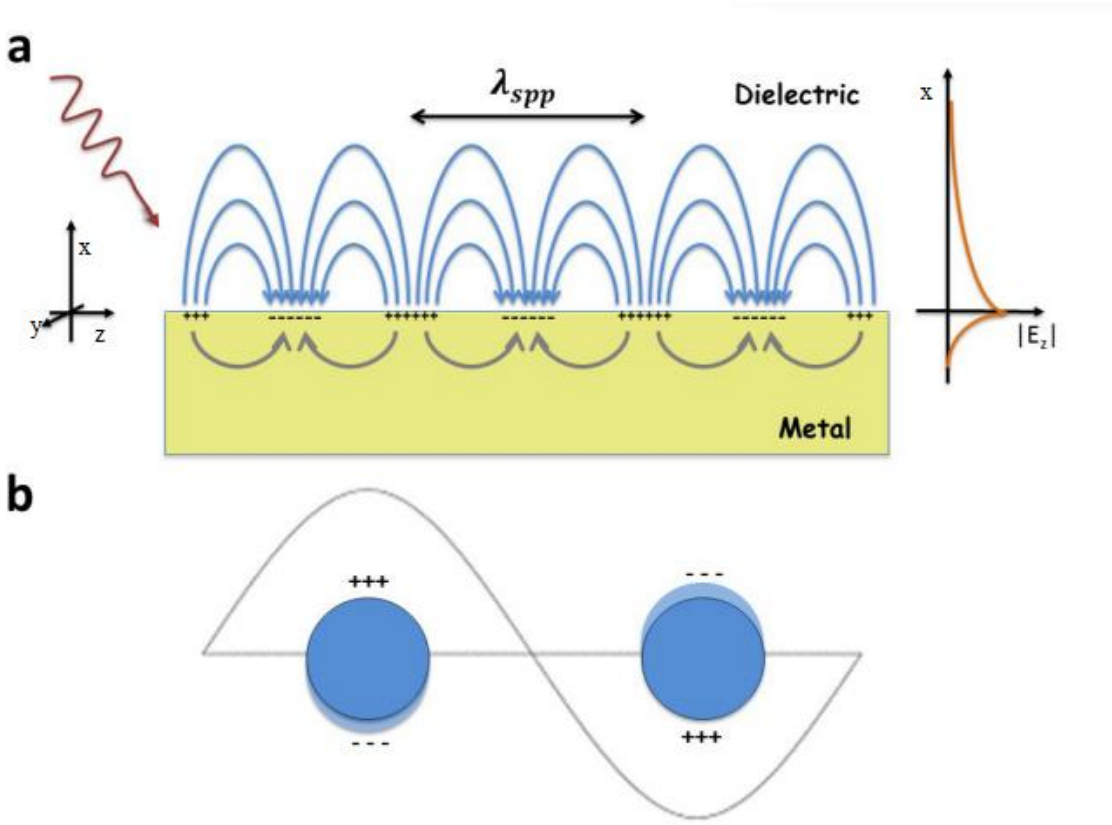

Fig 2.4: (a) EM radiated wave incident on metal dielectric interface, (b) Coherent electron oscillations of metal (Plasmon)

Low-laying reductions in energy on metal surfaces coated with an oxide coating were addressed by E.A. Stern and R.E. Ferrell [53]. The incident radiation angle affected the low-laying energy loss. The reflection angle affected the distribution of low-laying energy losses as well. The intensity structure of the scattering occurred when the waves strike at an angle (not in the usual direction). Low-laying losses energy was transformed into surface waves, which produce excitement at the interface of two distinct plasmas. J.B.Pendry et.al [54] demonstrated that when the field was incident on structured surfaces, the surface Plasmon exhibits arbitrary dispersion in frequency and in space.

Surface-Plasmon-Resonance (SPR) was a resonant oscillation of electrons that exists at the interface between two materials where real part of the permittivity changes sign across the metal-dielectric interface. Cecilia Noguez [55] mentioned that the physical environment and shape of metal-Nano particles will affect the Surface-Plasmon-Response of that metal. She considered shape of metal was function of number of vertices and faces. For different shapes the graph between the incident light wavelength and extinction efficiency was as shown in fig 2.5.

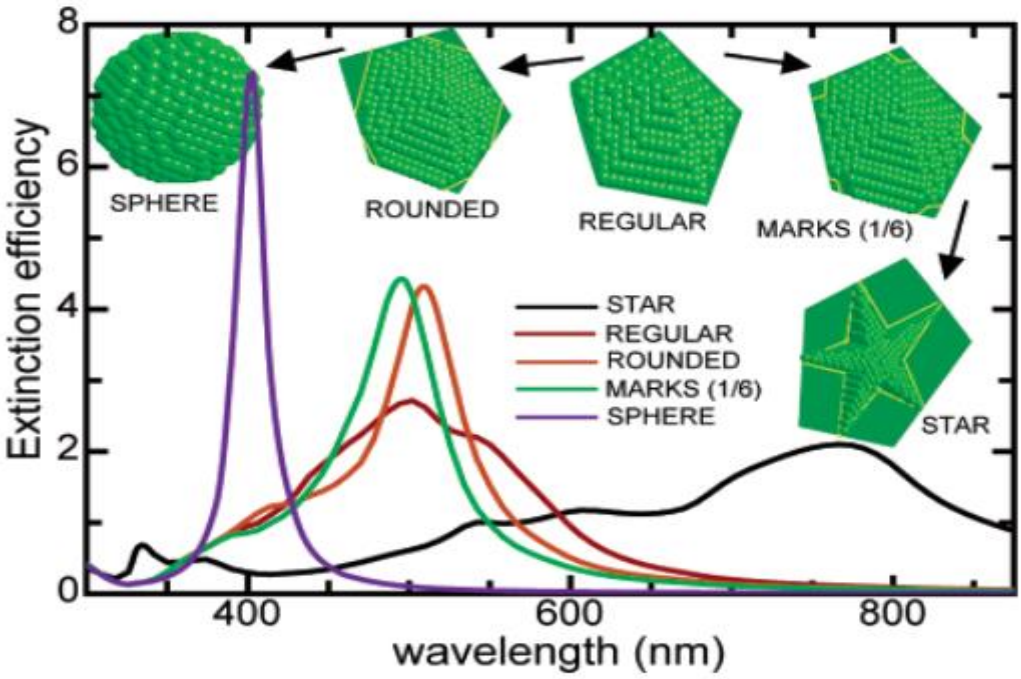

Fig 2.5: [55] Extinction efficiency as a function of the wavelength of the incident light for the regular decahedron and its truncated morphologies for parallel light polarization.

For star shape she got less extinction efficiency at higher wavelengths, for sphere shape, she got extinction efficiency high at lower wavelength only. She also explained that the surface-Plasmon-Resonance also depend on the physical environment like substrate used, Nanoparticles and other media surrounding the metal layer.

The Spoof-Surface-Plasmon-Polariton (SSPP) were the surface electromagnetic waves in microwave and Terahertz range that propagates along the planar interface between two materials (with periodic hole structure). Graphene exhibits SSPP in microwave to terahertz range. Qin p et.al [56] designed an artificial graphene based meta-surface which controls the transport and emission of EM waves at microwave frequency. They observed that Dirac cones located at corners of First Brillouin Zone (FBZ) in the momentum space of present Spoof Surface Plasmon graphene when they were excited by dipole antenna as shown in fig 2.6. As frequency raises low to high, the emission of wave front (E_z) was changed from concave shape to flat and then reached to convex as shown in fig 2.7 at different frequencies (a) 7.57GHz, (b) 8.47GHz, (c) 9.76GHz, (d) 10.57GHz and (e) 11.47GHz and exhibits negative group-velocity, Pseudo-diffusion characteristics and positive group-velocity. Pseudo-diffusion characteristics feature was exhibited at Dirac frequency when SSPPs travelling on meta-surfaces as shown in fig 2.7 at different frequencies (f) 7.57GHz, (g) 8.47GHz, (h) 9.76GHz, (i) 10.57GHz and (j) 11.47GHz .

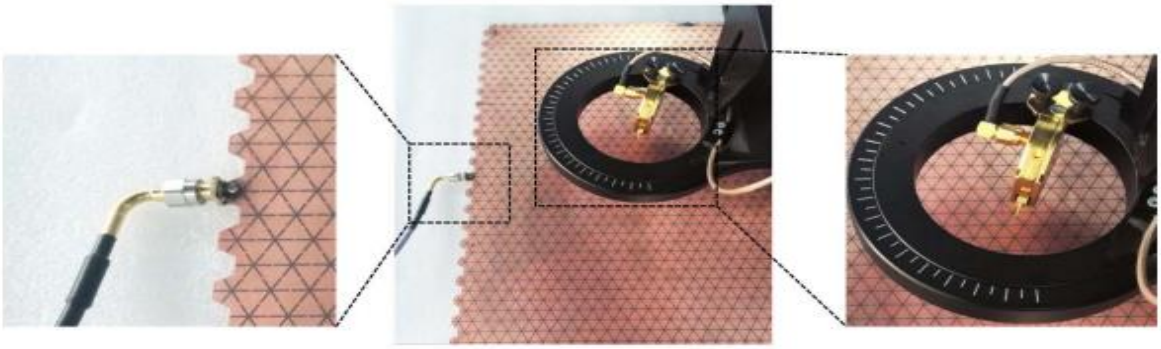

Fig 2.6: [56] An electric dipole antenna was located at the left side of the meta-surface to excite the SSPPs, and another electric dipole antenna was fixed at the arm of the 3-D movement platform to detect the z-polarized electric field. The insets enlarge the source antenna and the detector electric dipole antenna, respectively.

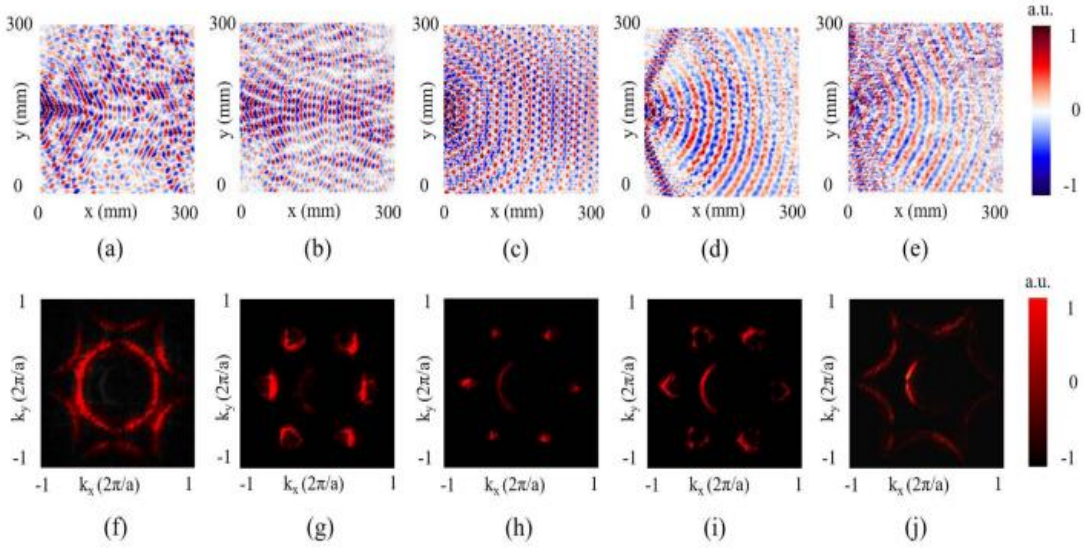

Fig 2.7: [56] Measured Ez field distribution and the corresponding isofrequency contours in the momentum space at different frequencies.

Dinh Van Tuan and Nguyen Quoc Khanh [57] investigated the effect of temperature on doped double layer graphene. They took two single-layer (carrier densities $n_1$and n_2) graphene with separated by distance d at certain temperature. Under n_2=0 and d=0 condition, there was a change in Plasmon dispersion modes when compared to zero-temperature. i.e when there was no carrier density in second layer without separation distance between two layers, then also plasmon property was not equal to single layer plasmon with equal density (n_1).

Podunavac et.al [58] designed a sensor based on SSPP concept for liquid analytic purpose. The sensor was produced using a hybrid manufacturing technique that includes

xerography, laser micromachining, and layer lamination. Dielectric constants of the oil-based samples were identified to be compared to those in the literature in order to confirm the sensing capability in a real-world scenario. It was demonstrated that the sensor outperforms alternative options with regard to cost, sensitivity, and fabrication complexity. It can detect small amount of changes in dielectric constant in liquid analytics.

2.5 Reviews on Frequency based applications of graphene

Inum R et.al [59] designed graphene based three tapered-slot-antennas (TSA), i) Linear TSA, ii) Exponential TSA (Vivaldi), iii) Constant width slot antenna using 35um thick single-layer-graphene as a radiating element. Among all three Vivaldi antenna provides high gain at low frequency region which was used in brain tumour detection. Zainud-deen et.al [60] designed a wide band impedance matching magneto-electric antenna (ME antenna) using Graphene with circular polarization. They also examined that the operating band width was depends on chemical potential of graphene element. As graphene conductivity increases the radiation efficiency and peak gain also increased. High isolation between ME antenna elements was achieved when they fit in octagonal array. By changing the chemical potential of graphene, electronic beam switching could be easily achieved.

Zhang et.al [61] designed a small size antenna (50mmx50mm) operating at 3.13 – 4.42GHz band with flexible-graphene film which was used as a wearable wireless RF sensor. They get good Omni-directional pattern of radiation. The miniaturization of sensor was achieved with high sensitivity under compressive bending (sensitivity 34.9) and tensile bending (sensitivity 35.6), after 100-cycle test of bending the sensor gave good stability in both structurally and mechanically which was useful for health and motion detection of human. There was another antenna designed for human motion detection by Sindhu et.al [62] with rectangular shaped flexible patch antenna using laser induced graphene. The antenna operating at 5.8GHz with gain of 1.8dBi and gave high sensitivity of 14.8 with fewer dimensions. When the antenna was folded the frequency (normalised) was increased and when unfolded the frequency (normalised) was decreased. It showed that when strain was applied the frequency changed. By using biodegradability property of graphene, Nemet A et.al [62] described that biodegradable textile based eco-friendly antenna for 5G communication which was designed on fabric substrate using graphene. The antenna was operating at band 3.3 – 3.8GHz with efficiency of 64%. Antenna showed stable performance when it was subjected to conformity.

Pierantoni L et.al [64] analysed a simple patch antenna using graphene as a conductor with medium losses. They took graphene surface impedance less than 10ohm and finalised radiation pattern was as similar to metal antenna when graphene surface impedance was small. They also suggested that an easy method to regulate the outcome of the array factor of a structure composed of tightly spaced graphene-patches was by changing outside bias to tune the coupling among antennas. With this concept, Zheng B et.al [65] designed an antenna array using graphene which was used for mm wave technology applications. The antenna resonating at 28GHz with minimum S_{11} of -49.87dB and impedance bandwidth of 1.1%, which had an advantages like flexibility without deformation, less material density and small in size.

The graphene exhibited high flexible property compared to the copper, so Hao-Ran Zo et.al [24] designed and fabricated a graphene based circularly polarised wearable antenna operating at 5.8GHz and tested. They found that reflection coefficient retained below -10dB, axial ratio (<3dB) band width covers 5.75-5.83GHz with gain varying from 5.6-6.1dBi. The SAR peak was 1.02W/Kg with human tissue 1grm and 0.947W/Kg for human tissue 10g which was within the limit of international standards. Isidoro I L, et.al [25] created a planar, upside cone-shaped antenna patch with CPW-fed growth of numerous layers graphene on a cellulosic textile substrate. The maximum operational bandwidth in both free-space and on-human phantom configurations was 6 GHz (3- 9 GHz). There was a minor frequency tuning issues in the performance whenever the antenna was bent, but it was insignificant given the vast operating frequency range of the antenna. In summary, they found that the suggested design had benefits like lightness, wash ability, and performance benefits like an extended radiation pattern with greatest coverage through the body, less radiation to the body due to maintaining a full ground plane, and stability was subject to antenna bending.

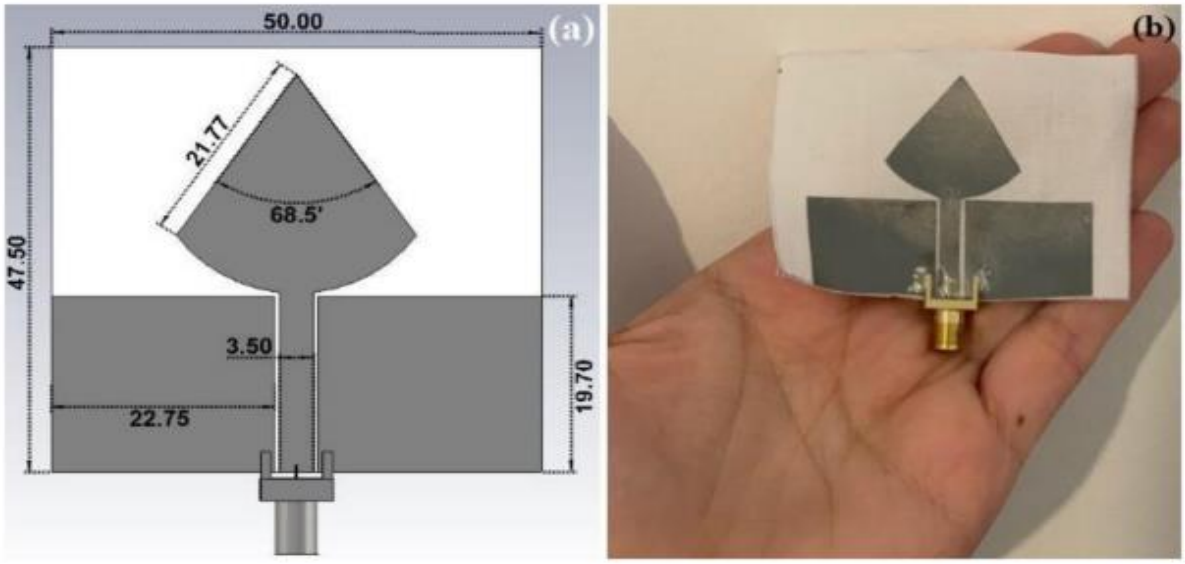

Fig 2.8: [25] a) CAD designed model of antenna with dimensions in mm, b) Antenna prototype.

The authors [26] designed different RFID tags operating in UHF using both graphene and copper found that the interrogation distance was limited for graphene based tags compared to copper based tags from the following table.

Table 2.1: [26] Comparison of interrogation distance between different UHF RFIDs.

	Tag A	Tag B	Tag C	Tag D	Tag E
Conductive track material	GNP1 (R_s = 15 Ω/□)	GNP2 (R_s = 10 Ω/□)	GNP2 (R_s = 10 Ω/□)	copper (R_s = 0.7 mΩ/□)	copper (R_s = 0.7 mΩ/□)
Chip attachment method	silver-based conductive epoxy	silver-based conductive epoxy	silver-based conductive epoxy	soldering	silver-based conductive epoxy
Substrate	kapton foil (t = 100 μm)	kapton foil (t = 100 μm)	paper (t = 200 μm)	kapton foil (t = 100 μm)	kapton foil (t = 100 μm)
No. of tags fabricated	10	5	5	5	5
Interrogation distance (std)	21 ± 5 cm (5.65)	22 ± 6 cm (5.22)	11.5 ± 3 cm (3.70)	204 cm	171 ± 22 cm (22.67)

Mitra Akbari et.al [27] designed graphene ink based a RFID tag with interrogation distance 5m at 950MHz. The realized gain of this dipole was 2.18dBi with 40% efficiency. The performance of RFID could be further improved by tuning tag antenna parameters like input feed gap and length and width of tag antenna.

The authors [28] explained the application of graphene in different sensors like electrochemical sensors, strain sensors and electrical sensors. They also compared the different research papers of sensors and highlighted the performance parameters. They

addressed that there some challenges like production of quality graphene, graphene was vulnerable to oxidised in oxidative environment and electrical and thermal conductivity may decreased in some environmental conditions. Limitations of graphene were also discussed in as shown in following table.

Table 2.2: [28] Limitations of graphene for sensor applications.

Sl. No.	Limitations
1.	The maximum photo-responsivity of graphene photodetectors is low. This is due to the small detection area of the graphene sheets and the very short photo-generated carrier lifetime.
2.	It is susceptible to oxidative environments. Thus, it cannot be used as a catalyst in redox reactions.
3.	Point defects are present in graphene due to its sp^2 hybridizing property which results in the formation of various non-hexagonal structures. This alters the electro-mechanical properties of the resultant electrodes of the sensors.
4.	Even though a lot of graphene-based strain sensors have been developed in the laboratory environment, the stretch-ability is still insufficient due to the defect density in its structure.
5.	The presence of multilayers in graphene sheets results in interlayer sliding, leading to a difference in crack densities.
6.	Defects occur in graphene's structure during its interaction with metallic substrates.
7.	There are oxides in the surface of graphene which affect the electronic and chemical properties.
8.	There are unknown cytotoxic limitations in graphene sensors which limit their usage in bio-sensing applications.
9.	A lot of parasitic effects are present in graphene which influences the response of the graphene-based sensors.
10.	The formation of different compounds with graphene changes its structural composition on which when an external load is applied, producing fracture lines, and increasing the number of dangling bonds in its structure.

Due to tuning property of graphene, Bian Wu et.al [29] discussed the first graphene-based dynamically tuneable filtering attenuators and fabricated, they achieved good tuneable attenuation and selectivity. The proposed device not only improve the degree of integration but also reduces the insertion loss compared with cascaded devices of filter and attenuator, which can find applications in the multifunctional RF front and the feed network of the antenna array. Jianzhong Chen et.al [30] designed graphene based filtering power divider with tuneable attenuator which was operated in 1.5 to 2.6GHz frequency range. By applying external voltage it can be tuned more than 10dB with maintaining low reflection coefficient in the same frequency.

Limin Ma et.al [31] demonstrated the five layered optically transparent microwave broad band absorber by graphene and metal rings, They observed that experimental results showed that 90% absorption in the frequency range 25.2−35.2 GHz, led to a bandwidth of greater than 90% absorption of up to 10 GHz, as maximal absorption approaching 99% and

an good optical transmittance of 76−78% at 400−1100 nm. These good results were due to multiple reflections and absorptions resulting from the rational layout of the structure, along with impedance matching resulting from the suitable sheet resistance of graphene. This study led to developing multifunctional electromagnetic shielding systems and novel optical microwave components. Papari Das et.al [32] explained the EMI shielding properties and mechanisms of graphene products like graphene aerogels, graphene polymer composites, doped graphene, graphene polymer composite foams and free standing graphene films varied depending on different temperatures of thermal treatment, percentage of doping, compression pressures and thickness of graphene film. The EMI shielding efficiency of graphene was high for graphene aerogels (135dB).

Qihui Zhow et.al [33] demonstrated a tuneable broadband meta-material terahertz absorber with a transmission band, 3-layered sinusoidal shaped graphene layer, SiO_2 substrate and gold FSS. The absorptivity controlled by chemical potentials of graphene with tuned from 0.4 to 0.9 within 0.5 THz to 1 THz. As EF rises from 0 eV to 0.3 eV, the pass band was stabilized at high transmission over 0.7. Because of controllable absorption in the transmission band, this design had the applications like EMC, stealth, and filtering relying on the anti-jamming capability and low loss for the normal signals. Laxmi Narayana Deekonda et.al [34] explained about design of 3 –layered graphene-based broadband meta-material terahertz absorber with a circular graphene ring on top which was used to enhance the bandwidth and gold as ground separated by SiO_2 substrate layer. Their structure gave a bandwidth of 67% for absorption with more than 90% and a bandwidth of 46% for absorption greater than 98%.

Sergi Abadal et.al [35] designed a graphene based terahertz antenna with unique features like miniaturization and tuneability with stacks containing multiple graphene monolayers and thin dielectric layers shows same trade-offs between different performance features. This analysis gave the design of antennas for size dependence applications, as Software defined meta-material may tolerate higher loss by compromise for miniaturization, whereas Wireless network on chip may give priority to performance and configurability over miniaturization. The authors [36] presented an efficient flexible tuneable antenna design for terahertz frequencies band i.e 4.546 THz, 4.636THz and 5.347 THz by changing the chemical potential and relaxation time. The authors observed that by changing the chemical potential led to increase the BW from 199GHz at 0.2 eV to 314GHz at 0.4 eV. On the other side, chemical potential had affected the radiation pattern by increasing the side lobe and

compromising the directivity of the proposed design. They also compared the substrate material on the antenna performance; graphene antenna on polyamide substrate gave the maximum S_{11} of - 42 dB. Mohammad M. Fakharian [37] designed different configurations of graphene based switchable multi-functional terahertz antenna as shown in fig 2.9 and parameters like polarization, resonant frequency and radiation pattern varied by changing the surface impedance of graphene by applied voltage witch was shown in the table 3. The structure gave band width varied from 1.2 to 1.7THz with polarization changed at 1.4THz.

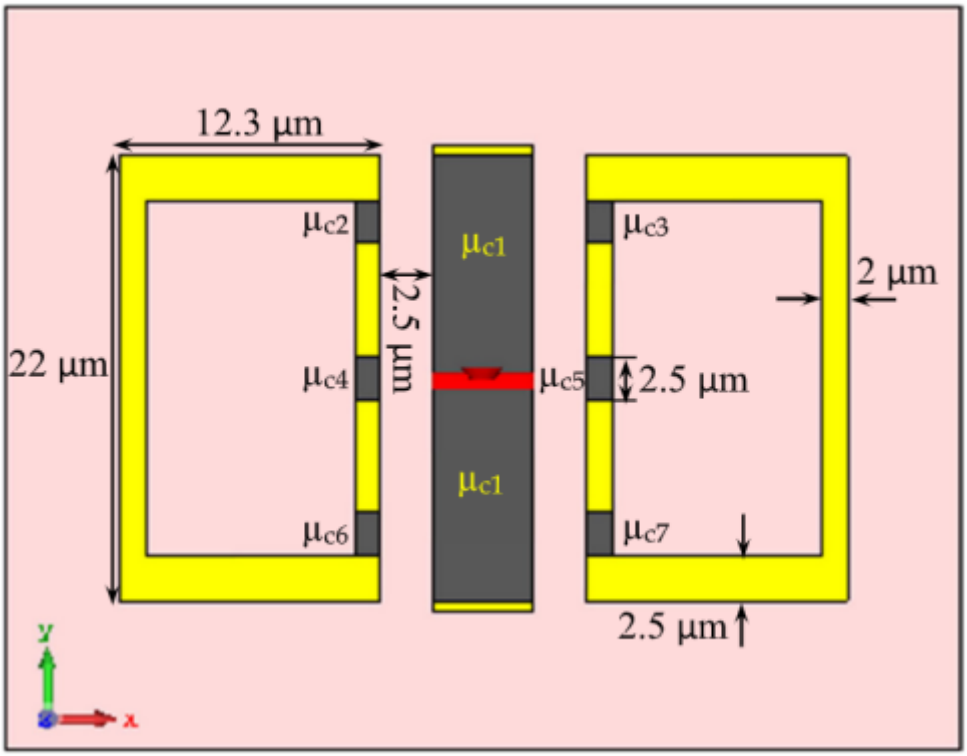

Fig 2.9: [37] Graphene based multi-functional terahertz antenna.

Table 2.3: [37] Reconfigurability of antenna for different chemical potentials of graphene.

Antenna	Chemical potential							Reconfigurability
	µc1 (eV)	µc2 (eV)	µc3 (eV)	µc4 (eV)	µc5 (eV)	µc6 (eV)	µc7 (eV)	
Ant. 0	0.6	–	–	–	–	–	–	None
Ant. 1	0.4	0	0	0	0	0	0	Frequency
Ant. 2	0.6	0.6	0.6	0	0	0.6	0.6	
Ant. 3	0.6	0	0	0	0	0	0	
Ant. 4	0.8	0	0	0	0	0	0	
Ant. A	0.6	0.6	0	0	0	0.6	0	Radiation Pattern
Ant. B	0.6	0	0.6	0	0	0	0.6	
Ant. C	0.7	0.7	0	0.7	0.7	0	0.7	Polarization
Ant. D	0.7	0	0.7	0.7	0.7	0.7	0	

Amit Sharma and Dinesh Kumar Vishwakarma [38] developed graphene based square shaped trucked terahertz antenna associated 5-element diamond structured multi-feed antenna array operated at 6.45Hz. They observed smith chart variation as well as far-field parameter analysis such as gain, axial ratio, directivity, radiation efficiency and compared with the single element with the 5-element terahertz antenna array and finalised that array gave a broadside radiation pattern, high gain (>13dBi), circularly polarization(AR BW>0.15THz) , suitable for inter-chip to inter-satellite terahertz communication systems, terahertz WLAN, ultrafast nano-sensors for biomedical applications and missile guiding systems.

Meisam Esfandiyari et.al [39] designed a dual band stop filter and single band antenna with tuning capability by varying the chemical potentials in terahertz band. They showed that the resonance frequencies were at 0.01, 0.3 and 0.1THz in first and second band of filter and single band antenna respectively when chemical potential varied from 0.4eV to 1eV. G Challa Ram [40] designed a transmission line modelled band stop filter with open-circuit stubs in terahertz regime with tuneability. The tuneability was achieved by changing width of stub or by changing chemical potentials of graphene. They showed that 0.1THz tuning range was achieved when graphene potential change from 0.3eV to 1eV.

Heng Zhang et.al [41] designed and fabricated the graphene based active FSS in microwave frequencies, the graphene used as absorption layer to control the absorbility. They achieved transmission of 81.7% at resonant frequency when there was no applied voltage. When they applied external voltage of 3.6V to graphene layer then transmission coefficient decreases to 25.2%. So the authors suggested that this structure may be used as on-off switch. Chi Ma et.al [42] designed a graphene based novel FSS modulator and they compared the results with numerical investigation. Their structure was combination of graphene, silicon dielectric, FSS, silicon dielectric and graphene with modulation depth of 90% in the band of 0.23 to 0.6THz. This structure had application in medical imaging. Yao-Jia Yang et.al [43] simulated six hexagonal graphene based FSS screen which surrounded the monopole omnidirectional antenna shown in fig 2.10 for switchable with filtering in two bands. By varying the chemical potential of graphene from 0eV to 0.5eV, they achieved high transmission (on state) and almost total reflection state in bands independently. So they achieved 360^0 omnidirectional radiation and beam scanning in those bands.

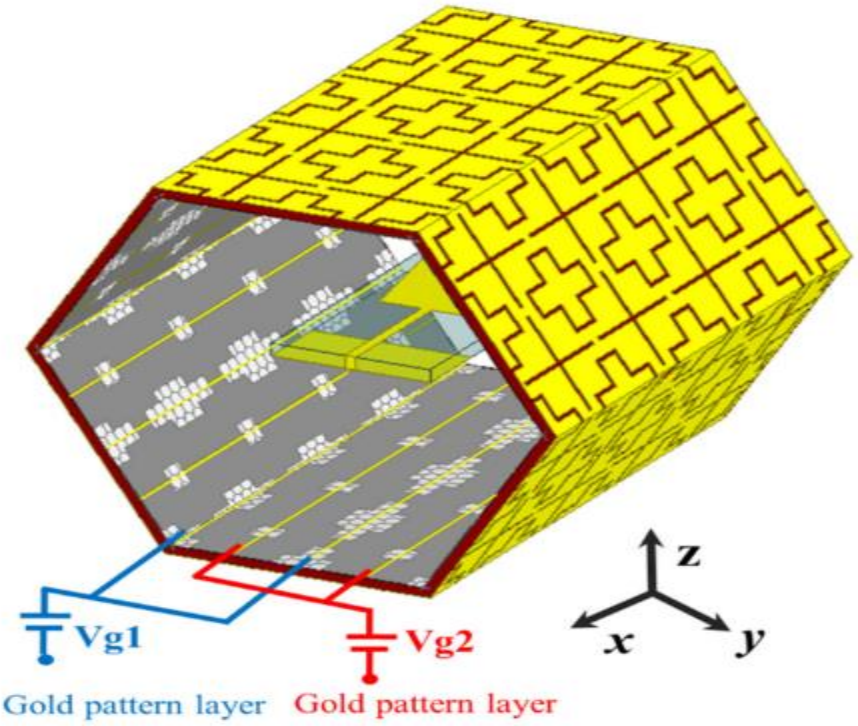

Fig 2.10: [43] 3D view of Dual band beam steering THz antenna surrounded by graphene based FSS.

Hamidreza Taghvaee et.al [44] investigated the multi-wideband terahertz graphene based metasurface for 6G communication applications. They combined different layers of graphene, alumina, HDFE and gold to design the unit cells which produces Reconfigurability of the local reflection phase at multiple frequencies by varying the biasing voltage of graphene layers independently. They showed that beam splitting, beam steering, random scattering, and collimation-functionalities were achieved at the different frequencies (i.e., 0.65, 0.85, and 1.05 THz), which were defined by low atmospheric attenuation. The main advantage of this metasurface was that it can be used for multiple applications.

Nianchao Li et.al [45] designed a grahene based polarization conversion metasurface in terahertz band which converts the co-polarised wave to cross-polarised wave. Their structure was composed of columnar metal and metal on polyimide with gaps filled by graphene to get the controllability. When they adjusted the Fermi level of graphene they got regulated the polarisation conversion from 95% to 25% from 2.1 to 3.6THz wideband. Shuvajit Roy and Kapil Debnath [46] designed electromechanically tuneable graphene plasmonic metasurface, in their design graphene membrane surface was controlled by applied voltage. When they applied voltage up to 20V and got tuneability of 0.5THz in the band of 5-6THz. they also found that the switching speed for different input voltage was limited by

maximum resonance frequency. This structure has different applications like beam steering, sensors, actuators and MEMS based detectors.

From the above reviews, the graphene was Nobel Nanomaterial in the world which created tremendous opportunities for the researchers to design new devices which meets current needs of technology in all field of science, so the basics of graphene discussed in the next chapter.

CHAPTER -3
BASICS OF GRAPHENE and METASURFACE

3.1 Chapter overview

This chapter discussed about the basic structure of graphene (section 3.2 and 3.3), properties of graphene, surface waves on metals along with drude model for metal will be discussed in sections from 3.3 to 3.6, methods of preparation of graphene was explained briefly in section 3.7, testing methods of graphene was elaborated in section 3.8 and finally in section 3.9 brief discussion about the Metasurface was presented.

3.2 Structure of graphene

3.2.1 Atomic structure

In the 1930s, Landau and Peierls (and Merminin in 1960s) showed thermodynamics prevented Two-dimensional (2D) crystals to be unstable and so could not form, as was demonstrated more than 70 years ago [47]. The Single atomic layer of carbon in graphite was first mentioned by Wallace 1947 in his theoretical work [66]. There were two three-dimensional (3D) natural allotropes of the element carbon found, those were graphite and diamond. These two materials were composed of large networks of sp^2 and sp^3 hybridised carbon atoms, respectively. Hybridization means when different atomic orbitals of same or nearly same energy combine together to form new hybrid orbitals. Carbon has an atomic number 6, which means it has total six electrons surrounding its nucleus, out of six 2-electrons were in inner shell and 4-electrons were in outer shell with configuration $1s^2\ 2s^2\ 2p^2$. The 4 outer shell electrons of carbon atom were involved in chemical bonding. A carbon atom has sp^3 hybridization as shown in fig 3.1. When carbon atom was in ground state, there was no change of state of electron to higher orbital. When it was excited the one of 2s electron was shifted to $2p_z$ orbital. The 2s, $2p_x$, $2p_y$ and $2p_z$ combined and forms the four sp^3 hybridized orbitals which forms the tetrahedron shape with bond angle 109.5^0. These sp^3 hybridized carbon atoms forms σ- bonds between them which were very strong in nature. So the carbon atoms with sp^3 hybridization in a diamond molecule were strongly bonded to one another, forming a tetrahedron-shaped link between each carbon atom.

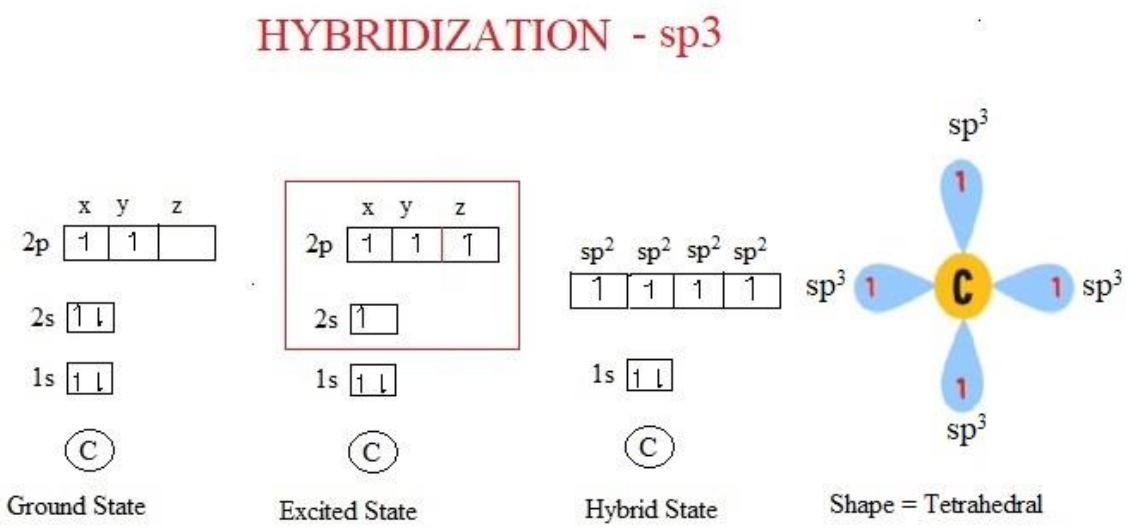

Fig 3.1: SP^3 Hybridization of carbon atom.

A carbon atom had sp^2 hybridization as shown in fig 3.2. When carbon atom was in ground state, there was no change of state of electron to higher orbital. When it was excited the one of 2s electron was shifted to $2p_z$ orbital. The 2s, $2p_x$ and $2p_y$ combined and forms the three sp^2 hybridized orbitals which forms the trigonal shape with bond angle 120^0. The unhybridized $2p_z$ orbital was orthogonal to hybridized orbitals as shown in fig 3.2. The sp^2 hybridized orbitals were responsible for σ- bonds (very strong) and unhybridized $2p_z$ orbital was responsible for π-bond (week in nature).

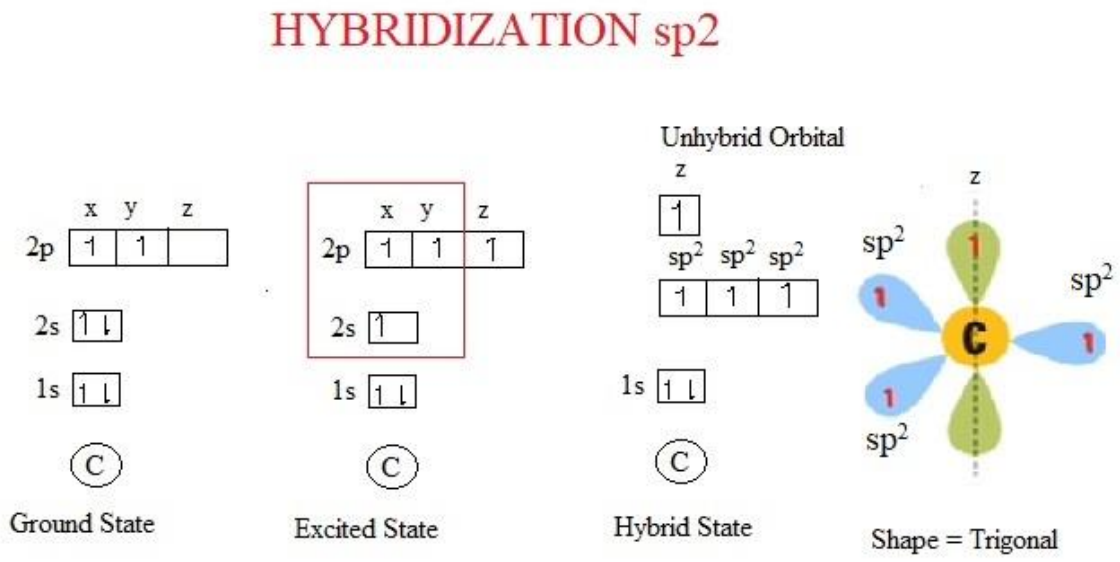

Fig 3.2: SP^2 Hybridization of carbon atom.

The Graphite was structured with sp^2 hybridized carbon atoms in a layered substance with inter layer distance was 0.335 nm, and the carbon atoms on each layer were organised in a hexagon with a separation of 0.142 nm.

For a very long period up to the discovery of fullerenes in 1985, the only known allotropes of carbon were graphite and diamond [67]. Similar to graphite in structure, fullerene (0D) was an allotrope of carbon having hexagonal and pentagonal patterns of carbon atom correlation. The many allotropic carbon structures were shown in Figure 3.3.

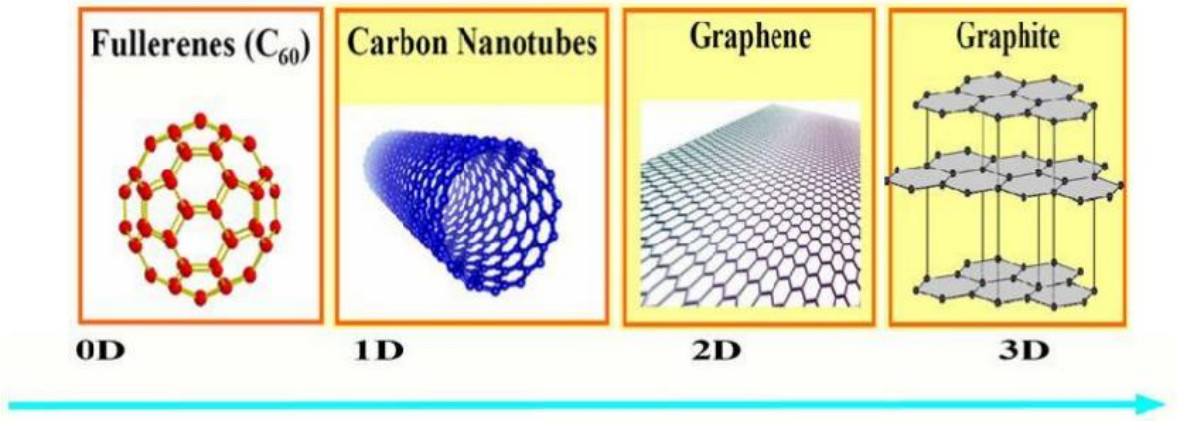

Fig 3.3: Allotropes of carbon

According to Andreoni's [68] research, fullerenes were molecules with spherically organised carbon atoms, making them zero-dimensional objects with distinct energy states from a physical perspective. Another member of the fullerene family was the carbon nanotube (CNT), which has a tubular structure with cylindrical carbon molecules and exhibits amazing strength and distinctive properties. They possess both electrical qualities and effective heat conductivity. Charlier et.al [69] investigated the process of forming carbon nanotubes from graphene by rolling it in a specific direction and re-connecting the carbon bonds. As a result, carbon nanotubes could be conceived of as one-dimensional (1D) objects because they only contain hexagons.

Graphene was a sheet of graphite that was one sp^2 hybridized carbon atom size and had an atomic thickness of 0.345 nm with carbon to carbon atomic distance was 0.142 nm. As discussed earlier one carbon had three sp^2 hybridized orbital and one unhybridized $2p_z$ orbital bonded with another same carbon atom as shown in fig 3.4. When carbon atom was in excited state, three outer-shell sp^2 hybridized electrons of one carbon atom were σ- bonded with three outer-shell sp^2 hybridized electrons of other carbon atom in plane as shown in fig

3.4 and these bonds were responsible for thermal and mechanical properties of graphene. The other one electron i.e unhybridized $2P_z$ orbital in carbon atom was π-bonded with unhybridized $2P_z$ orbital of other carbon atom perpendicular to the plane shown in fig 3.4 and it was responsible for electrical properties of graphene.

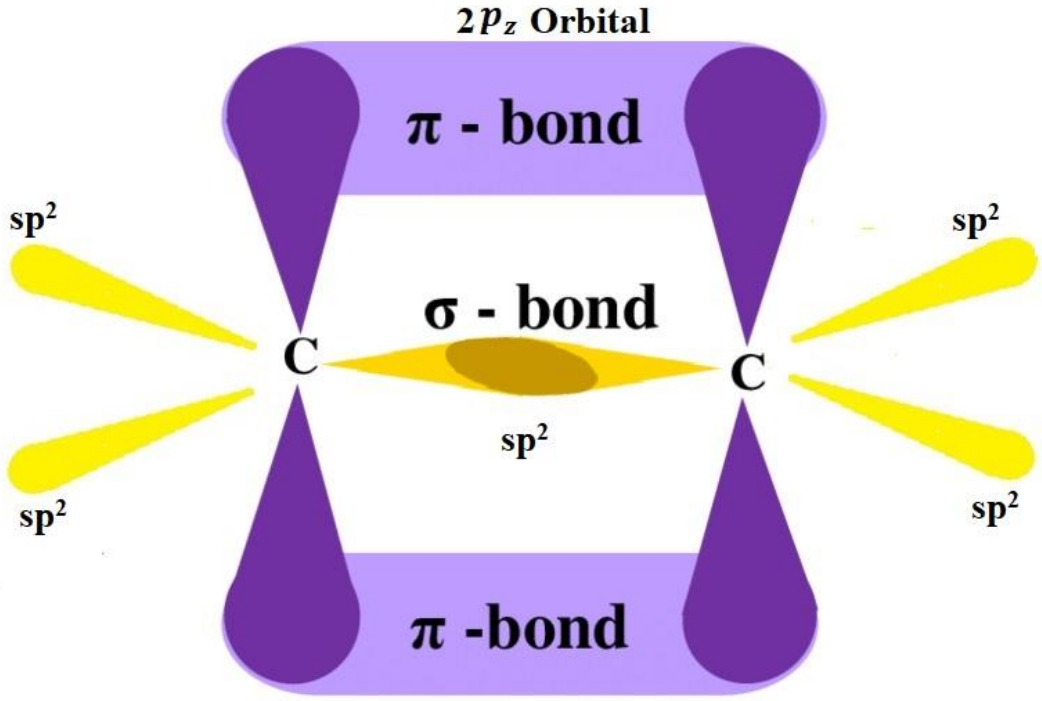

Fig 3.4: Bond structure between two carbon atoms of graphene.

The basic structure of graphene was shown in fig 3.5. The basic building block of crystal was called unit cell of that crystal. Graphene had unit cell with 2- atoms as shown in fig 3.5. The blue and red atoms of carbon were opposite in spin in $2P_z$ orbital which explained magnetic properties of graphene.

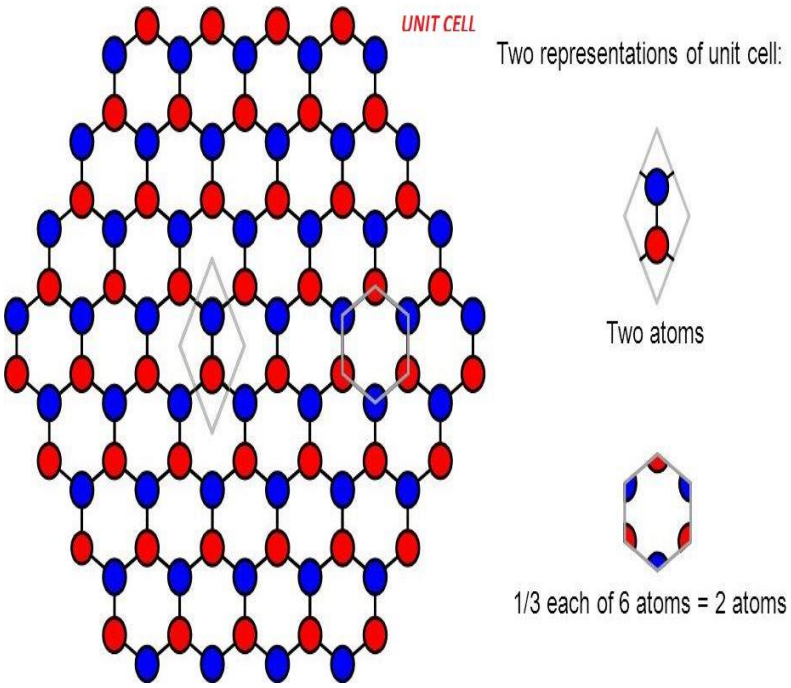

Fig 3.5: Graphene Structure and Unit cell of graphene.

3.2.2 Band structure of graphene

Two distinct structures were produced after cutting the 2D infinite graphene sheet, and they were known as zigzag and arm chair graphene Nano-ribbons (GNRs), respectively, as illustrated in Fig 3.6.These gave rise to various band structures and electrical spectra for them and was named after their distinctive atomic-scale appearance. There was no edge reconstruction in armchair GNR, preserving the planar patterns, while it was unexpectedly discovered that the zigzag edge of zigzag GNR was meta-stable and reconstructions occur spontaneously at high temperature Shen-lin Chang et.al [70]. According to Young- woo Son et.al [71] Varied edge structure GNRs exhibit a range of electronic properties, from spin-polarized half metals to regular semiconductors, opening the door for the use of GNRs in the construction of electric devices.

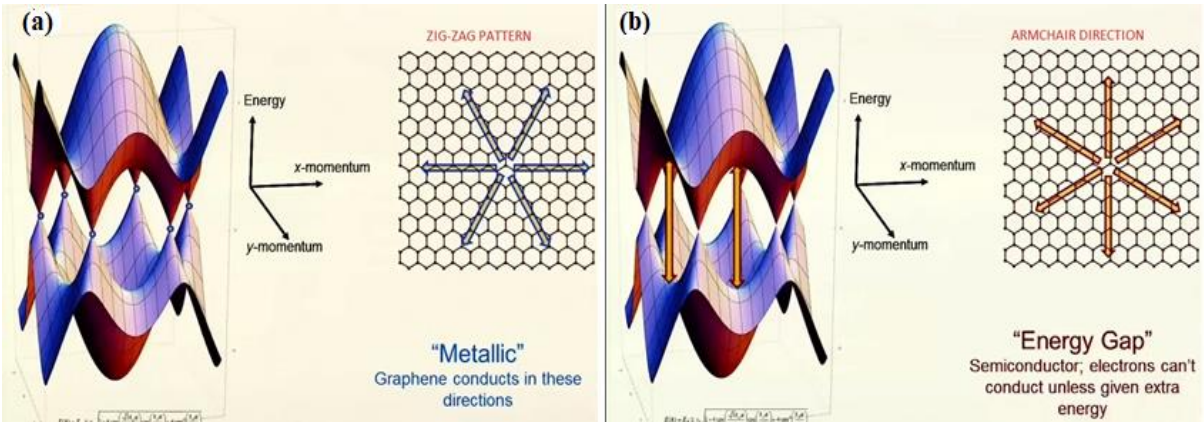

Fig 3.6 (a): Band structure of graphene in zig-zag pattern, Fig 3.6 (b): band structure in armchair pattern.

Graphene had unique conical shape of band structure with zero band gaps at conical point as shown in fig 3.6 and 3.7 between valance and conduction band. The charge carriers in graphene primarily behaved as massless relativistic particles with a conical energy spectrum $E = v_f \hbar k$, where v_f was the Fermi velocity, $\hbar$ was the reduced Planck constant, and k was the wave vector. The energy momentum relation was linear as move from centre point of brillouin zone to edge of brillouin zone which gives conical structure. The cone of the conical structure was called Dirac point. Graphene had two types of edge cuttings as discussed earlier; first one was zigzag pattern which gives metallic properties of graphene. Due to this structure the valance and conduction bands were meeting at Dirac points in band structure as shown in fig 3.6(a). Second one was armchair pattern which gives semiconductor (semimetal) properties of graphene. Due to this structure there was band gap between the valance and conduction bands as shown same fig 3.6(b).

By giving (n-doping) or taking away (p-doping) electrons, molecules adsorbing on graphene may potentially modify its electrical characteristics and change its Fermi level Martin Pykal et.al [72]. DFT simulations can directly identify which adsorbents/supports donate/withdraw electrons to/from graphene and give detailed information about electron fluxes. In order to create graphene devices with a usable band gap that can be used in graphene-based transistors, this property was also taken use of bilayer graphene sandwiched between $FeCl_3$ and K can be used to make such devices $FeCl_3$ was determined by calculations to be an electron acceptor capable of producing p-doped graphene, and K was determined to be an electron donor capable of producing n-doped graphene. The energy band diagram for all these cases along with pristine graphene and bilayer graphene was shown in fig 3.7 (a) and (b). As number of layers increased band gap also increased as shown.

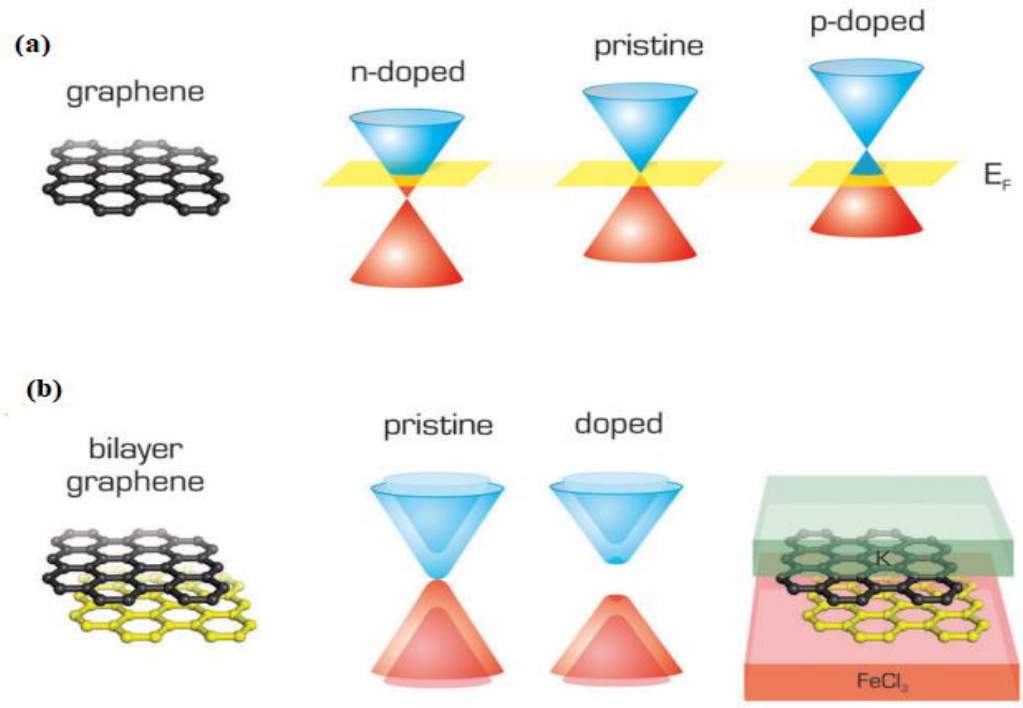

Fig 3.7(a): [72] Band structure of pristine, p and n- type doped single layer graphene, Fig 3.7(b): Band structure of pristine and doped bilayer graphene.

3.3 Properties of graphene

The wide variety of graphene's structural variations were accompanied by a wide range of their striking chemical, physical, mechanical, electrical, and electronic properties that were crucial for thorough evaluation of graphene material for using in many applications. Carbon-based systems exhibit an infinite array of distinct structures with an equivalent variety of physical attributes due to the flexibility of their bonding. These physical characteristics were mostly a result of these structures dimensionality. Many of the non-electrical and electrical phenomena discussed in the following Sections can be attributed to graphene's hypothetical semimetal behaviour, which has zero band gap energy and zero effective masses of the electrons and holes.

3.3.1 Thermal properties

At room temperature, graphene has one of the highest thermal conductivities of any known material, ranging between 2000 and 5000 $Wm^{-1}K^{-1}$ for samples that were hanging freely. Graphene was frequently considered to be superior to other materials from the perspective of Nano-scale devices and interconnects because of its better thermal conductivity, which suggests superior heat sinking and reduced temperature rise during

device operation Eric Pop et.al [73]. Due to the potential for thermal management applications, research into thermal transport in graphene was an important topic of study. Early tests of the thermal conductivity of a pure sample of suspended graphene revealed an incredibly high value of about 5300 $Wm^{-1}K^{-1}$ Balandin A.A et.al[74], which was much higher than the thermal conductivity of pyrolytic graphite at room temperature of about 2000 $Wm^{-1}K^{-1}$.

3.3.2 Mechanical properties

A unique combination of mechanical characteristics was seen in graphene. Research has shown that suspended graphene exhibits both brittle fracture and non-linear elasticity. Additionally, because of graphene's superior elastic characteristics, it may regain its former shape after relieving the tension. Young's modulus of 0.5 TPa and variable spring constants of 1-5 N/m were obtained through atomic Force Microscopy (AFM) investigation of suspended graphene sheets that ranged in thickness from 2 to 8nm I. W. Frank et.al [75]. It responded to deformation in a remarkable way, being superior to hard materials, which fail at about 1%, in that it can bear up to 20% tensile strain before fracture Lee et.al [76]. However, defects in graphene-like vacancies, Stone-Wales defects, dislocations and grain boundaries which impaired its mechanical properties, greatly affected these ideal values Meyer J.C et.al [77].

3.3.3 Optical properties

Understanding the linear response of graphene was made easier by an understanding of its optical conductivity. Graphene's higher and lower energy levels combine at a single spot. Electrons in the occupied energy levels of graphene absorb the energy from incident waves and become excited to higher energy levels as soon as electromagnetic energy was incident on the material. Within the band and between the bands, the electron will transition. As a result, both the intra band and inter band transitions contributed to graphene's actual conductivity as shown in fig 3.8. The intra band transition of charge carriers rises after graphene was activated by a THz-frequency energy source, and this intra band charge transition significantly contributes to graphene's effective conductivity.

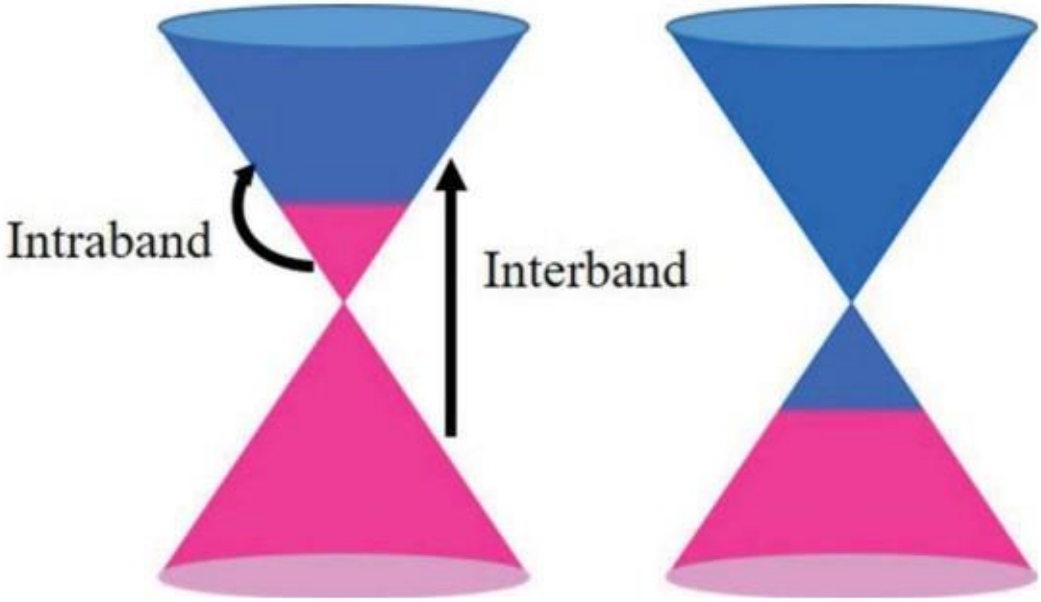

Fig 3.8: Graphene intra and interband Transitions when EM incident.

The Drude mathematical model can be used to theoretically investigate this intra band transition effect. The conductivity of graphene was frequency-dependent, behaving differently at different frequency bands. It was affected by the Fermi level (also known as chemical potential), which controls the surface carrier density. Because thermal carriers were substantial at low carrier densities, temperature T has an impact on conductivity. Finally, because it was closely related to carrier mobility, the mean free time in between carrier collisions, also known as the carriers' scattering time, has a significant influence on conductivity. The graphene electronic band structure-dependent Kubo formula, which provides an excellent numerical approximation of graphene conductivity up to visible light frequencies, can be used to explain these phenomena. To explain all these concepts by start with drude model for metals, then negative permittivity of metals, surface Plasmon resonant frequency, electronic properties and finally kubo formula of graphene conductivity.

3.4 Drude model for metals

Drude applied kinetic gas theory to conduction electrons in metals. He assumed that i) between collisions electrons move in straight line, Effect of electron-electron interaction and effect of electron-ion interaction was ignored. ii) Mean free time between collisions τ was independent of electron's position or velocity. iii) Electrons achieved thermal equilibrium by

collisions with lattice. First the permittivity calculation in static electric fields was done and then find for oscillating fields.

Let us consider a metal, the free electrons were propagated as shown in fig 3.9, the electric dipole moment produced by an electron as shown in fig 3.9, when a static electric field E applied, and electron experiences a linear restoring force F = $m_e\omega_0^2 x$ (where m_e was the effective mass of the electron, ω_0 was Natural frequency, x was charge displacement) in opposite direction then

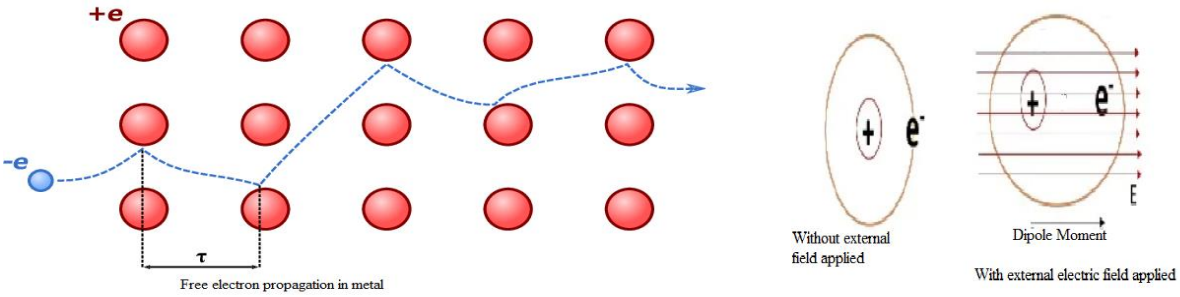

Fig 3.9: Drude model for metals.

$$eE = m_e\omega_0^2 x \tag{3.1}$$

The resulting charge displacement was given by

$$x = \frac{eE}{m_e\omega_0^2} \tag{3.2}$$

The electron polarization was given by

$$P = ex = \frac{e^2E}{m_e\omega_0^2} \tag{3.3}$$

If metal has free electron density N_e then total polarisation was given by

$$P = \frac{N_e e^2 E}{m_e\omega_0^2} \tag{3.4}$$

Polarization in terms of susceptibility given by

$$P = \epsilon_0 \chi_e E \tag{3.5}$$

Where χ_e =Electric susceptibility

Note: How quickly a dielectric substance polarises in response to an electric field was measured by its electric susceptibility.

Now on equating equation (3.4) and (3.5)

$$\epsilon_0 \chi_e = \frac{N_e e^2}{m_e \omega_0^2}$$

$$\chi_e = \frac{N_e e^2}{\epsilon_0 m_e \omega_0^2} \quad (3.6)$$

$$\chi_e = \frac{\omega_p^2}{\omega_0^2} \quad (3.7)$$

Where

ω_p = plama frequency $= (\frac{N_e e^2}{\epsilon_0 m_e})^{1/2}$, Typical metals have $\omega_p \sim 10^{16}$ rad/s

N_e was now interpreted as free electron density, N_e. Typical metals have $N_e = 10^{22}$ cm^{-3}

m_e was the effective mass of the electron.

ω_0= Natural frequency.

Γ=Damping factor or mean collision frequency in Hz.

The Electric flux density was given by

$$D=\epsilon_0 E+ \epsilon_0 \chi_e E$$

$$D=\epsilon_0 (1 + \chi_e) E \quad (3.8)$$

The electric flex density can also expressed in terms of complex permittivity as

$$D= \epsilon_0 \epsilon_r E \quad (3.9)$$

The right hand side equations (3.8) and (3.9) were equal

$$\text{i.e } \epsilon_0 \epsilon_r E= \epsilon_0 (1 + \chi_e) E$$

$$\epsilon_r= 1 + \chi_e \quad (3.10)$$

From equation (3.6)

$$\epsilon_r= 1 + \frac{N_e e^2}{\epsilon_0 m_e \omega_0^2} \text{ For static fields} \quad (3.11)$$

For oscillating fields, from the Lorenz oscillator model the susceptibility in terms of frequency was given by

$$\chi_e(\omega) = \frac{\omega_p^2}{\omega_0^2 - \omega^2 - j\omega\Gamma} \quad (3.12)$$

Where

ω_p = plama frequency

ω= Operating frequency.

ω_0= Natural frequency.

Γ=Damping factor or mean collision frequency in Hz.

Then permittivity of material was given by

From equation (3.10)

$$\epsilon_r(\omega) = 1 + \frac{\omega_p^2}{\omega_0^2 - \omega^2 - j\omega\Gamma} \quad (3.13)$$

But for metals most of electrons were not bounded to nucleus and they were free, so restoring force was negligible and their natural frequency was zero (ω_0=0) and damping factor was equal to $\frac{1}{\tau}$. Here τ was the average time an electron travels between consecutive collisions.

Then metal permittivity was given by

$$\epsilon_r(\omega) = 1 + \frac{\omega_p^2}{0 - \omega^2 - j\omega\tau^{-1}}$$

$$\epsilon_r(\omega) = 1 - \frac{\omega_p^2}{\omega^2 + j\omega\tau^{-1}} \quad (3.14)$$

The complex permittivity can be written in terms of the real ($\epsilon'_r(\omega)$) and imaginary $\epsilon''_r(\omega)$ components

$$\epsilon_r(\omega) = \epsilon'_r(\omega) + j\epsilon''_r(\omega) = 1 - \frac{\omega_p^2}{\omega^2 + j\omega\tau^{-1}} \quad (3.15)$$

To get the real and imaginary parts the R.H.S term should be normalized by multiplying numerator and denominator by $\omega^2 - j\omega\tau^{-1}$

$$\epsilon_r(\omega) = \epsilon'_r(\omega) + j\epsilon''_r(\omega) = 1 - \frac{\omega_p^2}{\omega^2 + j\omega\tau^{-1}} \times \frac{\omega^2 - j\omega\tau^{-1}}{\omega^2 - j\omega\tau^{-1}}$$

$$= 1 - \frac{\omega_p^2\omega^2}{\omega^4 + \omega^2\tau^{-2}} + \frac{j\omega_p^2\omega\tau^{-1}}{\omega^4 + \omega^2\tau^{-2}}$$

$$= 1 - \frac{\omega_p^2}{\omega^2 + \tau^{-2}} + \frac{j\omega_p^2\tau - 1}{\omega(\omega^2 + \tau^{-2})}$$ (after taking ω common in numerator and denominator and cancelled)

$$\epsilon'_r(\omega) + j\epsilon''_r(\omega) = 1 - \frac{\omega_p^2\tau^2}{1 + \omega^2\tau^2} + j\frac{\omega_p^2\tau/\omega}{1 + \omega^2\tau^2}$$ (after re arranges the τ) (3.16)

By comparing real and imaginary part both sides

Real part of permittivity was

$$\epsilon'_r(\omega) = 1 - \frac{\omega_p^2\tau^2}{1 + \omega^2\tau^2} \quad (3.17)$$

Imaginary part of permittivity was

$$\epsilon''_r(\omega) = \frac{\omega_p^2\tau/\omega}{1 + \omega^2\tau^2} \quad (3.18)$$

It can be expressed that material losses in terms of complex permittivity as

$$\nabla \times H = j\omega\epsilon_0\,\epsilon_r(\omega)\,E \quad (3.19)$$

The losses in materials were expressed in real conductivity and real permittivity by Maxwell's equation

$$\nabla \times H = \sigma E + j\omega\epsilon_0\,\epsilon_r E \quad (3.20)$$

After equating the right hand side of equations (3.19) and (3.20)

$$j\omega\epsilon_0\,\epsilon_r(\omega)\,E = \sigma E + j\omega\epsilon_0\,\epsilon_r E$$

$$j\omega\epsilon_0\,\epsilon_r(\omega) = \sigma + j\omega\epsilon_0\,\epsilon_r$$ (after cancelling E on both sides)

$$j\omega\epsilon_0\,\epsilon_r(\omega) = j\omega\epsilon_0\left(\epsilon_r + \frac{\sigma}{j\omega\epsilon_0}\right)$$ (Taking $j\omega\epsilon_0$ common from R.H.S)

$$\epsilon_r(\omega) = \epsilon_r - \frac{j\sigma}{\omega\epsilon_0} \quad (3.21)$$

The complex permittivity can be written in terms of the real ($\epsilon'_r(\omega)$) and imaginary $\epsilon''_r(\omega)$ components

$$\epsilon_r(\omega) = \epsilon'_r(\omega) - j\epsilon''_r(\omega) = \epsilon_r - \frac{j\sigma}{\omega\epsilon_0} \tag{3.22}$$

On comparing both sides

$$\epsilon'_r(\omega) = \epsilon_r \tag{3.23}$$

$$\epsilon''_r(\omega) = \frac{\sigma}{\omega\epsilon_0} \tag{3.24}$$

Conductivity of metal ($\sigma(\omega)$) = $\omega\epsilon_0\ \epsilon''_r(\omega)$ in terms of frequency was given by

$$\sigma(\omega) = \omega\epsilon_0 \frac{\omega_p^2\tau/\omega}{1+\omega^2\tau^2} \quad \text{(from equation (18))}$$

$$\sigma(\omega) = \frac{\epsilon_0\omega_p^2\tau}{1+\omega^2\tau^2} \tag{3.25}$$

From the above relations of permittivity and conductivity, it has been concluded that the i) below plasma frequency permittivity was mostly imaginary and metal acts as good conductor. ii) Near the plasma frequency, both the real and imaginary parts of permittivity were significant and metals were very loss. iii) At very high frequencies above the plasma frequency, loss vanishes and metals become transparent i.e weakly absorbers. These concepts explained by surface waves of metals.

3.5 Surface Waves on metals

Surface Waves were the waves that were travel on surface of material in longitudinal direction. Let us consider an interface between air and metal boundary (x=0) as shown in fig 3.10. The surface wave was propagating along the z-direction. The electric field has two components, one was along the direction of propagation (z-direction), and second one was along the x-direction. The amplitude of both components was maximum at the interface separating (x=0) two media and as x value increases (both in +x axis and –x direction) the amplitude of wave was decaying exponentially to zero value which depends on the propagation constant. Any conducting medium which has finite conductivity can support surface waves. In plasma physics these waves were called surface plasma waves. These waves were analysed as follows.

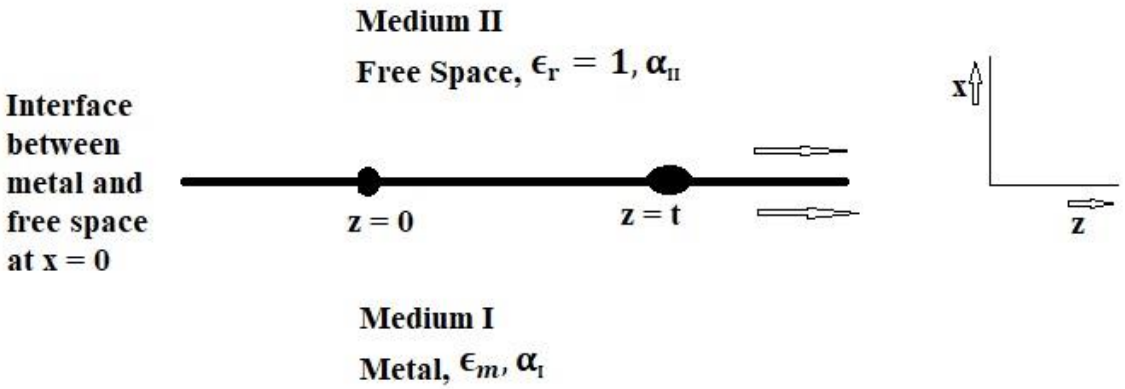

Fig 3.10: Interface between metal and free space.

Let us assume metal permittivity was ϵ_m and was given by

$$\epsilon_m = \epsilon_r - \frac{\omega_p^2}{\omega^2} \text{ (at high frequency)} \quad (3.26)$$

And electric field was of the form at z=0 was

$$E(z=0, t) = A\, e^{-i\omega t} \quad (3.27)$$

Electric field at z was given by

$$E(z, t) = E\left(z, t - \frac{z}{v_{ph}}\right) = A(x)\, e^{-i\left(\omega t - \frac{\omega}{v_{ph}} z\right)} \quad (3.28)$$

Let us assume

$$K_z = \frac{\omega}{v_{ph}} \quad (3.29)$$

Then

$$E(z, t) = E\left(0, t - \frac{z}{v_{ph}}\right) = A(x)\, e^{-i(\omega t - K_z z)} \quad (3.30)$$

As the wave has an x-component it should satisfies wave equation and to find the electric field in z-direction

$$\nabla^2 E_z + \frac{\omega^2}{c^2} E_z = 0 \text{ in free space } (x>0) \quad (3.31)$$

$$\nabla^2 E_z + \epsilon_m \frac{\omega^2}{c^2} E_z = 0 \text{ in conductor } (x<0) \quad (3.32)$$

$$\nabla^2 E_z = \frac{\partial^2 E_z}{\partial x^2} + \frac{\partial^2 E_z}{\partial z^2}$$ (by assuming field was uniform in y-direction) (3.33)

Let us find $\frac{\partial^2 E_z}{\partial z^2}$ from the equation (3.30)

$$\frac{\partial^2 E_z}{\partial z^2} = \frac{\partial^2}{\partial z^2} \left(\mathrm{A(x)} e^{-i(\omega t - K_z \mathrm{z})}\right)$$

$$= \frac{\partial}{\partial z}(\mathrm{i}K_z \mathrm{A(x)} e^{-i(\omega t - K_z \mathrm{z})})$$

$$= \mathrm{i}^2 K_z^2 \mathrm{A(x)} e^{-i(\omega t - K_z \mathrm{z})}$$

$$\frac{\partial^2 E_z}{\partial z^2} = -K_z^2 E_z \quad (3.34)$$

Substitute above value in equation (3.33)

$$\nabla^2 E_z = \frac{\partial^2 E_z}{\partial x^2} - K_z^2 E_z \quad (3.35)$$

Substitute above value in equation (3.31)

$$\frac{\partial^2 E_z}{\partial x^2} - K_z^2 E_z + \frac{\omega^2}{\mathrm{c}^2} \mathrm{E_z} = 0$$

$$\frac{\partial^2 E_z}{\partial x^2} - \left(K_z^2 - \frac{\omega^2}{\mathrm{c}^2}\right) E_z = 0 \quad (3.36)$$

Let

$$\alpha_{\mathrm{II}}^2 = K_z^2 - \frac{\omega^2}{\mathrm{c}^2} \quad (3.37)$$

Then equation (3.36) becomes

$$\frac{\partial^2 E_z}{\partial x^2} - \alpha_{\mathrm{II}}^2 E_z = 0 \quad (3.38)$$

The above equation has following solution

$$E_z = \mathrm{A_0}\, e^{-\alpha_{\mathrm{II}} x} e^{-i(\omega t - K_z \mathrm{z})}$$ in free space (x>0) (3.39)

Substitute equation (3.35) in (3.32) and to find the electric field in z-direction in conductor (x<0)

$$\frac{\partial^2 E_z}{\partial x^2} - K_z^2 E_z + \epsilon_{\mathrm{m}} \frac{\omega^2}{\mathrm{c}^2} \mathrm{E_z} = 0$$

$$\frac{\partial^2 E_z}{\partial x^2} - (K_z^2 - \epsilon_m \frac{\omega^2}{c^2})\, E_z = 0 \quad (3.40)$$

Let

$$\alpha_I^2 = K_z^2 - \epsilon_m \frac{\omega^2}{c^2} \quad (3.41)$$

Then equation (3.40) becomes

$$\frac{\partial^2 E_z}{\partial x^2} - \alpha_I^2 E_z = 0 \quad (3.42)$$

The above equation has following solution

$$E_z = A_0^1\, e^{\alpha_I x} e^{-i(\omega t - K_z z)} \text{ In conductor (x<0)} \quad (3.43)$$

But E_z was continuous at interface (x=0) of two medium then

$$E_z /_{x=} 0^- = E_z /_{x=} 0^+ \quad (3.44)$$

$A_0^1\, e^{i\alpha_I(0)} e^{-i(\omega t - K_z z)} = A_0\, e^{-i\alpha_{II}(0)} e^{-i(\omega t - K_z z)}$ (from equation (3.39), (3.43) and (3.44)

$$A_0^1 = A_0 \quad (3.45)$$

To find the E_x value, from the maxwell's equation

$$\nabla.(\epsilon_m E) = 0 \quad (3.46)$$

$$\nabla. E = 0$$

$$\frac{\partial E_x}{\partial x} + \frac{\partial E_z}{\partial x} = 0$$

$$\frac{\partial E_x}{\partial x} + iK_z E_z = 0$$

$$\partial E_x = -iK_z E_z\, \partial x$$

Integrating on both sides

$$\int \partial E_x = \int(-iK_z E_z)\, \partial x$$

$$E_x = -iK_z \int E_z \partial x \quad (3.47)$$

Electric field component (E_x) in free space was given by substituting E_z value (x>0) (from equation (3.39)) in equation (3.47)

$$E_x = -\,\mathrm{i}K_z \int \mathrm{A}_0\, e^{-\alpha_{\mathrm{II}} x} e^{-i(\omega t - K_z \mathrm{z})} \partial x$$

$$E_x = \frac{\mathrm{i}K_z}{\alpha_{\mathrm{II}}} \mathrm{A}_0 e^{-\alpha_{\mathrm{II}} x} e^{-i(\omega t - K_z \mathrm{z})} \quad \text{For x>0} \tag{3.48}$$

Electric field component (E_x) in conductor was given by substituting E_z value (x<0) (from equation (3.43)) in equation (3.47)

$$E_x = -\,\mathrm{i}K_z \int \mathrm{A}_0\, e^{\alpha_{\mathrm{I}} x} e^{-i(\omega t - K_z \mathrm{z})}\, \partial x \quad (\text{from equation (3.44) } \mathrm{A}_0^1 = \mathrm{A}_0\ )$$

$$E_x = \frac{-\,\mathrm{i}K_z}{\alpha_{\mathrm{I}}} \mathrm{A}_0 e^{\alpha_{\mathrm{I}} x} e^{-i(\omega t - K_z \mathrm{z})} \quad \text{For x<0} \tag{3.49}$$

At the interface of free space and metal (x=0), from equations (3.48) and (3.49) it can observe that E_x has two different components and they were in outer phase.

At the interface x=0, from the boundary conditions, $\epsilon_{\mathrm{eff}} E$ was continuous

So,

$$\epsilon_{\mathrm{r}} E_x/_{\text{medium II}} = \epsilon_{\mathrm{m}} E_x/_{\text{medium I}} \tag{3.50}$$

$$\frac{\mathrm{i}K_z}{\alpha_{\mathrm{II}}} \mathrm{A}_0 e^{-\alpha_{\mathrm{II}}(0)} e^{-i(\omega t - K_z \mathrm{z})} = \epsilon_{\mathrm{m}} \frac{-\,\mathrm{i}K_z}{\alpha_{\mathrm{I}}} \mathrm{A}_0 e^{\alpha_{\mathrm{I}}(0)} e^{-i(\omega t - K_z \mathrm{z})} \quad (\epsilon_{\mathrm{r}}=1 \text{ for free space})$$

$$\alpha_{\mathrm{I}} = -\,\epsilon_{\mathrm{m}} \alpha_{\mathrm{II}} \tag{3.51}$$

So it could be observed that at the interface between metal and free space the sign of the permittivity changed.

By squaring on both sides

$$\alpha_{\mathrm{I}}^2 = \epsilon_m^2 \alpha_{\mathrm{II}}^2 \tag{3.52}$$

Substituting equation (3.37) and (3.41) in above relation

$$K_z^2 - \epsilon_{\mathrm{m}} \frac{\omega^2}{\mathrm{c}^2} = \epsilon_m^2 \left(K_z^2 - \frac{\omega^2}{\mathrm{c}^2}\right)$$

$$K_z^2 (1 - \epsilon_m^2) = \epsilon_{\mathrm{m}} (1 - \epsilon_{\mathrm{m}}) \frac{\omega^2}{\mathrm{c}^2}$$

$$K_z^2 = \frac{\epsilon_m(1-\epsilon_m)\frac{\omega^2}{c^2}}{(1-\epsilon_m)(1+\epsilon_m)}$$

$$K_z^2 = \frac{\epsilon_m \frac{\omega^2}{c^2}}{1+\epsilon_m} \tag{3.53}$$

$$K_z = \frac{\omega}{c}\left(\frac{\epsilon_m}{1+\epsilon_m}\right)^{1/2} \tag{3.54}$$

This was called dispersion relation for surface plasma waves

Put above K_z^2 value in equation (3.37)

$$\alpha_{II}^2 = K_z^2 - \frac{\omega^2}{c^2}$$

$$\alpha_{II}^2 = \frac{\epsilon_m \frac{\omega^2}{c^2}}{1+\epsilon_m} - \frac{\omega^2}{c^2}$$

$$\alpha_{II}^2 = \frac{\omega^2}{c^2}\left(\frac{\epsilon_m}{1+\epsilon_m} - 1\right)$$

$$\alpha_{II}^2 = \frac{\omega^2}{c^2}\left(\frac{-1}{1+\epsilon_m}\right) \tag{3.55}$$

$$\alpha_{II} = \frac{\omega}{c}\left(\frac{-1}{1+\epsilon_m}\right)^{1/2} \tag{3.56}$$

Put above K_z^2 value in equation (3.41)

$$\alpha_I^2 = K_z^2 - \epsilon_m \frac{\omega^2}{c^2}$$

$$\alpha_I^2 = \frac{\epsilon_m \frac{\omega^2}{c^2}}{1+\epsilon_m} - \epsilon_m \frac{\omega^2}{c^2}$$

$$\alpha_I^2 = \frac{\omega^2}{c^2}\left(\frac{\epsilon_m}{1+\epsilon_m} - \epsilon_m\right)$$

$$\alpha_I^2 = \frac{\omega^2}{c^2}\left(\frac{-\epsilon_m^2}{1+\epsilon_m}\right) \tag{3.57}$$

$$\alpha_I = \frac{\omega}{c}\left(\frac{-\epsilon_m^2}{1+\epsilon_m}\right)^{1/2} \tag{3.58}$$

If E_x component amplitude decayed in away from interface x=0 as shown in fig 3.8, then α_I and α_{II} should be real and large quantity.

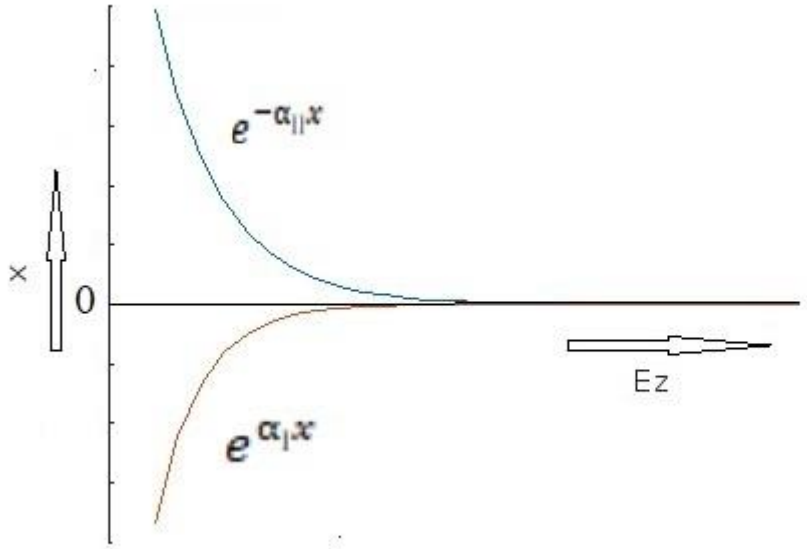

Fig 3.11: Field decay in x-direction.

From equation (3.58) α_l to be real then the value $\frac{-\epsilon_m^2}{1+\epsilon_m}$ under root should be positive, this condition was satisfied only when

$$(1 + \epsilon_m) < 0 \tag{3.59}$$

$$\epsilon_m < -1 \tag{3.60}$$

So metal should have negative permittivity then only field component vanish in x-direction rapidly as shown in fig 3.11 (skin depth phenomena) and this loss of energy was absorbed by the particle (free electrons) in metal by wave particle interaction process and Surface Plasmon waves were formed on the metal surface, on the other side of interface i.e in free space/dielectric energy travelled in the form of EM waves. By this way energy propagated in z-direction (longitudinal) at the interface in the form of EM waves and Surface Plasmon wave. So the field components were neglected away from the interface.

From the equations (3.26) and (3.59)

$$1+ \epsilon_r - \frac{\omega_p^2}{\omega^2} < 0$$

$$1+ \epsilon_r < \frac{\omega_p^2}{\omega^2}$$

$$\omega^2 < \frac{\omega_p^2}{1+\epsilon_r}$$

$$\omega < \frac{\omega_p}{\sqrt{(1+\epsilon_r)}} \tag{3.61}$$

Resonance will occur when $\omega = \omega_r$ which was called Surface Plasmon Resonance (SPR) frequency and was given by

$$\omega_r = \frac{\omega_p}{\sqrt{(1+\epsilon_r)}} \tag{3.62}$$

For gaseous plasma $\epsilon_r = 1$ then $\omega_r = \frac{\omega_p}{\sqrt{2}}$ and for metals ω_r was much less as ϵ_r greater than 1, so there was limitation that the surface wave has to travel along the interface between two medium the wave has frequency below the resonant frequency. This frequency was called surface Plasmon resonant frequency.

SPR was the resonant oscillations of the electrons that exist at the interface between any two materials where the real part of the permittivity changes sign across a metal–dielectric (free space) interface. The resonance condition occurred when the frequency of the incident photons matches with the natural frequency of oscillations of the surface electrons. By reducing the size of metal Nano particles to below the mean free path of electron of that metal, then metal nanoparticle allowed quantization in the Plasmon frequency of electron. When the Plasmon frequency was matched with EM radiated wave frequency then there was enhanced absorption resulting collective excitation of electrons of metal which in turn interact with EM radiation. These interaction phenomena results a travelling wave in longitudinal direction as the electrons displacement was in parallel to the direction of propagation.

Put ϵ_m (equation (3.26)) in equation (3.54)

$$K_z = \frac{\omega}{c}\left(\frac{\epsilon r - \frac{\omega_p^2}{\omega^2}}{1 + \epsilon r - \frac{\omega_p^2}{\omega^2}}\right)^{1/2}$$

$$K_z = \frac{\omega}{c}\left(\frac{\frac{\omega_p^2}{\omega^2} - \epsilon r}{\frac{\omega_p^2}{\omega^2} - (1+\epsilon r)}\right)^{1/2} \tag{3.63}$$

At $\omega = \omega_r$ the K_z value goes to high value then phase velocity of wave V_{ph}= $\frac{\omega}{K_z}$ was less than c. The diffraction of wave depends on the wave length of wave. Here as K_z was high, wavelength was less and then wave was less diffracted and travels along the surface.

Surface Plasmon effects were in the optical range, it was necessary to have surfaces that contain features < 400 nm. Hybrid surface Plasmon's were also produce by plucking holes in metals that had already a surface Plasmon [54] as shown in fig 3.12. The holes on metal surface increased the penetration of EM fields into the metal and resulting lower the frequency of present existing surface Plasmons. These surface plasmons were called the spoof surface plasmons as they merge one into the other.

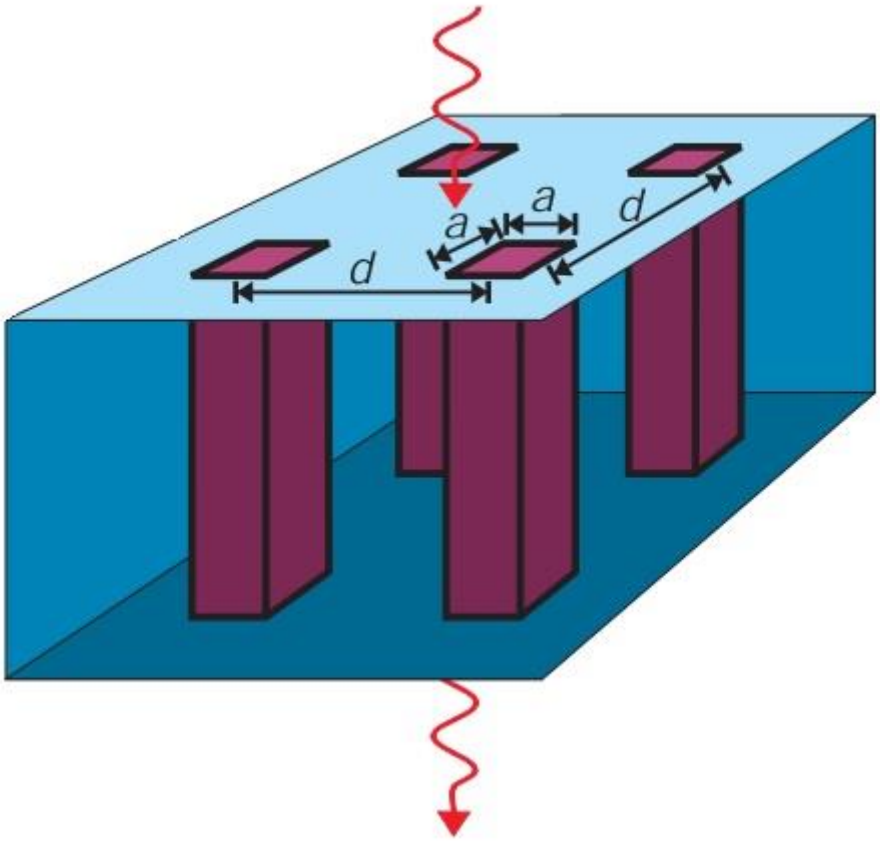

Fig 3.12: Metal with structured hole for SSPP

The holes spacing (d) must be less than the wavelength. To achieve these conditions, need of material which has size in the order of Nano scale and Plasmon frequency also in the order of microwave to terahertz. Graphene was a material which was suitable for these features. The electronic properties of graphene were as follows.

3.6 Electronic properties of graphene

3.6.1 Density of charge carriers

According to the authors [11], the free charge carriers or electrons in graphene appeared as massless Dirac fermions. A Fermi function or Fermi-Dirac distribution was used to characterise the distribution of fermions over an energy range since the properties of fermions were examined through their half-integer spin. At absolute zero temperature (T = 0 K), the chemical potential was referred to as the Fermi level, and states above this level were regarded as empty. The electron charge carriers migrated to higher energy levels when graphene's temperature rises, creating a filled and empty state. The findings demonstrate that as energy levels rise, the likelihood of an electron's occupancy falls. At the chemical potential, the probability of an electron's occupancy was 50%, or at E = μ_c, half the states were filled. The graphene's electron density can be calculated using the formula below when μ_c was more significant than thermal energy ($|\mu_c| >> k_BT$).

$$N_e = \frac{\mu_c^2}{\pi \hbar^2 v_f^2} \tag{3.64}$$

Where

μ_c = chemical potential

$\hbar$= reduced planks constant

v_f = velocity of fermions (10^6 m/s)

The minimum carrier density was anticipated to be equivalent to the thermally generated carriers at room temperature due to the electron-hole duality in suspended graphene, and as a result, the hole and electron mobilities were anticipated to be quite similar. However, it has been noted that the reported minimum carrier density for graphene typically ranges between 10^{11} and 10^{12} cm^{-2}, which was 10^7 times larger than copper [78].

3.6.2 Carrier mobility

The electron mobility of graphene determined how quickly an electric field drawn an electron in and how the electron travels through the sheet. Low carrier densities of 5 x 10^{11} cm^{-2} at low temperatures have been reported to have a mobility of 200000 cm^2 $(Vs)^{-1}$ in suspended graphene [79, 80]. At ambient temperature, however, the increasing resistivity causes the mobility to drop to 100,000 cm^2 $(Vs)^{-1}$ [81]. The enhanced resistivity may also have its roots in the metal contacts of voltage-gate architectures [82] and the edge state of

graphene ribbons. The mobility of graphene can be computed using considerations for resistivity and gate voltage as shown in [83, 84].

$$\mu = \frac{1}{N_e \rho} \tag{3.65}$$

Where

ρ = Graphene's electrical resistivity

N_e = Gate-induced electron density as described in equation (3.64).

Additionally, substrates have an impact on graphene's mobility [85]. Electron scattering mechanisms further restricted the mobility of graphene sheets on SiO_2 surfaces to 40,000 $cm^2 (Vs)^{-1}$ [86]. Graphene on a hexagonal boron nitride (h-BN) substrate has orders of magnitude greater mobility than SiO_2 [84]. The mobility can also be determined from the perspective of scattering mechanisms by [87].

$$\mu = \frac{e v_f^2}{\Gamma \mu_c} \tag{3.66}$$

Where

e = electron charge

v_f = velocity of fermions (10^6 m/s)

Γ = Scattering rate of electron = $\frac{1}{2\tau}$

μ_c= chemical potential of graphene.

3.6.3 Electron relaxation time

The length of time it takes for a charge distortion induced into a material as a result of electron collisions to relax to a uniform charge density was known as the relaxation time [88]. It was sometimes described as the typical duration between the two successive scattering occurrences and was represented in terms of scattering rate, as follows:

$$\tau = \frac{1}{2\Gamma} \tag{3.67}$$

Where

Γ= Scattering rate of electron

This scattering rate was sum of scattering due to the longitudinal acoustic phonon scattering rate, the impurity scattering rate and the surface optical phonon scattering rate in the graphene [89].

The relaxation time in graphene was a key component of the conductivity model for graphene and was dependent on the quality of the graphene sample [90]. The surface conductivity of an infinite graphene layer can be roughly calculated using the Drude like formulation in the lower frequency range (10 THz), where intra-band contribution predominates [91]. The relaxation time can be calculated in terms of carrier mobility and chemical potentials by ignoring the electron-phonon interaction that occurs over the inter-band and optical phonon threshold frequencies [92]. Fig 3.13 shows that the electron relaxation time was varied linearly according with chemical potential of graphene.

$$\tau = \frac{\mu \mu_c}{e v_f^2} \tag{3.68}$$

Where

μ = Mobility of charge carrier

e = electron charge

v_f = velocity of fermions (10^6 m/s)

μ_c= chemical potential of graphene

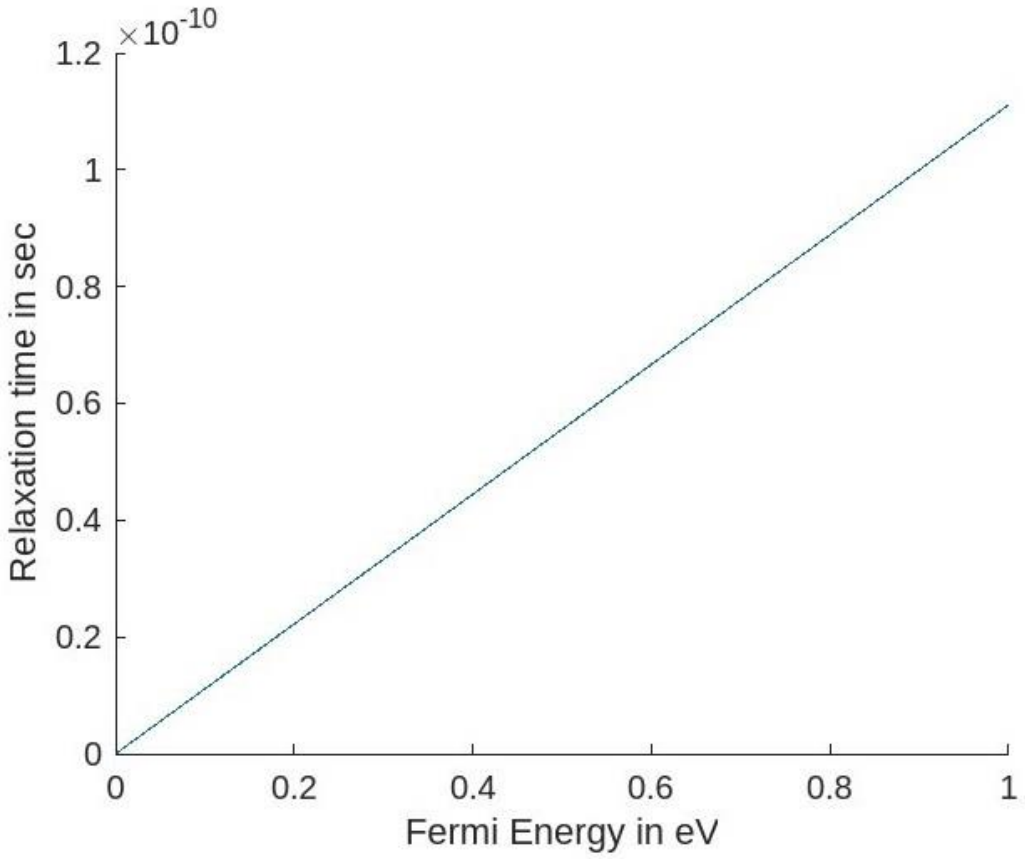

Fig 3.13: Graphene electron relaxation time versus chemical potential

Numerous studies have examined how graphene conductivity and, consequently, its radiation properties were affected by relaxation time. The relaxation time of graphene was predicted to be between 10^{-14} and 10^{-11} seconds [93]. In order to accurately characterise the graphene surface conductivity, it was necessary to also provide data on the relaxation time and chemical potential, which can be used to determine the doping level of the samples.

3.6.4 Fermi velocity

By regulating the energy gap of graphene, Fermi velocity played a very important role in the design of graphene-based Nano-devices [94].The application of graphene to electronics encourage researchers to look for ways to create energy gap in graphene's low-energy electrical structure. The charge carriers in graphene primarily behaved as massless relativistic particles with a conical energy spectrum $E = v_f \hbar k$, where v_f was the Fermi velocity, was the reduced Planck constant, and k was the wave vector. In this equation, v_f represents the effective speed of light. Coulomb interaction must be considered in graphene, though, because the energy spectrum was full of electronic states up to the Fermi energy.

The writers [95] carried out studies of the cyclotron mass in suspended graphene at carrier concentrations spanning three orders of magnitude highlighted that Fermi velocity could by altering the carrier concentration in graphene, 3 x 10^6 m/s. Additionally, the graphene material was the only one known to have features that were similar to those of the graphene material in terms of permittivity over such a broad frequency range, which can be utilised to tailor the electrical characteristics of the antenna. Because graphene's conductivity can be altered to resemble either a metal or a semiconductor, it was a great candidate for high frequency electronics. Generally speaking, the conductivity of graphene exhibits radically distinct behaviour at microwave and THz frequencies and basically follows a Drude-like pattern. [96]

3.6.5 Chemical potential

The level in the distribution of electron energies at which a quantum state has an equal chance of being occupied or vacant was known as the chemical potential of graphene. The amount of power that a graphene can absorb and, as a result, its resonance frequency, were trade-offs. As a result, it was reasonable to assume that altering the graphene chemical potential also has an impact on the material's electrical conductivity, which was one of the key elements affecting how well it radiated and provides the opportunity to tune the antenna resonant frequency [93]. The formula for chemical potential (approximate) was given by [51, 97].

$$\mu_c = \hbar v_f \sqrt{\left(\frac{\pi \epsilon_0 \epsilon_r V_b}{e t_s}\right)} \tag{3.69}$$

Where

$\hbar$= Reduced planks constant

v_f = Velocity of fermions (10^6 m/s)

ϵ_0 = Permittivity of free space

ϵ_r = Relative permittivity of dielectric

V_b = V_g- V_{dirac}= Biased voltage of graphene

V_g = Voltage applied to graphene

V_{dirac}= Graphene offset voltage caused by natural doping.

t_s = Thickness of dielectric layer

The graph in fig 3.14 showed that as bias voltage increased the chemical potential also increased. Thus, the charge carrier density or electrostatic bias voltage and thickness of dielectric layer can be used to readily change the chemical potential of graphene, allowing for the dynamic tuning of graphene's radiation properties as the real and imaginary components of conductivity were typically varied as the chemical potential varied.

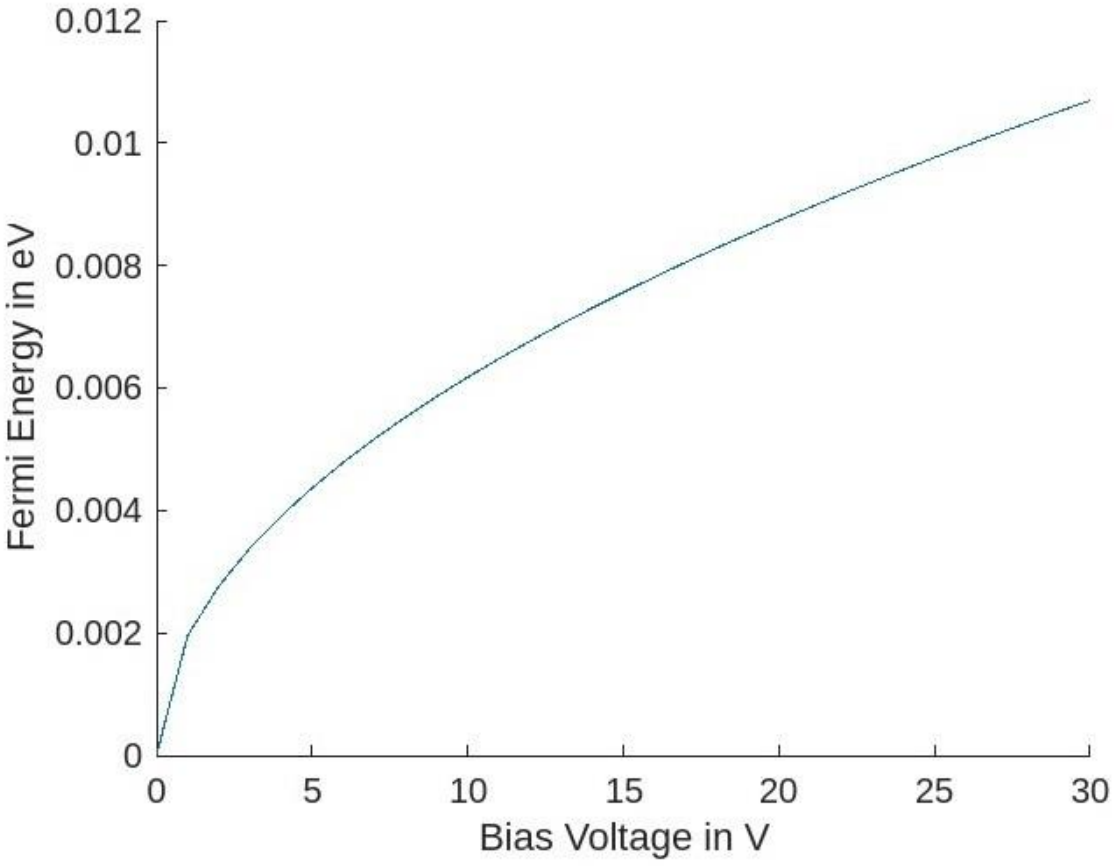

Fig 3.14: Graphene Fermi energy versus bias voltage.

3.6.6 Plasma frequency

In metals, when compared to the ions, the plasma's electrons naturally fluctuate at a certain frequency, which was known as plasma frequency. The plasma frequency of graphene was defined by following formula [98, 99]

$$\omega_p = \sqrt{\frac{e^2 \mu_c}{t_g \pi \hbar^2 \epsilon_0}} \tag{3.70}$$

Where

e = Charge of electron

μ_c= Chemical potential of graphene

t_g = Thickness of graphene

$\hbar$ = Reduced planks constant

ϵ_0 = Permittivity of free space

From the above equation, plasma frequency was also depends on the chemical potentials and graphene thickness. As number of graphene layers increased the plasma frequency will be decreased. The advantage of graphene was that its plasma frequency was tuneable as compared to other conductors like copper, gold and silver which have fixed plasma frequency.

3.6.7 Conductivity

Due to the material's adjustable conductivity, desired electromagnetic and mechanical qualities, which provide the provision of flexible and reconfigurable constructions, the material graphene was widely employed in a variety of microwave and terahertz applications. The main problem for employing graphene as a Nano component was to theoretically predict the new sophisticated graphene material that would have better high frequency qualities. Less loss, improved impedance matching, and high radiation efficiency were the specific features that demand attention, and as a result, changed electromagnetic absorption characteristics should be provided to be compatible with Nano devices based on electromagnetic properties. Electrons in the occupied energy levels of graphene absorb the energy from incident waves and become excited to higher energy levels as soon as electromagnetic energy was incident on the material. Within the band and between the bands, the electron will transition. As a result, both the intra-band and inter-band transitions contribute to graphene's actual conductivity. However, the surface conductivity of the graphene material was characterised by a quantum-dynamical inter-band mode and a semi-classical intra-band mode [100]. Therefore, the graphene surface conductivity was complex quantity (equation 3.71) and as a function of frequency has been calculated using Kubo's formula [96]. In this formula the surface conductivity of an infinite graphene film was expressed in terms of intraband and interband contributions, which, respectively, correspond to the intraband electron-phonon scattering process and the interband electron transition i.e The intraband conductivity converges to the Drude model at T = 0 K [101], while the interband conductivity was related to the creation and recombination of electron-hole pairs. Graphene conductivity expressed as

$$\sigma = \sigma' + i\sigma'' = \sigma_{intra} + \sigma_{inter} \quad (3.71)$$

If σ"> 0, graphene's interband conductivity becomes dominant, and surface Plasmon polariton with TE polarisation were supported. If σ" <0, graphene's intraband conductivity predominates, and surface plasmon polaritons with TM polarisation were supported [96]. The addition of impurities or the application of an electric field can altered the two-dimensional conductivity of graphene. Graphene's intraband and interband transitions shift a little bit when a gate voltage was applied. In this fashion, intraband transitions happen when the applied energy was less than the band gap of graphene, while interband transitions happen when the applied energy was greater than the band gap of graphene. This approach can alter the conductivity of graphene since these intraband and interband transitions directly affect its intraband and interband conductivities [99]. The 2D conductivity of graphene which derived from kubo formulation was as follows [96].

$$\sigma_g(\omega, \mu_c, \Gamma, T) = \frac{ie^2(\omega - i2\Gamma)}{\pi\hbar^2}\left[\frac{1}{(\omega - i2\Gamma)^2}\int_0^\infty E\left(\frac{\partial f(E)}{\partial E} - \frac{\partial f(-E)}{\partial E}\right)dE - \int_0^\infty \frac{\partial f(-E) - \partial f(E)}{(\omega - i2\Gamma)^2 - 4(E/\hbar)^2}dE\right] \quad (3.72)$$

Where

ω = Angular frequency

e = Charge of electron = 1.602*10^{-19} Coulombs.

$\hbar$ = Reduced planks constant = $\frac{h}{2\pi}$ = 1.054*10^{-34} JSec

Γ = Scattering rate of electron

T = Temperature = 300K

E = Energy

f (E)= Fermi distribution function

$$\text{f (E)= Fermi distribution function} = \frac{1}{\left[1 + e^{\frac{(E - E_f)}{k_B T}}\right]} \quad (3.73)$$

$\mu_c = E_f$ = Chemical potential or Fermi level of graphene

k_B = Boltzmann constant

First integral of above equation gives the intra band conductivity and second integral gives the inter band conductivity of graphene. After substituting equations 3.67 and 3.73 in 3.72 with assumption of time variations as exp (-jωt) in kubo derivation and solving the integrals, then

$$\sigma_{intra} = \frac{ie^2 k_B T}{\pi\hbar^2(\omega+i\tau^{-1})}\left[\frac{E_f}{k_B T} + 2ln\left(e^{\frac{-E_f}{k_B T}} + 1\right)\right] \quad (3.74)$$

$$\sigma_{inter} = \frac{ie^2}{4\pi\hbar} ln\left[\frac{2|E_f| - (\omega+i\tau^{-1})\hbar}{2|E_f| + (\omega+i\tau^{-1})\hbar}\right] \quad (3.75)$$

As discussed earlier Up to terahertz frequency the photon energy was very less and fewer than the Fermi level ($E_f \gg k_B T$) and interband transitions i.e carrier transition from valance band to conduction band cannot happen until EM energy was larger than two times the chemical potential [102]. If graph drawn between frequency to conductivity of graphene as shown in fig 3.15 for 3.74 equation with value shown in table 3.1, it can observed that the intraband conductivity tending zero when frequency goes to near optical regime. So graphene interband conductivity was neglected and intraband conductivity becomes drude like model as follows [103] at lower frequencies below optical frequency.

$$\sigma_{intra} = \left[\frac{e^2 E_f}{\pi\hbar^2}\right] \frac{i}{(\omega+i\tau^{-1})} \quad (3.75)$$

Table 3.1: Parameters used in graphene intraband conductivity and their values.

Sl.No	Symbol	Parameter	Value	Units
1	e	Charge of electron	$1.602*10^{-19}$	Coulombs
2	k_B	Boltzmann constant	$1.38*10^{-23}$	J/K
3	T	Ambient Temparature	300	Kelvin
4	Ƭ	Relaxation time	10.85	Pico sec
5	E_f	Chemical potential	9.8	meV

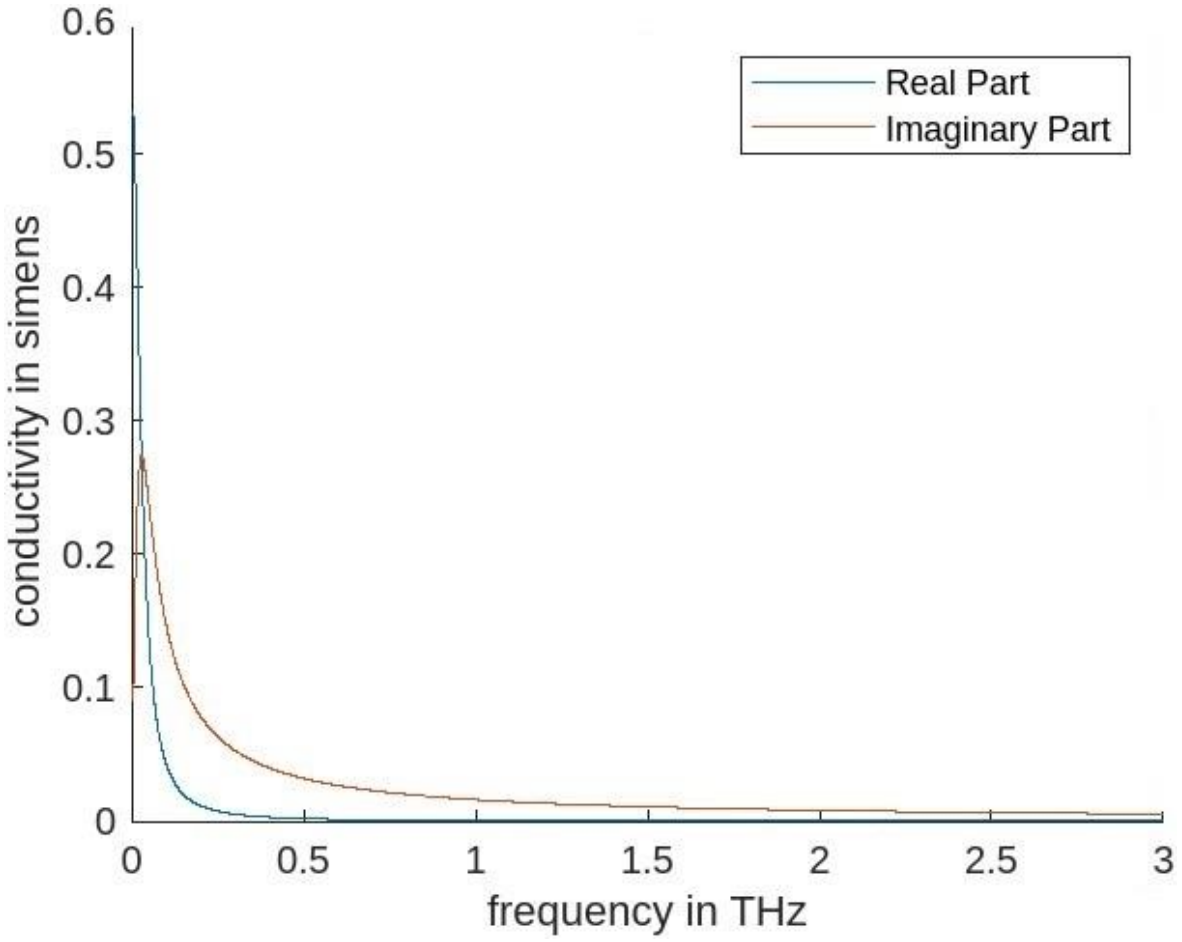

Fig 3.15: Graphene intraband conductivity weds frequency.

From the graph it was noted that the real part of conductance was dominated than imaginary part of conductance in gigahertz range, as frequency increases imaginary part of conductance was dominated than real part of conductance. There different formulas were developed for graphene conductivity and comparative analysis was done for accuracy of kubo formula for plasmonic of graphene and finally chosen equation 3.73 for our work.

3.7 Fabrication methods of graphene

In terms of graphene production methods, top-down and bottom-up approaches were used [104] as shown in fig 3.16. In that the sub classification was shown in tree chart fig 3.17.

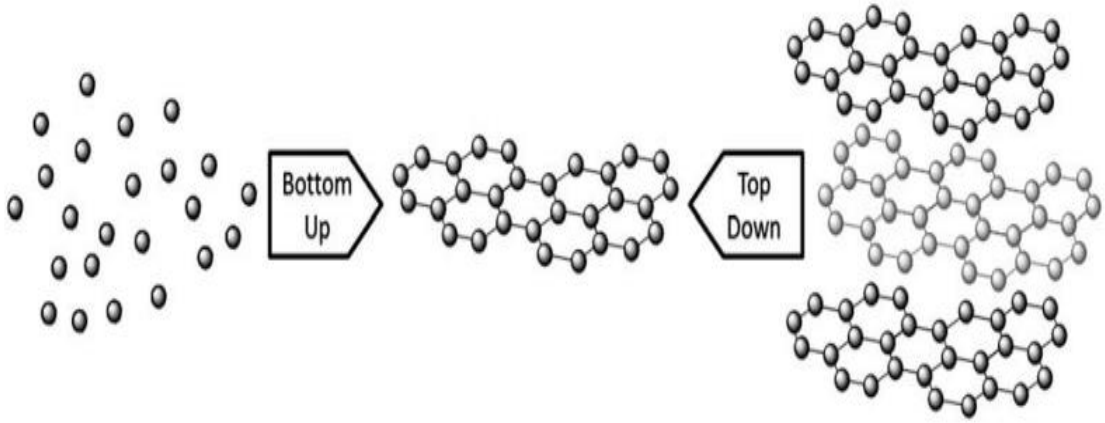

Fig 3.16: [105] Top-down and bottom-up approaches of graphene synthesis.

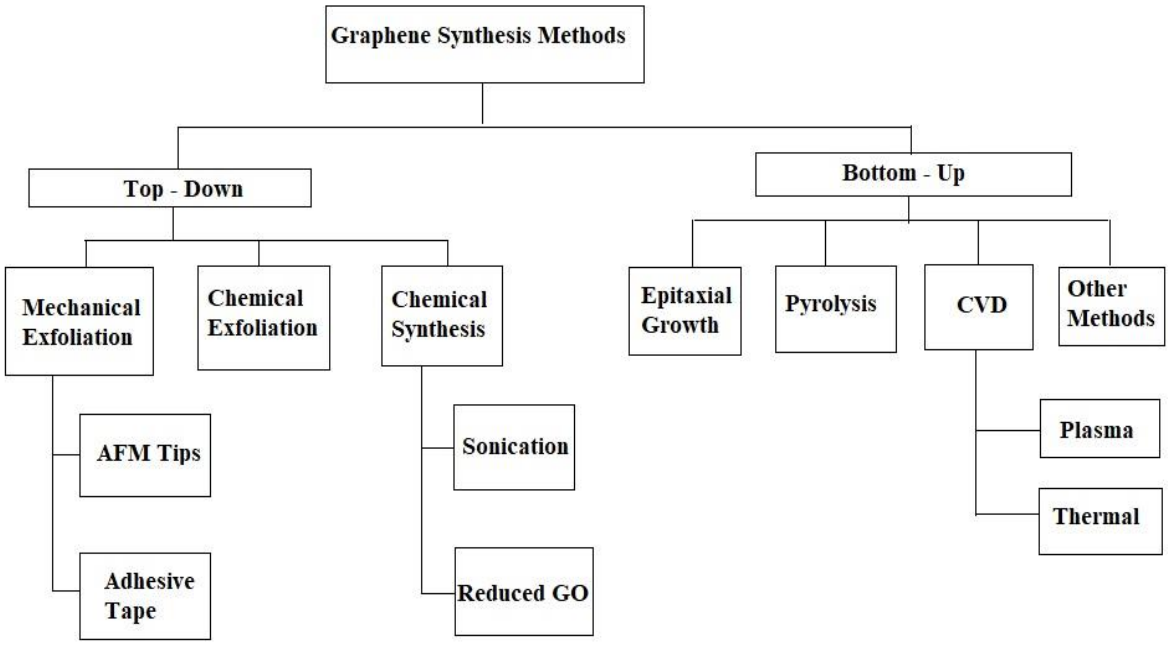

Fig 3.17: Different synthesis technics of Graphene.

3.7.1 Top-down approach

A natural carbon substance made up of stacked layers of graphene sheets, bulk graphite was a natural carbon material that was prepared via a top-down approach in most cases [105]. For example, mechanical exfoliation [106], electrochemical exfoliation [107], liquid-phase exfoliation [108], exfoliation and reduction of graphite oxide [109] were some exfoliation techniques that can be used to overcome the van-der-Waals force between

adjacent graphene sheets. The adhesive tape method of mechanical exfoliation was shown below fig 3.18 which was used in 2004 in lab of MIT [110].

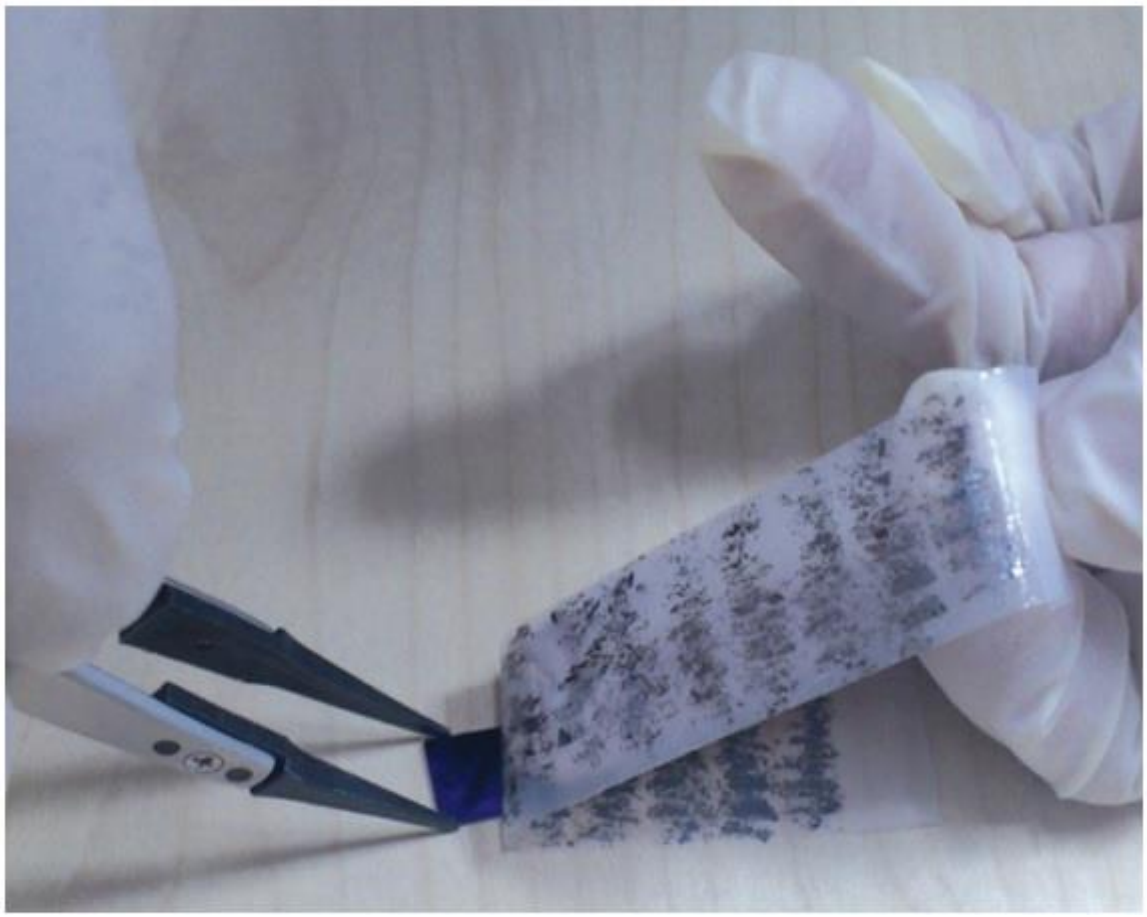

Fig 3.18: [110] Graphene exfoliation by adhesive tape.

The three other types of exfoliation mechanisms, with the exception of mechanical exfoliation, suffer from unregulated quantity in addition to limited sample sizes, which significantly affected the characteristics of graphene. Key challenges in this area included effectively separating the layers without damaging the sheets, and preventing re-agglomeration of the sheets once the layers have been exfoliated. Top-down approaches generally suffer from low yields, numerous steps, and have the common disadvantage that natural graphite must be mined and processed before use because it was a finite resource that was on the European list of scarce materials and requires mining and processing prior to use. Graphite can be produced synthetically under high temperature conditions, but it was not generally suitable for graphene production due to poor levels of graphitisation and irregular morphologies.

3.7.2 Bottom-up approach

The other method known as bottom-up entailed the manufacture of graphene from different gases containing carbon atoms, primarily through chemical vapour deposition, epitaxial growth [111], hummer method [28], pyrolysis [104], and arc discharge and unzipping carbon nanotubes were comes under other methods. In Figure 3.19, a schematic of CVD graphene process steps were displayed, in first step hydrocarbon molecules were decomposed, then desorbs was going on and finally carbon atoms were grown to form the graphene [112].

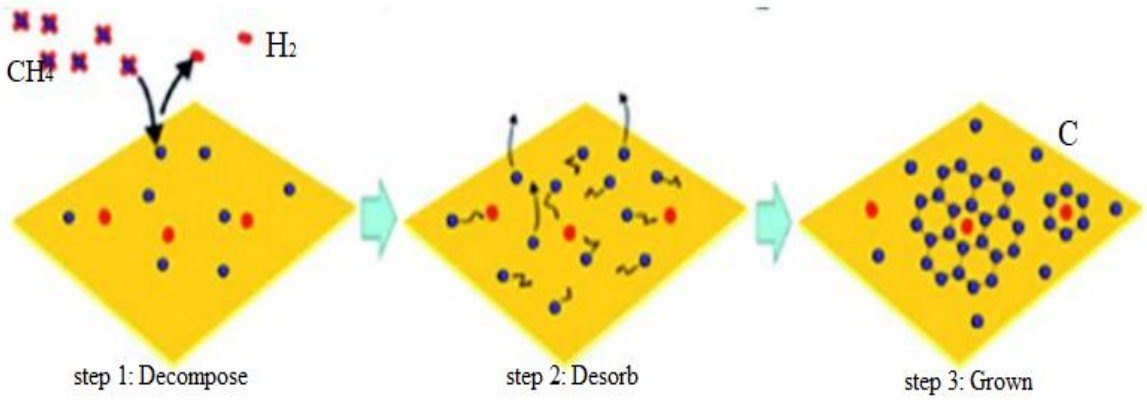

Fig 3.19: [112] Graphene growth process using CVD.

These bottom-up techniques typically demanded high temperatures because in order to generate high-quality material, high levels of graphitization must be encouraged. Although the processes involved were frequently straightforward, the material produced sometimes has higher degrees of imperfections than was seen with top-down approaches. Bottom-up approaches can be used to produce large area graphene films on certain substrates in addition to creating graphene Nano sheets. The chemical vapour deposition was discussed in next chapter.

3.8 Characterization of graphene

Characterization of graphene was a crucial component of graphene research and study. Characterizations involve studying the shape, characteristics, flaws, and layers of graphene using measurements at the microscopic and spectral levels [113, 114]. Characterization techniques include scanning electron microscopy (SEM), transmission

electron microscopy (TEM), Raman spectroscopy [115], atomic force microscopy (AFM), X-ray diffraction (XRD), and spectroscopy (UV-Visible) [116].

SEM was employed to examine the graphene's morphology. SEM imaging offers benefits include the ability to spot contaminants, folds in graphene, and discontinuities throughout the synthesis process. Its ability to resolve extremely thin layers of graphene was however constrained. The most popular method for examining the degree of structural complexity and number of sheets in graphene was the transmission electron microscope (TEM). Raman spectroscopy can be used to examine graphene layers and structural quality [117]. When the material's molecular vibration contacts with the mono-chromatic Raman spectroscopy radiation, the radiation shifts due to scattering [118]. In graphene, there were three primary peaks that may be seen: the D, G, and 2D peaks. A D peak at 1350 cm^{-1} was seen, indicating sp^2 hybridization abnormality [119]. The Raman spectrum for single, bilayer, three layer and four layer graphene on different substrates like quartz, SiO_2 / Si was shown in fig 3.20. The G peak was at 1580 cm^{-1}, which corresponds to lattice vibration, and the 2D peak was at 2700 cm^{-1}, which results from second-order Raman scattering at the Dirac point and as number of layers increases 2D peak was broaden [1120]. Because of the increased defect intensity's acoustic scattering, an increase in graphene disorder raised the I_D/I_G ratio. The I_D/I_G ratio, however, fallen as the carbon structure becomes more amorphous [121]. Due to the stretching of the C-C bond, graphene's Raman spectrum, often known as the G band, displays the G mode [122]. Strong peak values at 1580 cm-1, a first-degree Raman spectrum-allowed signal arising from the zone's centre (photon wave vector q = 0), were used to identify it. The defining number of layers of graphene was done by calculating the I_{2D}/I_G ratio, the I_{2D}/I_G value was between $2 < I_{2D}/I_G < 3$ then its monolayer, $1 < I_{2D}/I_G < 2$ then it was bilayer graphene and $I_{2D}/I_G < 1$ for multilayer graphene [123].

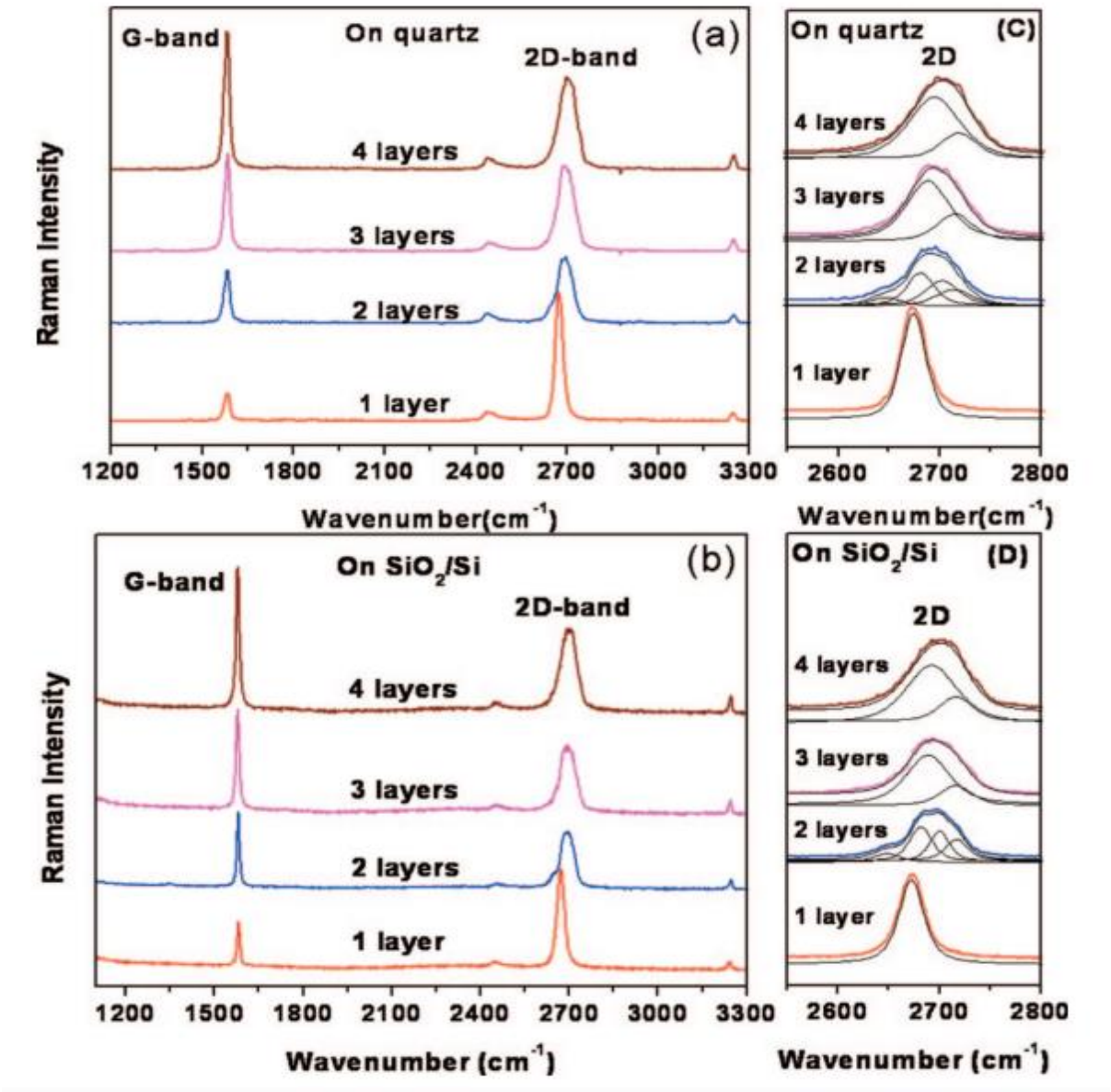

Fig 3.20: [120] Raman spectra of different layered graphene on a) Quartz substrate, b) SiO_2 / Si substrate, Broadening of 2D peak as number of layers increased on Quartz substrate (c) And on SiO_2/Si substrate (d).

The primary purpose of the X-Ray Diffraction method was to determine the substance's phase based on cell dimension units [124]. When X-Ray Diffraction was taken, Graphite has a prominent and significant diffraction spike at a temperature of 26.6 degrees. When oxygen molecules were present, the peak changes to 13.3 degrees. There was no peak following fabrication, proving that graphene was produced [125]. The surface structure and the thickness of graphene were assessed using atomic force microscopy (AFM) [126]. A tiny cantilever was used in an AFM to scan the surface of a specimen and produce images. The cantilever was bent when it was precise Nano-scale tip made contact with a surface. This

modified how much laser light returns onto the photodiode. Then the measured cantilever height tracking on the surface was used to alter the cantilever height to reactivate the response of the signal. The FTIR spectroscopy was discussed in later chapter.

3.9 Basics of Metasurface

3.9.1 Introduction to artificial materials

Metasurface was artificial 2D structured negative refractive indexed Metamaterial. Let us start with the history of artificial materials, the first artificial dielectric was developed by Kock in 1950s, later Pendry et.al developed a negative epsilon material with thin wire structure in 1998 [127]. Pendry also developed artificial magnetic material constructing from non-magnetic conducting sheets [128]. Let us consider electric material on x-axis and magnetic materials on y-axis as shown in fig 3.21.

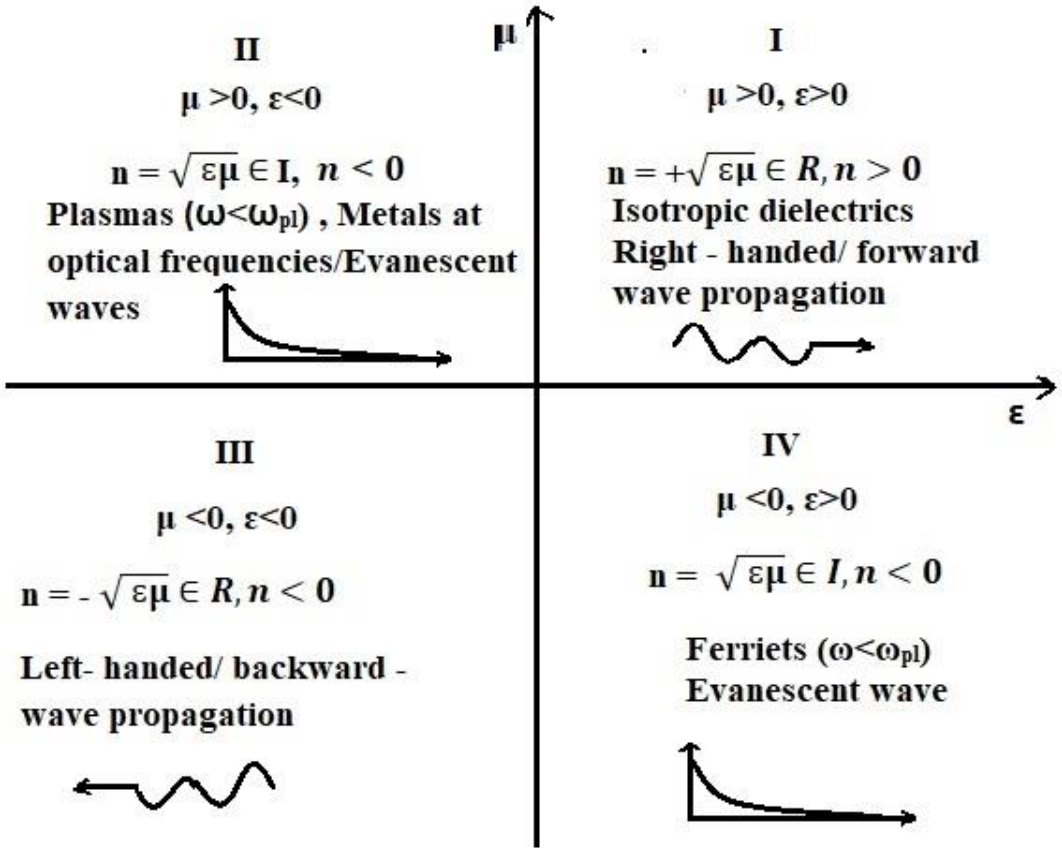

Fig 3.21: Response of different refractive index materials when EM wave incident on it.

In the first quadrant the materials whose permittivity and permeability both positive were isotropic dielectric materials, so they have positive real valued refractive index with

property to forwarded the incident EM waves, and the direction of pointing vector followed the right hand thumb rule, So they also called Right handed materials. In second (metals at optical frequency or artificial metals) and third (ferromagnetic materials or artificial magnetic conductors) quadrants which have negative permittivity, positive permeability and positive permittivity, negative permeability respectively resulting negative imaginary refractive index with property of evanescent wave. In all the above three cases, materials were naturally available, but in fourth quadrant there was no natural material available which has permittivity and permeability both negative. This negative value led to negative real valued refractive index that gave backward wave propagation for EM incident waves which was explained by generalised snell's law and opened a new era of artificially developed materials.

3.9.2 Metamaterials

It was a well-known fact that when an electromagnetic wave interacted with an integrated medium, its components experienced electric and magnetic polar moments. The effective permittivity and permeability of the composite medium were directly correlated with the aforementioned dipole moments. Materials with unique electromagnetic responses can be created because the creator was able to regulate the dimension, density, form, and orientation of the inclusions. Metamaterials were the name given to these manufactured materials. Such materials can have negative readings for both relative permittivity and permeability when the constituent elements were resonant. It must be emphasised that only highly resonant pieces can have a negative in value refractive index. This was as a result of "resonances having the property that their phase response reverses as frequency changes around the resonance." [129].

The Lorentz classic-theory can be used to explain the electromagnetic properties of metamaterials. According to this model, a field of electromagnetic radiation behaves as a damped harmonic oscillator around an electron. The Lorentz model was transformed into the Drude model when the restoring force was minimal. Within a broad frequency range, the Drude model permitted negative permittivity and permeability values. This characteristic makes the Drude model occasionally more advantageous for simulations than the narrowband Lorentz model [130].

Relative permeability and permittivity values can be negative in metamaterials with resonant individual constituents. The refraction angle was thus made negative by these left-hand materials, in accordance with the law of Snell's of refraction, causing the incident and

refracted waves to lie on the exact same side of the normal. Negative refraction was the name given to this occurrence. Light and other electromagnetic waves can be completely controlled by negative refraction in all four quadrants of a Cartesian plane. Metamaterials have numerous potential uses due to their peculiar quality that could not have been achievable if solely employing normally occurring materials [130]. The phase difference across the slab of this medium was zero when left handed and positive indices materials were put together. The variation in phase could be managed by combining dual positive and dual negative metamaterials. It can be demonstrated that the phase difference across the material was zero due to the refractive index and thickness ratio, not the entire thickness [130]. This demonstrated that the phase propagation in the positive index component of the slab was compensated by the slab's negative index part [131]. The focused resonance that developed at the interface of such two materials was another fascinating phenomenon that may be seen when mixing positive and negative indices materials [132]. The aperture-related resonance in a conventional waveguide can be replaced by a contact resonance, also known as a surface wave plasmon, allowing for the creation of sub-wavelength thin waveguides. Such guide's dispersion relationship was independent of total thicknesses and also depends on the thicknesses ratio [133, 134].

A superlens may also be created using metamaterials having a refractive index that was -1 on the negative side [135]. A superlens, referred to as a perfect lens, overcomes the constraints placed on focussing by wave optics (for a conventional lens, the area available for focussing energy was strictly limited to squares of wavelength). This was because, in a naturally existing medium, the amplitude of evanescent waveforms decayed exponentially, while LH materials increased its amplitude. Since evanescent waves didn't convey any energy, their structure continued to abide with the law of conservation of energy. The characteristic impedance, which was the combination of the ratio between permittivity and permeability, remains positive even though the refractive index was negative, so there were no echoes at the user interfaces and no (mismatch) energy losses throughout the entire phenomenon [135, 136].

3.9.3 Metasurface

The two-dimensional or plane analogues of metamaterials were called metasurfaces. Their electric and magnetic polarizabilities can be used to describe their reaction, just like with metamaterials. They were sometimes referred by the term metafilms in the works of

literature [137]. Because of its unique permittivity and permeability figures, metamaterials were able to regulate how light moves through space, but they also influence electromagnetic waves by taking advantage of this effect. In contrast to metasurfaces, which attempt to control the wave over a single, very thin layer, this can led to a complex, bulky structure [138,139].Metasurfaces were therefore fewer in size and may have less loss in their structures due to their two-dimensional shape [140]. Metamaterials were also challenged to manufacture due to their 3D character. An incredibly promising replacement was provided by metasurfaces. Metasurfaces were simple to produce using planar fabrication equipment because of its planar structure [141]. When compared to the production of intricate 3D metamaterials, the flat fabrication approach was likewise quite affordable [142]. Metasurfaces can be easily integrated into other devices because they were material with two dimensions. This makes them a standout component of nanophotonic networks and enables them to be used on chip photonics [143].

From the above discussions there must be phase uncertainty occurred at resonance condition (from the drude model of metals discussed in previous sections) so that negative refractive index can be created artificially. The physics behind this phase sudden phase variation of metasurface was explained by generalised snell's law of reflection and refraction. Let us consider an artificial surface which divided the two materials boundary as shown in fig 3.22. The two rays were incident on the surface with incident angle $\boldsymbol{\Theta_i}$ as shown with phase difference on the surface was ϕ and $\phi+d\phi$ where the rays crossed the surface with dx length between them and refractive indices of two mediums were n_i and n_t.

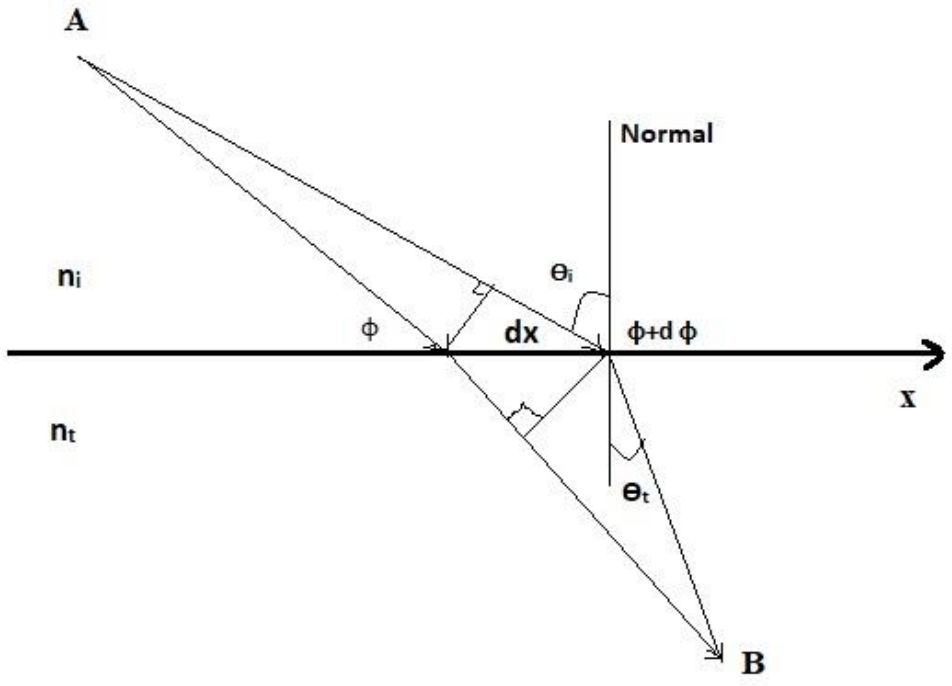

Fig 3.22: interface between two media that was constructed artificially to introduce abrupt phase shift for incident ray which depends on the position along the interface.

By using the law of Fermat [144,145], it may re-examined the rules of refraction and reflection when there was a sudden phase shift, also known as a phase uncertainty at the boundary between two mediums. Considering that the two routes were incredibly near to the real light path consequently, there was no variation in phase between them. Then

$$(k_o n_i \sin \theta_i dx + (\phi + d\phi)) - (k_o n_t \sin \theta_i dx + \phi) = 0 \qquad (3.76)$$

Where k_o wave number = $2\pi/\lambda_0$

The equation results in the generalised Snell's law of refraction if the phase gradient across the interface was intended to be constant and after rearranged the equation

$$n_t \sin \theta_t - n_i \sin \theta_i = \frac{\lambda_0}{2\pi} \frac{d\phi}{dx} \qquad (3.77)$$

Equation 3.77 suggested that the refracted ray can have any direction as long as an appropriate continuous gradient of phase irregularity was introduced across the interface. Both of the angles of incidence $\pm\theta_i$ result in distinct values for the angle of refraction due to the non-zero phase difference in this modified version of Snell's equation. Therefore, if $n_t < n_i$, there were two potential critical angles of total internal reflection.

$$\theta_c = \sin^{-1}\left(\pm\frac{n_t}{n_i} - \frac{\lambda_0}{2\pi n_i}\frac{d\phi}{dx}\right) \quad (3.78)$$

In the same way for reflection

$$\sin\theta_r - \sin\theta_i = \frac{\lambda_0}{2\pi n_i}\frac{d\phi}{dx} \quad (3.79)$$

Where θ_r was angle of reflection and above equation showed that there was nonlinear relation between θ_r and θ_i and critical angle was given by (after this angle wave became evascent)

$$\theta_c = \sin^{-1}\left(1 - \frac{\lambda_0}{2\pi n_i}\left|\frac{d\phi}{dx}\right|\right) \quad (3.80)$$

All of the incoming energy went into the unnatural reflection and refraction because it was assumed in the aforementioned calculation that ϕ was a constant function of position across the contact. This discreteness, still suggested the existence of continuously reflected and refracted rays which adhere to the standard laws of reflection and refraction i.e put $d\phi/dx = 0$ in Equation 3.77 then

$$n_t \sin\theta_t - n_i \sin\theta_i = 0$$

$$\text{i.e } n_t \sin\theta_t = n_i \sin\theta_i \quad (3.81)$$

From the above equation if $n_t$was negative for artificial materials as they have both permittivity and permeability negative, then θ_t should be negative to satisfy snell's law. Since in designs, an array of optically slim resonators were used together with subwavelength separation to produce a phase shift along the interface, the energy of the rays that were strangely reflected and refracted was controlled by the distance that separates the resonators, So distance between resonators played major role, if the distance was more, then phase reversal property may altered. The amplitudes of the radiation that was scattered from each resonator were also assumed to be the same, resulting in plane waves for the reflected and refracted rays. Through proper resonator design, the equal-amplitude constraint and constant phase difference across the interface can be achieved. These resonators were also called Meta atoms. The resonance of the individual meta-atoms was what causes the metasurfaces negative index. This characteristic put metamaterials in order inherently dispersive, making their electromagnetic (EM) characteristics most sensitive to variations in their operating

frequency and limiting their bandwidth. To get the more homogeneity in the EM wave characteristics, the design of resonator should also give same characteristics.

The term "metasurface" referred to a periodic (or aperiodic) arrangement in which both the thickness and repeatability of the constituent parts (scatters) were relatively tiny in relation to the operating wavelength i.e thickness must be less than one tenth of wave length and size less than one fourth of wave length. These 2D structures may also be further subdivided into metascreens and metafilms, which refer to independent, individual scatters and reflective screens, respectively [140]. The spatial distribution of each of the scattering elements played a crucial role in defining how a surface responds. The metasurfaces set themselves apart from conventional FSS with this characteristic. Individual components (periodicity) in a conventional FSS have the order of magnitude of the working wavelength (typically half wavelength). The fact that each component of a metasurface was sub-wavelength was another way that metasurfaces and FSSs differed from one other. Building blocks for metasurfaces can be thought of as traditional homogeneous structures because of its sub-wavelength nature, which makes it possible to characterise their reaction with useful parameters. Because a metasurfaces area was narrow, its fields and polarisations must be averages of its surface fields [145]. All single unit cells may be spatially altered because the metasurfaces reaction varies depending on the localised behaviour of every cell [147]. Wave fronts and metalenses can be created using such changes. Wave fronts spanning from microwave to visual size can be sub-wavelength resolved thanks to the miniaturised individual "meta-atoms" of the metafilms. The ability to behave like homogeneous or almost homogeneous sheets was another characteristic of metasurfaces [148]. The electromagnetic wave field components can be tailored via metasurfaces. Since the field polarizabilities of metasurfaces may be tailored to coincide with their impedance, they can have minimal mismatch losses [149, 150]. From the above discussion, metasurface property was completely depended on the individual unit cell property and distance between them. The more the Meta atoms less distance between them in the metasurface gave the more resultant homogeneity in property.

The main applications of metasurfaces were FSSs, metalenses, antennas and in EMI fields, some of them were discussed till now. The shape of unit cell found in literature were straight element, 3-legged, anchor, Jerusalem cross, different structured spirals, various loops, normal shaped patches and mixer of four leg loaded Jerusalem cross. The designing and

testing of a graphene metasurface with mixer of four-leg loaded Jerusalem cross, which reflected X-band frequencies, was done in this work.

CHAPTER -4

CVD GROWN METHOD and FTIR SPETRUM OF GRAPHENE

4.1 Chapter Overview

In section 4.2 the discussion was about the CVD method of preparation of graphene in detail and finally testing of graphene using FTIR spectroscopy with result were presented in section 4.3.

4.2 CVD method of preparation of graphene

4.2.1 Brief discussions on CVD grown graphene

Since 2008, the chemical vapour deposition (CVD) technology has been successfully used to create graphene [151]. An effort has been taken to increase its capability over the past fifteen years. Today, CVD was thought to be the most widely used and reasonably priced way of producing huge areas of graphene. Additionally, the synthetic graphene was easily transferable to other substrates. Applications for CVD graphene have multiplied [152].

The CVD process first entailed the breakdown of hydrocarbon gases over the use of transition metals, like methane (CH_4), acetylene (C_2H_2) and ethylene (C_2H_4), [152]. In addition to serve as substrates for reactions, transition metals could also function as facilitators that lower reaction temperatures [153]. By employing a copper substrate, for instance, the temperature during the thermal breakdown can be lowered from 1200 °C to 900 °C [154]. Transition metals came in a variety of possibilities, including nickel (Ni), copper (Cu),iridium (Ir), palladium (Pd), ruthenium (Ru), platinum (Pt) and cobalt (Co) [155-161]. Ni and Cu were two of these metallic transitions that were inexpensive and frequently used in CVD techniques [152]. However, since Ni has significantly higher carbon absorption than Cu, the growth mechanisms on Ni and Cu were distinct. It has been demonstrated that in high-concentration hydrocarbon gas with the lengthy development time, only a limited number of atoms of carbon can be dissolved in Cu [162]. Multi-layered graphene was grown on copper coated Si/SiO_2 by using atmospheric pressure chemical vapour deposition which was used for hydrogen sensing purpose [163]. The procedure mentioned in [163] for fabricating graphene on Si/SiO_2 and on cu in our lab was as followed.

4.2.2 Preparation of sample

The work was started with by cleaning of substrate. The substrates shown in the fig 4.1 with maximum sizes 1cm x 1cm should be taken so that it can put in furnace. The Si/SiO_2 substrate was first cleaned by acid process cleaning.

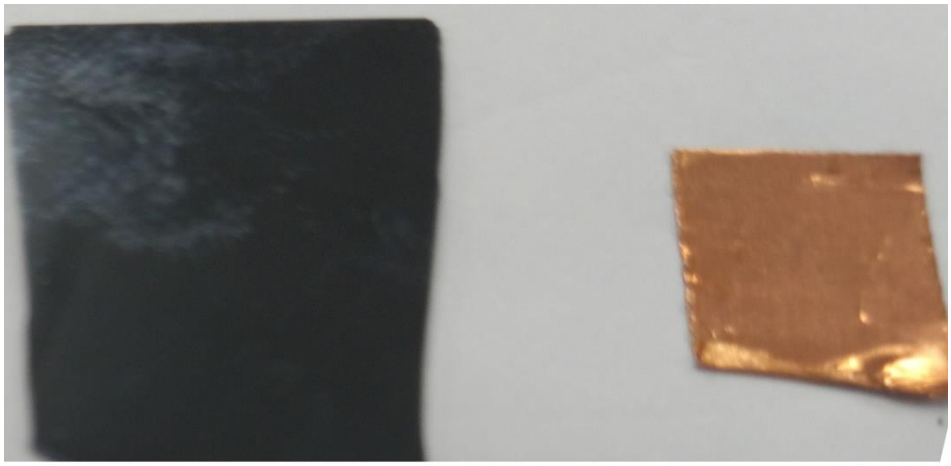

Fig 4.1: (a) Si/SiO_2 substrate, (b) Copper film substrate.

- In this method kept substrate in Trichloroethylene and boil it for 5 minutes, then sample was put into liquid of ultrasonic cleaner for three minutes to eliminate the dust particles from wafer.
- Then sample was put into acetone and boil for five minutes, after that again clean in ultrasonic cleaner for three minute to remove oil and grease if any.
- The inorganic compounds (if any) were removed by keeping sample in mixer of hydrogen peroxide and sulphuric acid (1:1) for 10 minutes in reaction chamber, then sample was cleaned by de-ionised (DI) water.
- The organic compounds were eliminated by keep the sample along with ammonium hydroxide (5sccm) in 4 minutes heated mixer of H_2O and H_2O_2 (1:1), keep for 10 min, then clean the sample with DI water.
- The sample was put in heated mixer of HCL, H_2O and H_2O_2 (6:1:1) for 10 minutes to remove alkaline compounds in sample.
- Now the sample was ready for keeping in CVD reactor, this step was followed for Si/SiO_2 substrate and for copper thin films substrate was cleaned by HCL and acetone.

4.2.3 CVD growth

- The arrangement of CVD system was shown fig 4.2.

Fig 4.2: Fabrication of graphene with CVD method.

- The cleaned sample of substrate was loaded into furnace.
- Then vacuum the furnace by using vacuum system still pressure meter shows low reading i.e below 0.5Ps.
- Meanwhile programme the temperature control programmer according to our requirement i.e in session 1 set temperature 1000^0C with time one hour thirty seven minutes as shown in fig 4.3, in session 2 kept temperature 1000^0C for fifteen minutes in first experiment and kept for eight minutes in second and third

experiments. In session 3 set temperature 500^0C for one hour forty minutes. In session 4 set temperature 200^0C for thirty minutes and for remaining sessions set all values to zero.

Fig 4.3 (a)

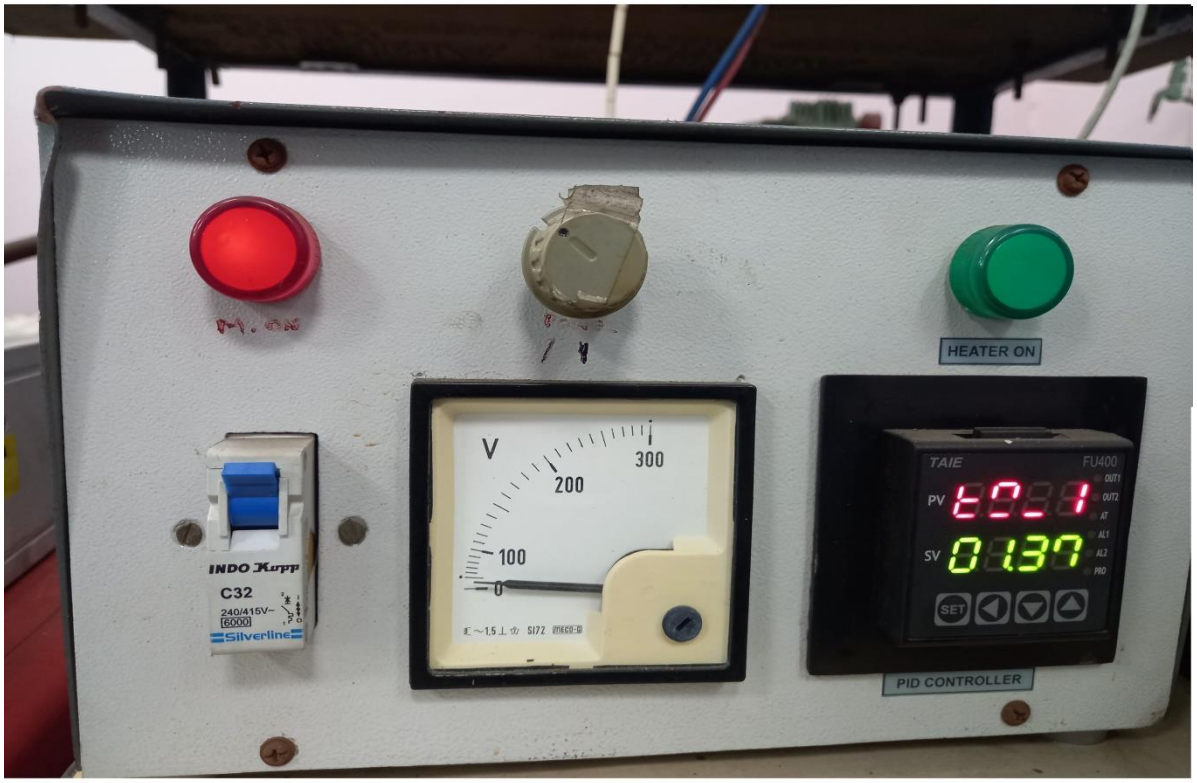

Fig 4.3 (b)

Fig 4.3: (a) Temperature setting, (b) Time setting in the Temperature controller.

- After pressure became low, close the outer air flow nob, then switch on the temperature controller to raise the temperature of furnace to 1000^0C, at the same time start flow of hydrogen (25sccm) and nitrogen (500sccm) into furnace from cylinders through MKS mass flow meter which measured the gas volume and were controlled by MKS mass flow controller.
- The temperature raising rate of furnace was set at 10^0C /min in temperature control programmer i.e it took 97min to raise the temperature of furnace to 1000^0C.
- After reaching temperature to 1000^0C immediately gas flow rate were changed to 5sccm:300sccm of hydrogen and nitrogen (both 99.99% purity gases) respectively using gas flow controller and methane gas (99.99% purity gas) of 15sccm sent into furnace for 15minutes (this time was called growth time, for second and third experiments it was 8minutes only). During This time decomposition of methane molecules was done and hydrogen atoms were come out from the outlet and carbon atoms were in the furnace.
- After 15/8min, the methane gas flow was stopped and retained the flow of hydrogen (25sccm) and nitrogen (500sccm) to initial state using gas flow controller with the temperature of furnace was decreased to 500^0C with cooling rate of 5^0 /min for 100minutes.
- After that hydrogen flow was stopped and nitrogen was continued with furnace cooling rate 10^0C/min until furnace temperature reached to 200^0C, then furnace temperature reached to room temperature naturally.
- The graphene grown Si/SiO_2 or copper sample was taken out and sample was tested with FTIR spectroscopy.

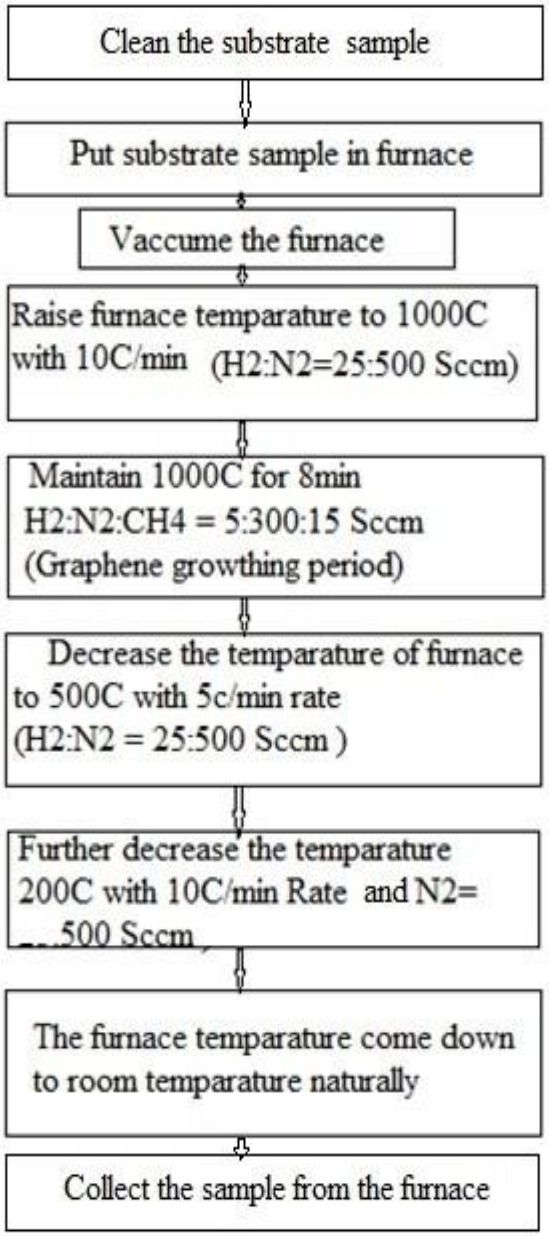

Fig 4.4: Flow for CVD grown graphene experiment.

The flow of entire work was shown in flow chart fig 4.4. If cleaning process was not done before then the annealing of copper surface can also done by hydrogen atmosphere in reactor initially with keeping reactor temperature to 1000^0C for one hour. The care should be taken during the experiment to maintain the gas flow according to timings set in the temperature control programmer.

The photograph of graphene grown samples was shown in the fig 4.5. The first experiment was done on Si/SiO_2 substrate with growth time 15min; second one again on

same substrate with growth time 8min, and last experiment on Copper substrate with growth time 8min.

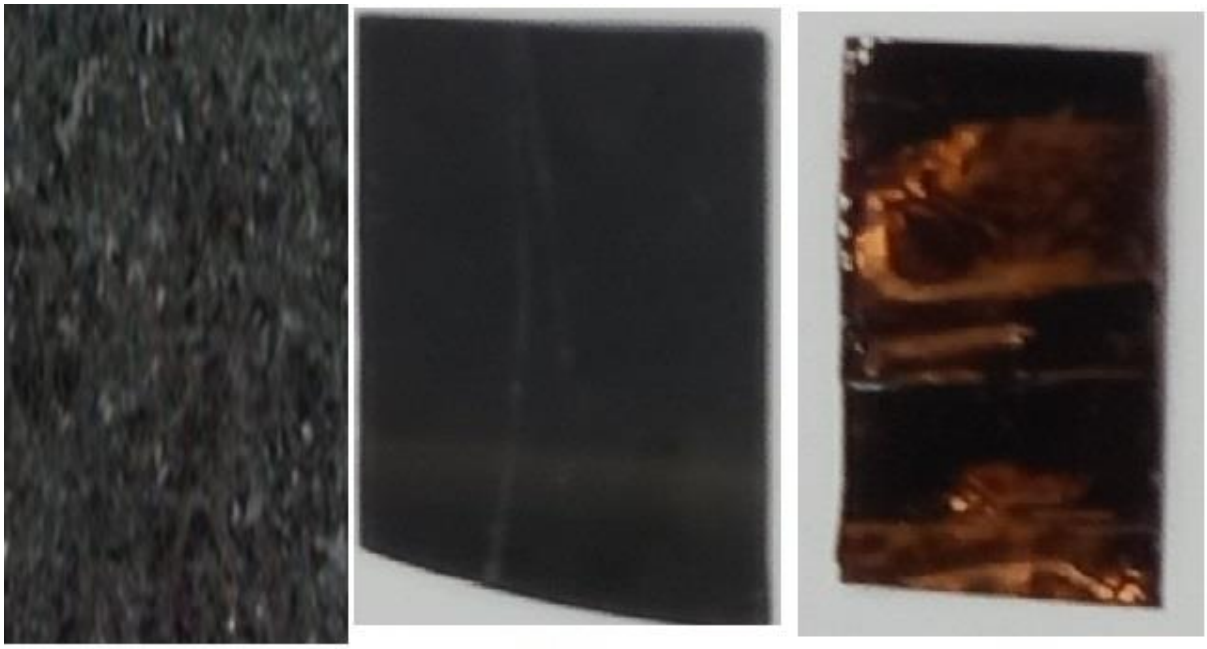

Fig 4.5: Graphene on (a) Si/SiO_2 with 15min growth time, (b) Si/SiO_2 with 8min growth time, (c) Copper with 8min growth time.

As discussed earlier the growth time play main role in number of layers deposition of graphene, as time increased number of layers also increased. The FTIR spectrum was studied for above three samples which were shown in following.

4.3 FTIR Spectrum

The versatile substance analysis method known as FTIR (Fourier Transform Infrared Spectroscopy) aids in control of quality by locating organic or inorganic (some) impurities that could lead to a malfunction. For users who required assistance detecting unidentified compounds, additives, impurities, and other material unknowns, FTIR analysis support serve as a very helpful inspection and troubleshooting tool. An established method for quality assurance when assessing industrially produced materials was FTIR spectroscopy, which was frequently used as the initial step in the material examination process. A modification in the chemical makeup of the substance or the existence of impurity was clearly shown by an alteration in the unique shape of Transmission/absorption bands. Visual inspection may reveal product flaws, and FTIR microanalysis was often used to pinpoint their source.

Smaller particles, usually 10 to 50 microns in size, as well as greater surface areas can be chemically analysed using this method.

The IRPrestige-21 model FTIR spectroscopy was shown in fig 4.6, which was available in School of Material Science and Nanotechnology Department, Jadavpur University. A Graphene grown sample was exposed to infrared light from an FTIR device that ranges in wavelength from 10,000 to 100 cm^{-1}, some of which was absorbed while a portion of which passes through.

Fig 4.6: FTIR spectroscopy.

The specimen's molecules transformed the radiation they absorb into spinning and/or resonance energy. The resulting indication, which appeared as a spectrum of wavelengths at the detector's aperture and typically ranges from 4000 cm^{-1} to 400 cm^{-1}, represented the sample's molecular spikes for absorbance. Because every molecule or chemical bonding structure of a substance will provide a distinct spectral fingerprint, spectral analysis using FTIR was a fantastic technique for identifying specific chemicals. The peaks below 1500 cm^{-1} wave number region was called finger print region. The peak data was collected from different reference papers for some bonds were show in the table 4.1.

Table 4.1: FTIR Peak occurrence data collected from different references.

Sl.No	Bond type	peak value at wave number cm^{-1}	GO/Graphene	Ref no
1	O-H Stretching	3410	GO	[164]
2	Carboxyl C=O Stretching	1721		
3	O-H Deformation	1404		
4	C-O Stretching	1087		
5	O-H stretching	3397	GO	[165]
6	CH2 stretching	2976, 2903		
7	C=O stretching	1727		
8	O-H Deformation	1392		
9	C-O stretching	1062		
10	=C-H	894		
11	C-OH stretching	1238	Reduced Graphene	
12	O-H Deformation	1392		
13	C-O stretching	1062		
14	C=C Skelton carbon ring	1579		
15	N-H stretching	3430	Graphene after polymerization	
16	C-C Absorption	1535		
17	C-N stretching	1454		
18	O-H stretching	3400	Graphene	[166]
19	C=O stretching	1730		
20	C=C Skelton stretching	1622		
21	C-O stretching	1370		
22	C-O-C of ether stretching	1058		
23	Fe-O stretching	560	Magnetic graphene composite	
24	C=C Skelton stretching	1605		
25	-OH	3432	GO	[167]
26	C=O stretching	1711		
27	C-H Stretch in methylene	2928, 2865	Graphene	
28	C-O stretching of COOH Group	1731		

29	Carboxylic Group	3412		
30	O-H stretching	3450, 1250	GO	[168]
31	C=O stretching	1730		
32	C=C Skelton stretching	1620		
33	C-O Stretch	1220, 1100		

FTIR spectra of reduced graphene with comparison to Graphene oxide was shown in fig 4.7 [164].

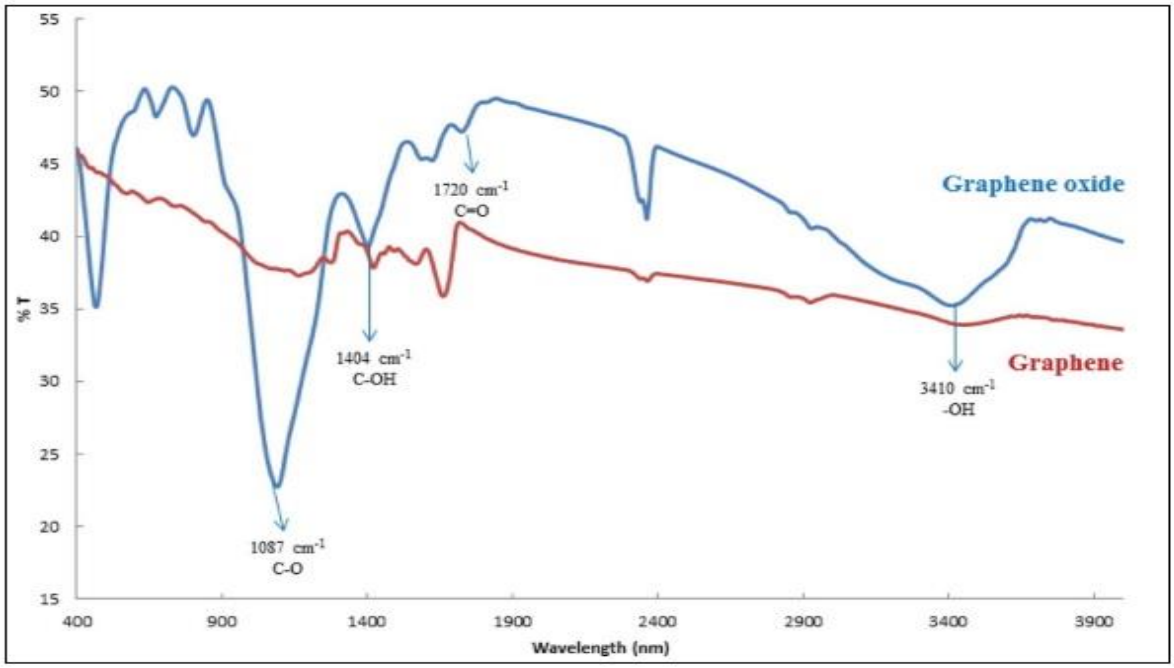

Fig 4.7: [164] Model FTIR of graphene and Graphene Oxide.

The FTIR spectra of first work, graphene grown on Si/SiO_2 Substrate for 15minutes growth time was shown in fig 4.8. The graph was drawn between wave number and absorbance, the peaks were aroused at wave numbers at strong 670 cm^{-1} denoted C=C bending, at 2350 cm^{-1} denoted O=C=O stretching and 3721 cm^{-1}, 3600 cm^{-1} denoted O-H stretching bonds. The C=C bending represented that the bond angle between two carbons has changed and some alkane class compound was there, The O=C=O stretching represented carbon dioxide compound and O=H denoted some alcohol compounds were there on the Si/SiO_2 Substrate. There was no graphene formed.

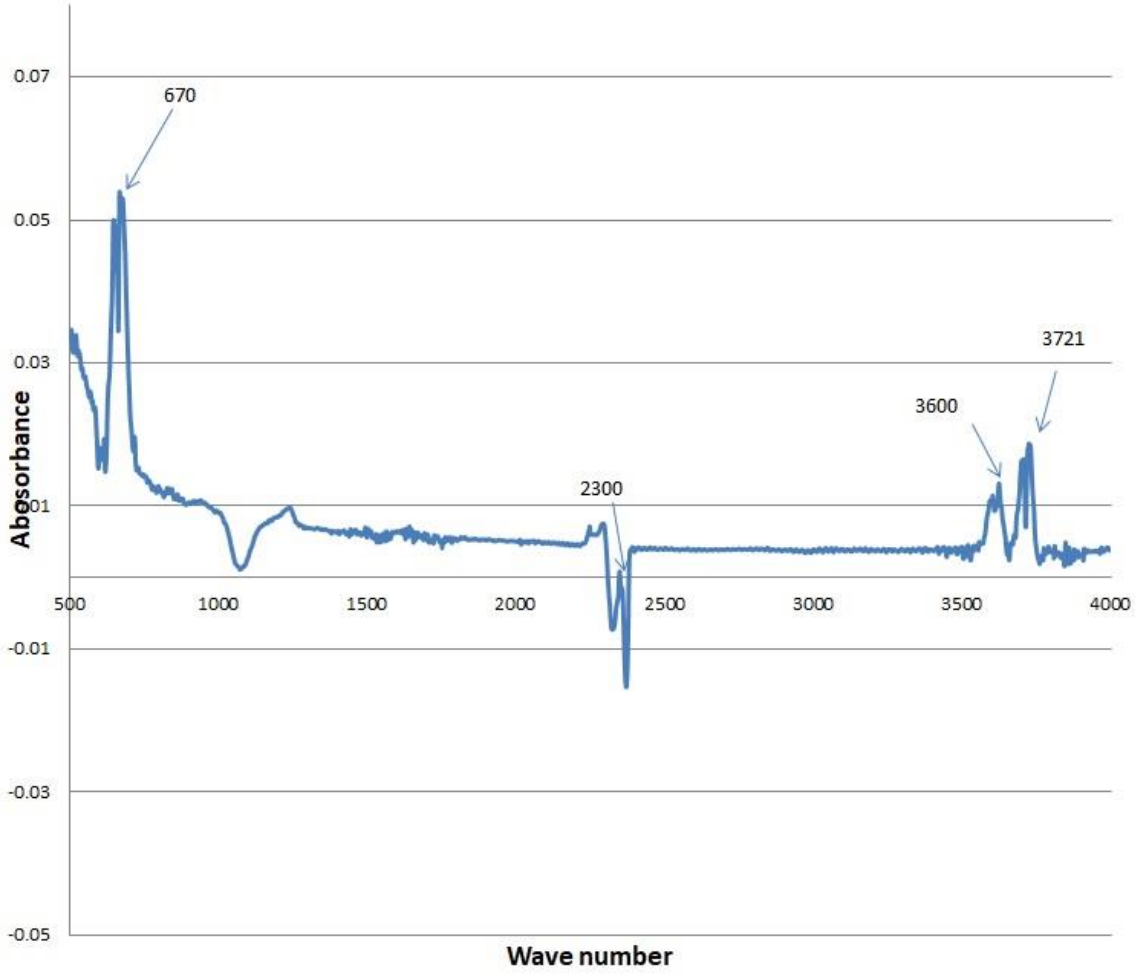

Fig 4.8: FTIR spectra of CVD grown graphene on Si/SiO_2 Substrate for 15min growth time.

The FTIR spectra of second experiment, graphene was grown on Si/SiO_2 Substrate with 8 minutes growth time was shown in fig 4.9. The peak was aroused at wave number 610 cm^{-1} denoted C-I Stretching bond or C-Br stretching bond may be there which belongs to halo compound category. There was no graphene formed.

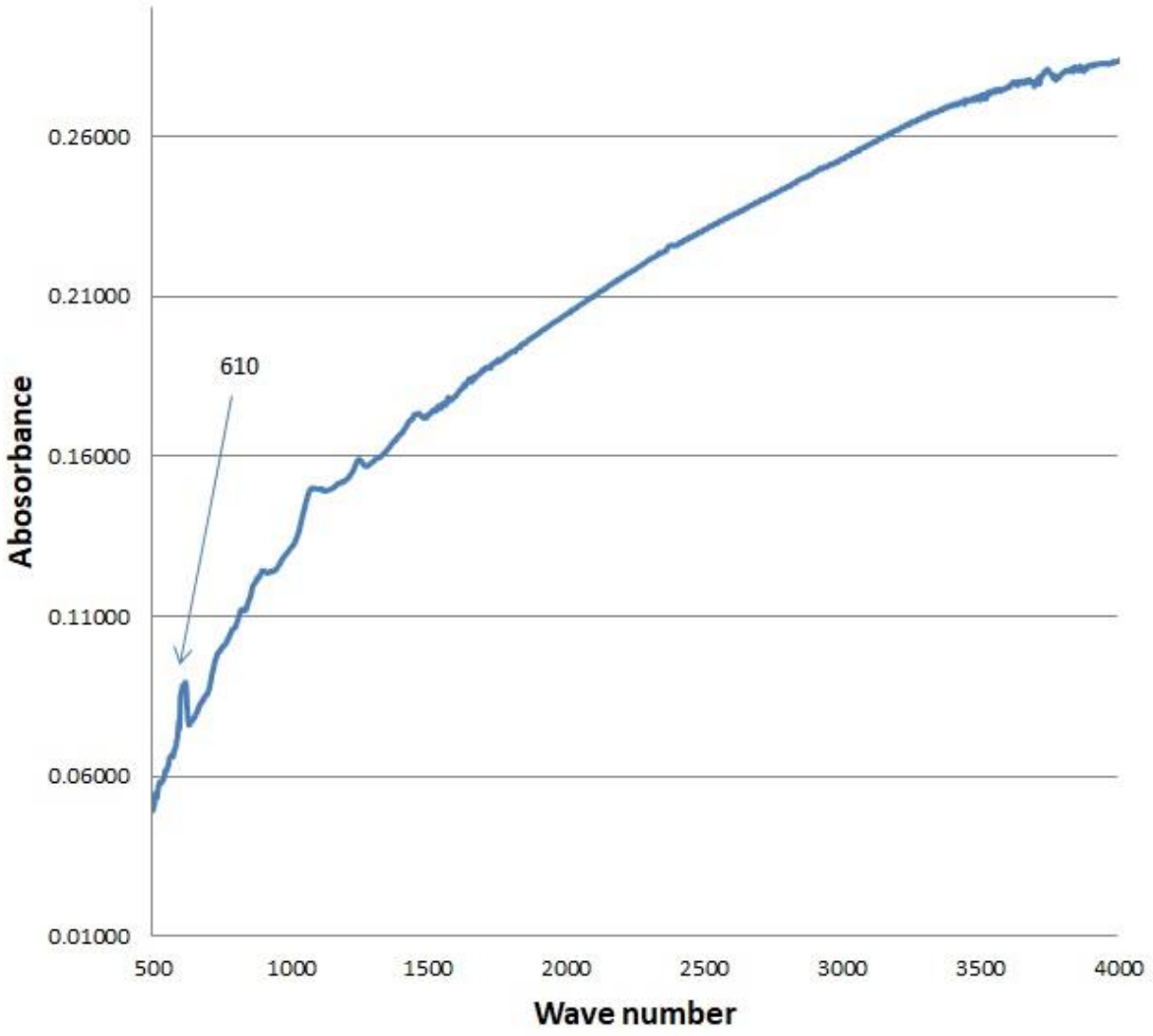

Fig 4.9: FTIR spectra of CVD grown graphene on Cu Substrate.

The FTIR spectra of third experiment, graphene grown on copper Substrate was shown in fig 4.10. The peaks were aroused at wave numbers at strong 517,579 cm^{-1} denote C-I Stretching, at 1584 cm^{-1} denotes C=C Skelton carbon ring, 1724 cm^{-1} shows that C=O stretching, 2370 cm^{-1} denotes O=C=O stretching, 3659 cm^{-1}, 3780 cm^{-1} denotes O-H stretching bonds. As discussed earlier C-I Stretching denoted halogen compound, C=C Skelton carbon ring represented cyclic alkene compounds, C=O stretching denoted unsaturated ester, O=C=O stretching denoted carbon dioxide compound and O=H denoted some alcohol compounds were there on the Cu Substrate. There was no graphene formed.

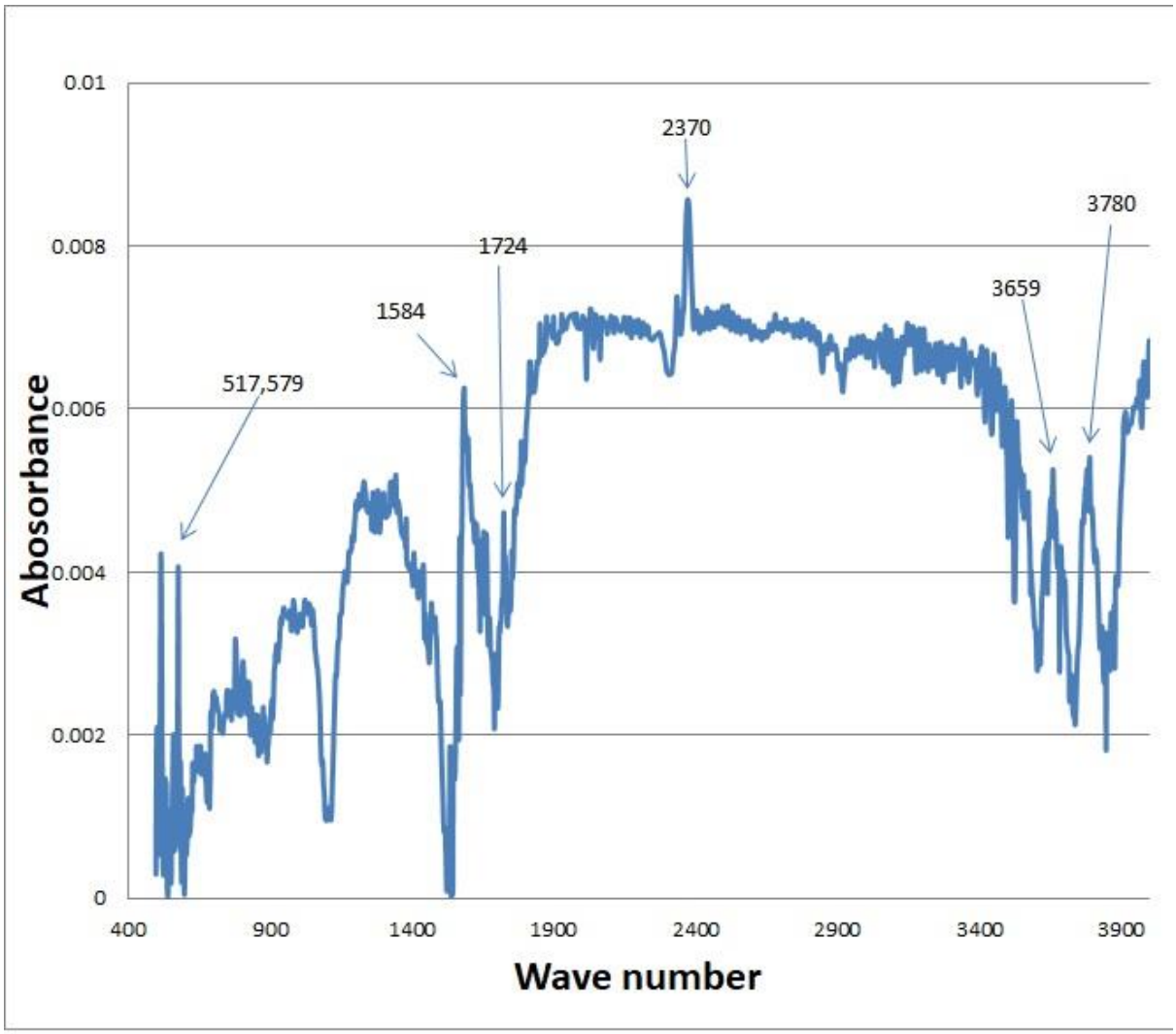

Fig 4.10: FTIR spectra of CVD grown graphene on Si/SiO_2 Substrate.

4.4. Discussions on FTIR results

This chapter discussed about growth of graphene on Si/SiO_2 and Cu with different growth times. The FTIR spectrum was analysed, for the first sample the FTIR spectra shows strong peak for C=C bond bending was found along with O=C=O stretching and O-H stretching bonds. The FTIR of second sample of graphene on Si/SiO_2 with growth time 8min shows only C-I/C-Br Stretching bond. For third sample on Cu shows strong peak of C=C Skelton bond with other peaks of C-I Stretching, C=O stretching, O=C=O stretching, O-H stretching bonds. The above all bonds represents alkane, carbon dioxide, alcohol, Cyclic alkene and ester compounds were grown on Substrates and finally concluded that graphene was not formed on any substrate.

CHAPTER -5

DESIGN AND DEVELOPMENT OF GRAPHENE BASED METASURFACE FOR X- BAND APPLICATIONS

5.1 Chapter Overview

The way of defining graphene in CST for microwave applications along with metasurface simulation was discussed in section 5.2. In section 5.3 explained fabrication process our metasurface and measurement of S_{11} and S_{12}.

5.2 Metasurface Simulation

5.2.1 Defining graphene in CST studio

As discussed earlier in the chapter 3, in microwave range, the graphene has intraband conductivity only which was given by equation 3.73 which was simplified to equation 3.75 when $E_f \gg k_B T$ condition satisfied. In our work, equation 3.73 was taken for more accuracy and given by

$$\sigma_{intra} = \frac{ie^2 k_B T}{\pi\hbar^2(\omega + i\tau^{-1})}\left[\frac{E_f}{k_B T} + 2ln\left(e^{\frac{-E_f}{k_B T}} + 1\right)\right] \quad (5.1)$$

Here, angular frequency (ω), chemical potential (E_f) and relaxation time (τ) were variable quantities. The variations in conductivity with respect to frequency in microwave region of graphene with fixed chemical potential (E_f) and relaxation time (τ) was shown in fig 5.1 using MATLAB.

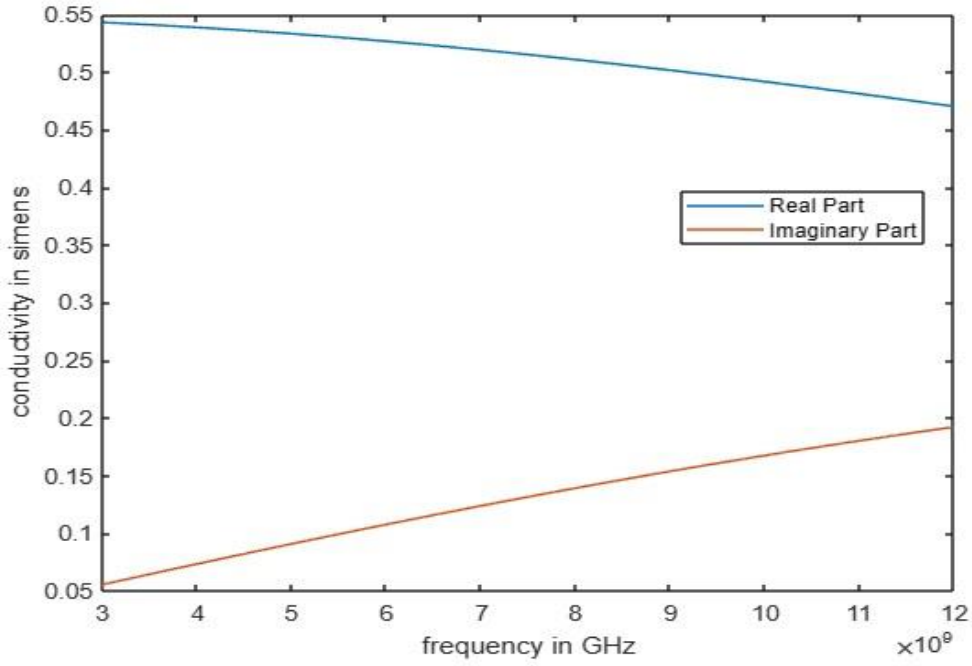

Fig 5.1: Graphene conductivity in microwave range.

The values of chemical potential (E_f) and relaxation time (τ) were given by equation 3.67 & 3.68.

$$\text{Relaxation time } \tau = \frac{\mu \mu_c}{e v_f^2} \tag{5.2}$$

$$\text{Chemical potential } E_f = \mu_c = \hbar v_f \sqrt{\left(\frac{\pi \epsilon_0 \epsilon_r V_b}{e t_s}\right)} \tag{5.3}$$

Here chemical potential was varied with bias voltage applied, and then relaxation time was varied according to chemical potentials, by varying these two parameters intraband conductivity was varied, so that graphene sheet resistance was varied accordingly. The values of parameters of conductivity, Relaxation time and Chemical potential of graphene (equation 5.1, 5.2 and 5.3 respectively) were shown in following table 5.1.

Table 5.1: Parameter values along with units which were used in formulas.

Sl.No	Symbol	Parameter	Value	Units
1	e	Charge of electron	$1.602*10^{-19}$	Coulombs
2	k_B	Boltzmann constant	$1.38*10^{-23}$	J/K
3	T	Ambient Temperature	300	Kelvin
4	τ	Relaxation time	11.88	Pico sec

5	E_f	Chemical potential	10.7	meV
6	ϵ_0	Free space Dielectric constant	$8.85*10^{-12}$	F/m
7	ϵ_r	Dielectric constant of arlon	4.3	-
8	μ	Charge carrier mobility of graphene	10,000	$cm^2\ (Vs)^{-1}$
9	v_f	Fermi velocity of fermions	$3*10^6$	m/Sec
10	V_b	Bias voltage	30	V
11	t_s	Thickness of substrate	$0.762*10^{-3}$	M
12	$\hbar$	Reduced planks constant	$1.054*10^{-34}$	J.Sec/rad

From the graph it can be observed that real and imaginary parts of graphene conductivity were almost constant in our frequency region with fixed chemical potential (E_f) and relaxation time (τ). From this constant conductivity the value of resistivity of graphene was calculated, which was used for defining the graphene ohmic sheet resistance in Computer Simulation Tool (CST 2019) as shown in fig 5.2.

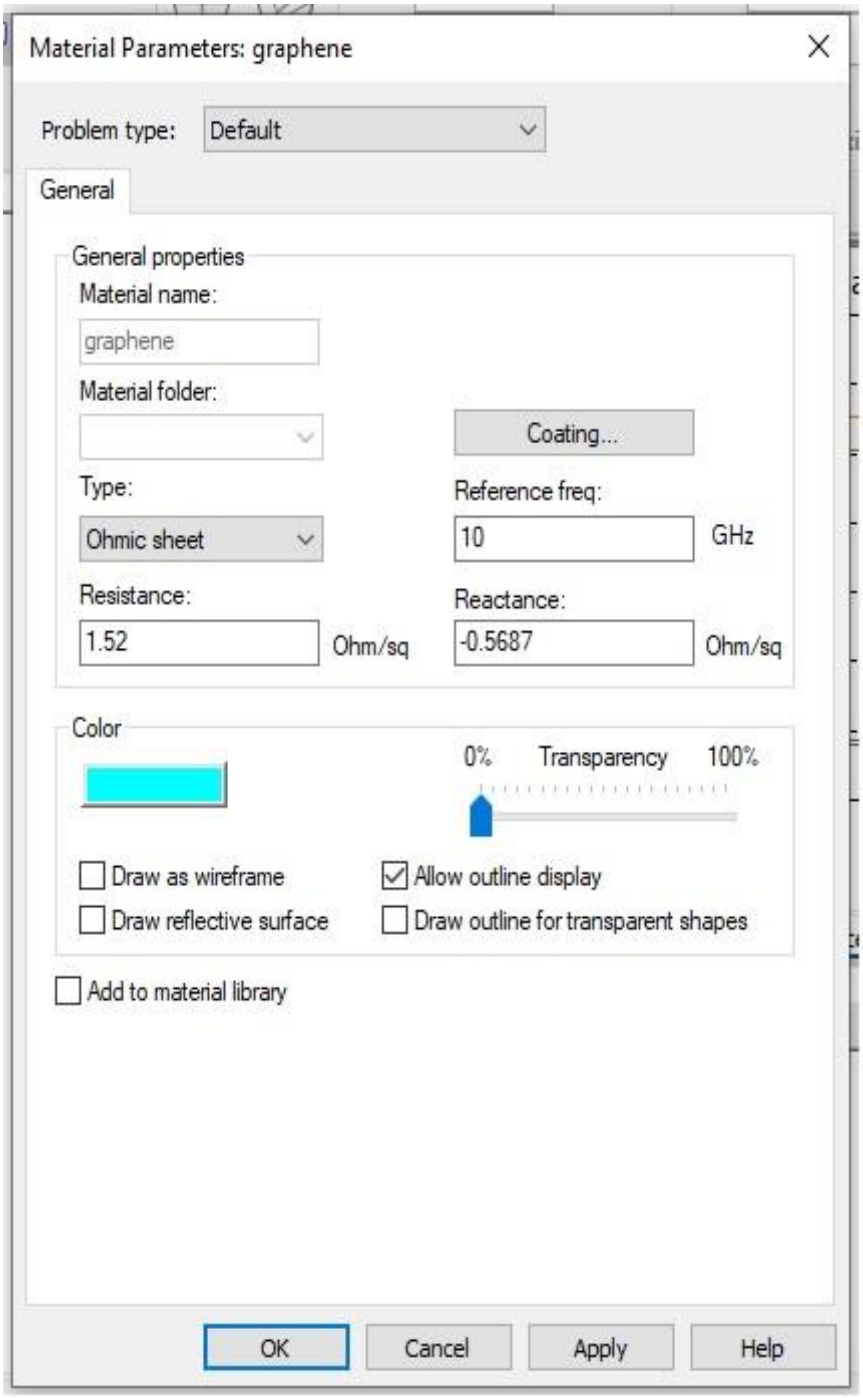

Fig 5.2: Defining graphene in CST.

5.2.2 Simulation of Metasurface

The designed metasurface unit cell with 16mm square dimensions was operated in X-band with resonance frequency 10.16GHz. The arlon AD 430 (lossy) was used as substrate material which has less thickness and thermally stable with following specifications

- Thickness: 0.762mm
- Dielectric constant: 4.3

- Permeability: 1
- Tan (δ):0.003
- Thermal conductivity: $0.46Wk^{-}1m^{-1}$

On this substrate, the metasurface unit cell was designed with graphene was used as a conducting material. The four legged Jerusalem cross shape was taken for our design and the dimensions were optimised for X-band applications. The metasurface and unit cell with optimised dimensions were shown in fig 5.3.

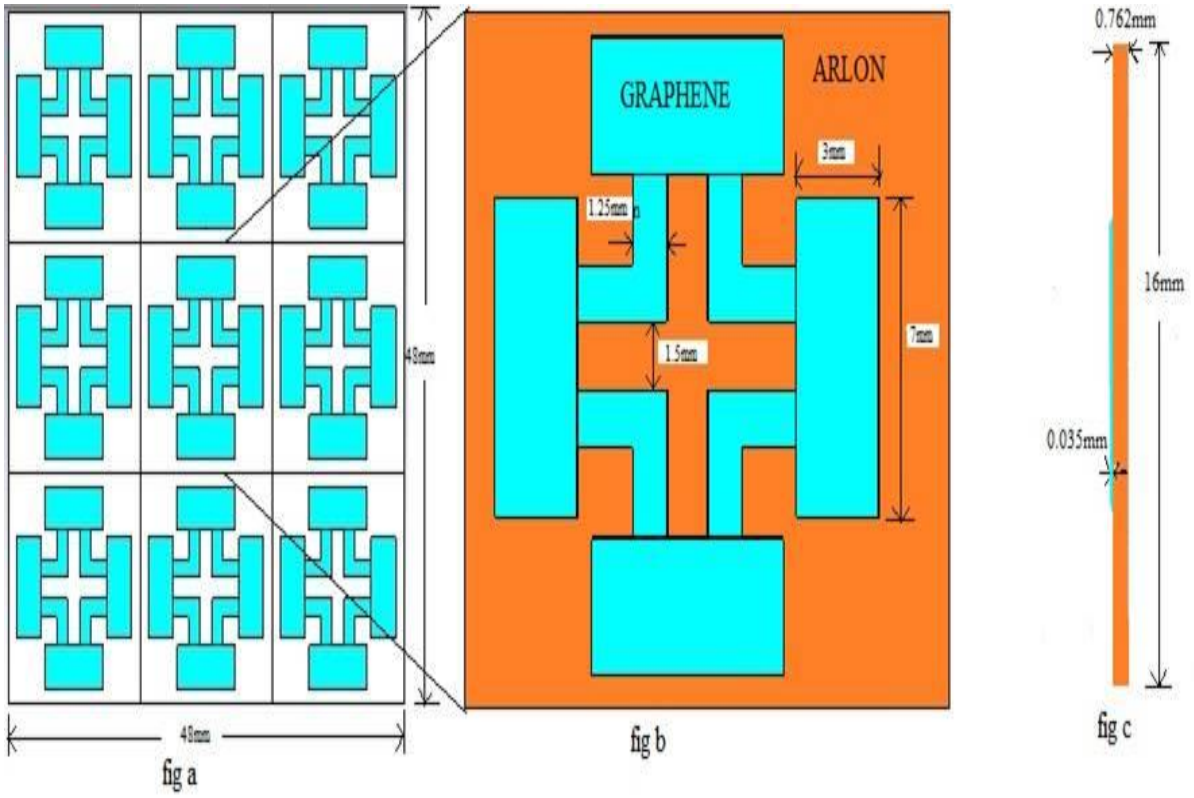

Fig 5.3: (a) Metasurface full structure, Fig (b) Unit Cell front view, Fig (c) Unit Cell side view.

The simulation of this design by using floquet port mode option in CST 2019 and got good results of S11 and S12 for different cases of input applied bias voltages which were shown in table 5.2.

Table 5.2: Graphene resistivity for different values of applied bias voltage.

S.No	Bias voltage in Volts	Relaxation time in pico sec	Chemical potential (eV)	Resistivity (ohm/sq)
1	5	4.859	0.0044	9.0643-1.3830i
2	10	6.86	0.0062	4.5567-0.9815i
3	20	9.7	0.0087	2.2957-0.7i
4	30	11.188	0.0107	1.5246-0.5687i
5	50	15.34	0.0138	0.9155-0.4410i
6	100	21.7	0.0195	0.4580-0.3121

The S_{11} and S_{12} of simulated results were shown in fig 5.4 and fig 5.5

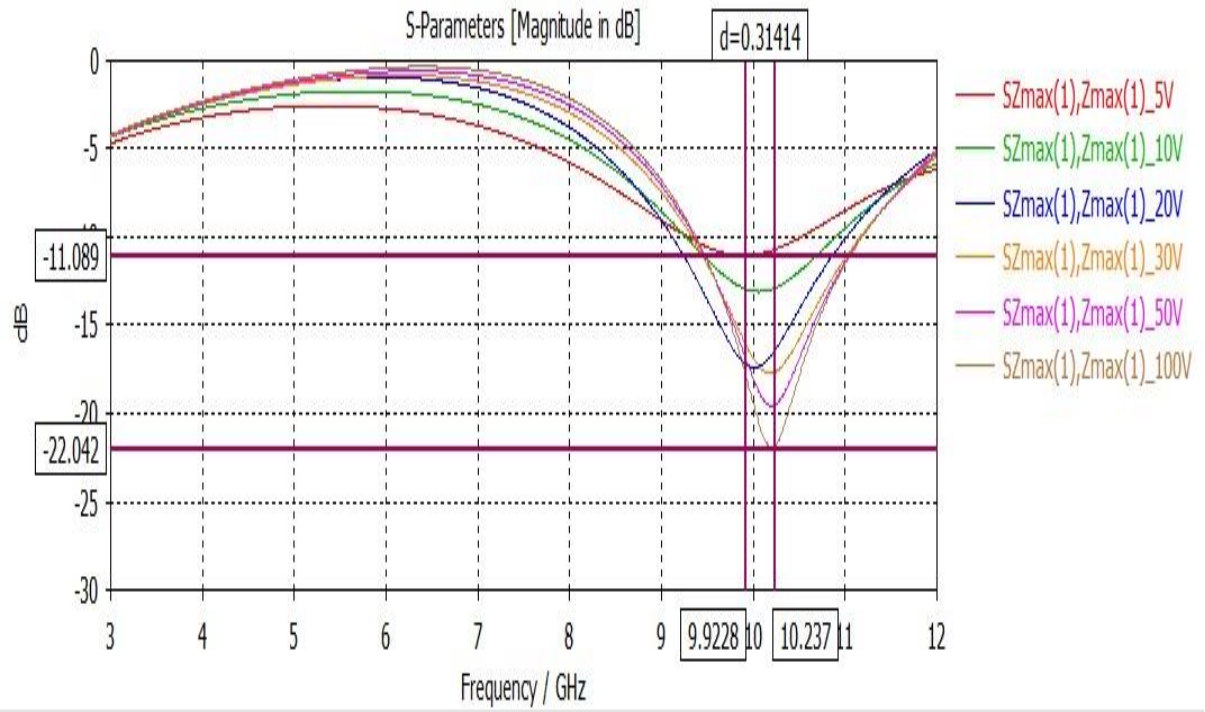

Fig 5.4: S_{11} of Simulated results of Graphene Metasurface.

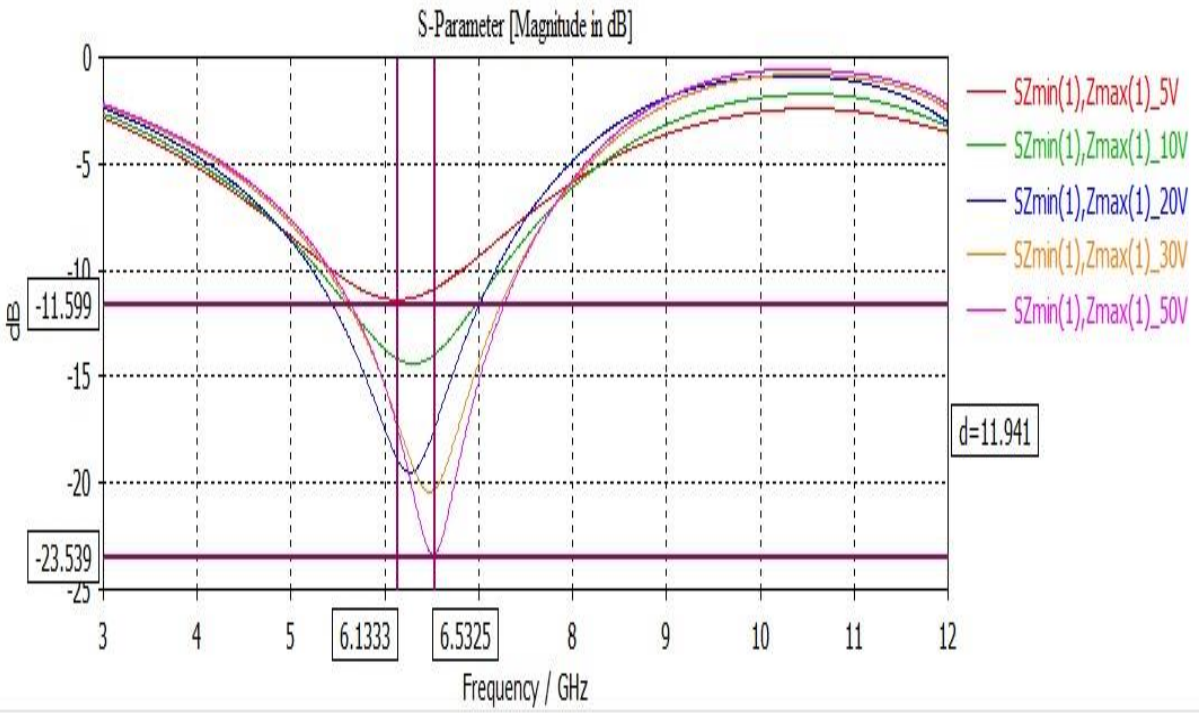

Fig 5.5: S_{12} of Simulated results of Graphene Metasurface.

5.2.3 Discussion on Simulated Results

From these results of S_{11} and S_{12} it can observe that there was a shift in frequency to high value when applied bias voltage was increased which gave frequency Reconfigurability by changing the applied voltage. There was also raise in value of S-parameters when voltage increased and S_{11} was maximum when S_{12} was minimum and S_{12} was maximum when S_{11} was minimum.

5.3 Fabrication and Measurement of Metasurface

5.3.1 Fabrication of Metasurface

- First masks were prepared using dxf file and Auto-CAD as shown in fig 5.6 for etching the copper on arlon substrate.

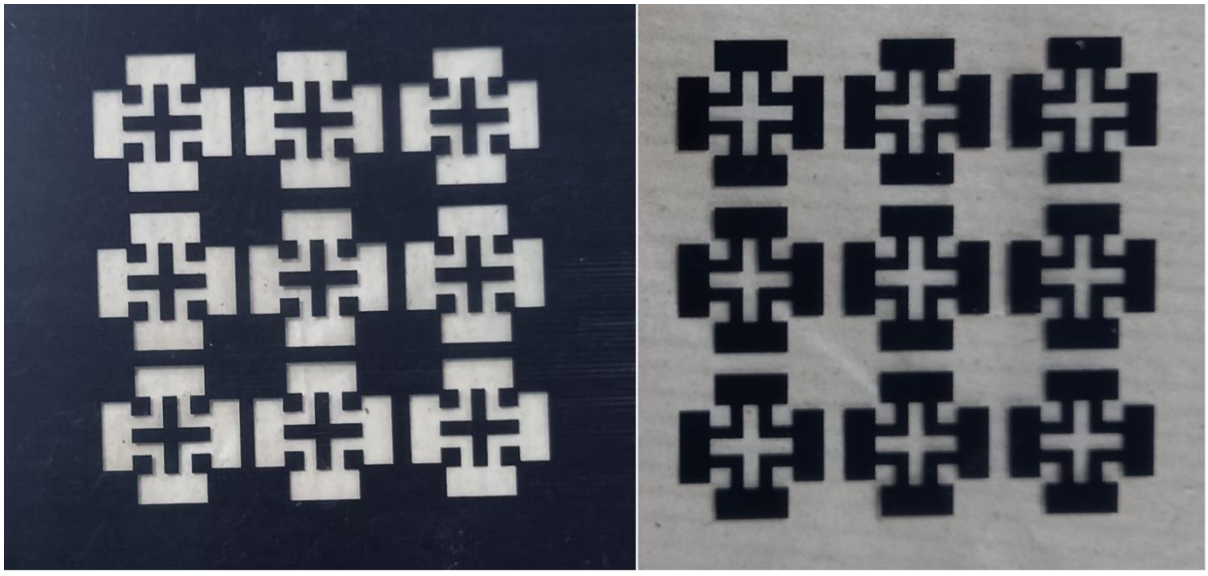

(a) (b)

Fig 5.6: (a) Mask for Graphene deposition part etching, (b) Mask for other than graphene part etching.

- Then arlon AD 430(lossy) substrate was taken and cleaned its surface with acetone which was shown in fig 5.7.

Fig 5.7: Cleaned Arlon AD430 Substrate.

- Now etched out the copper from our structured part using mask shown in fig 5.5 (a), then resultant substrate was shown in fig 5.8.

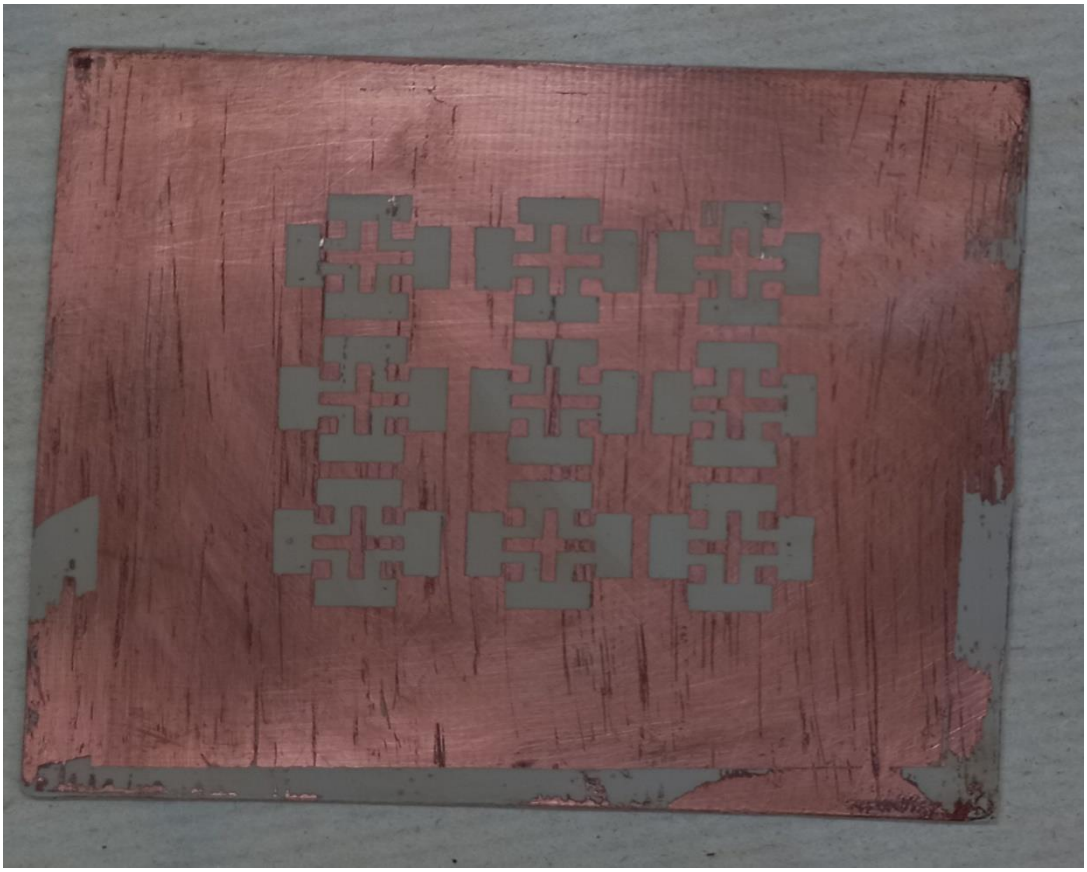

Fig 5.8: Structured part etched out Substrate.

- Now graphene ink witch was bought from Shilpent Company was deposited with 0 size brush as shown fig 5.9.

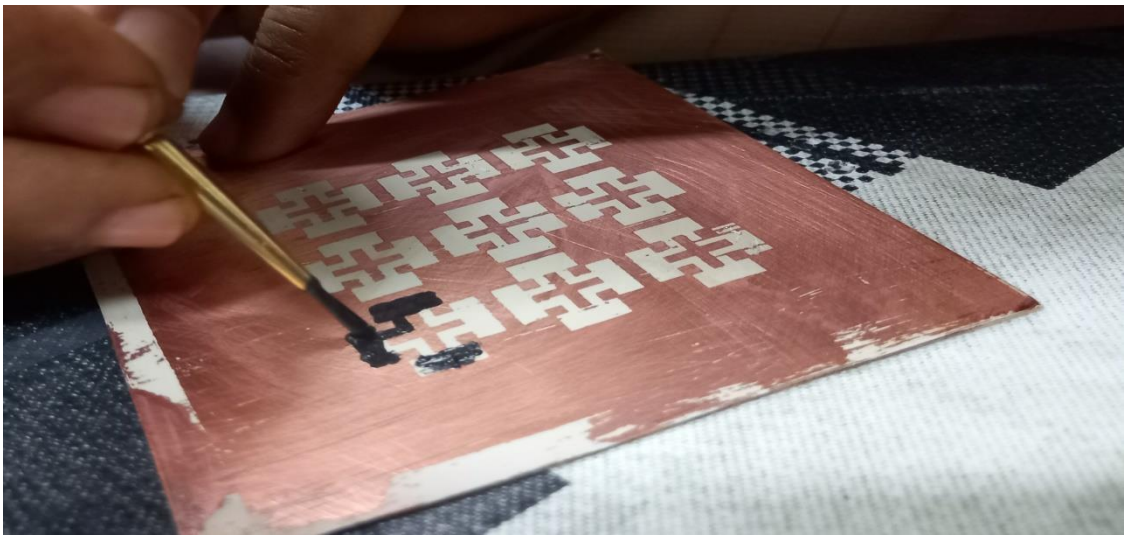

Fig 5.9: Graphene ink deposition.

- After deposition of graphene (fig 5.10), kept the deposited substrate for 30min for sticking purpose.

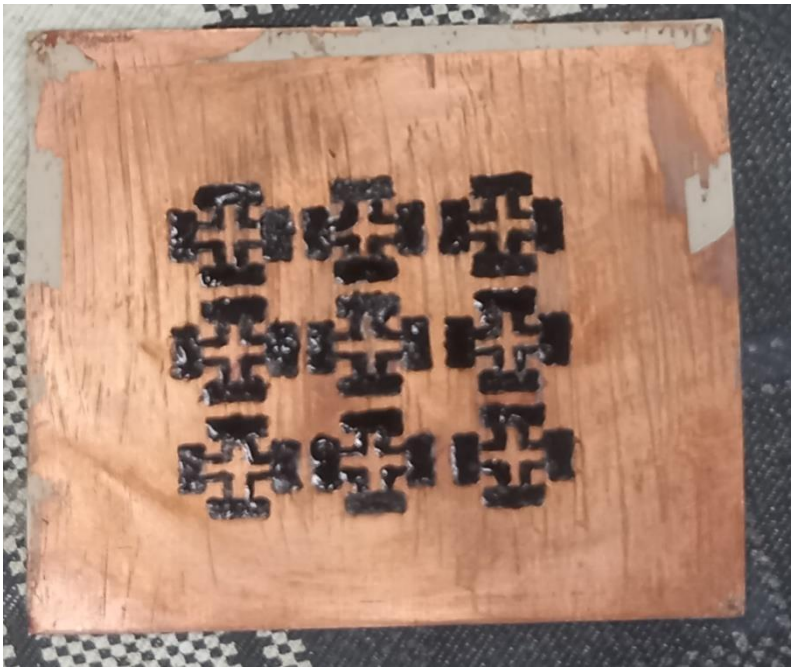

Fig 5.10: Substrate after Graphene ink deposition according to our shape.

- Then heat this structure with dryer to get strong stickiness with substrate. After that again place a mask shown in fig 5.6 (b) to remove remaining part of copper from the surface of substrate. After this step the metasurface fabrication was successfully completed as shown in fig 5.11.

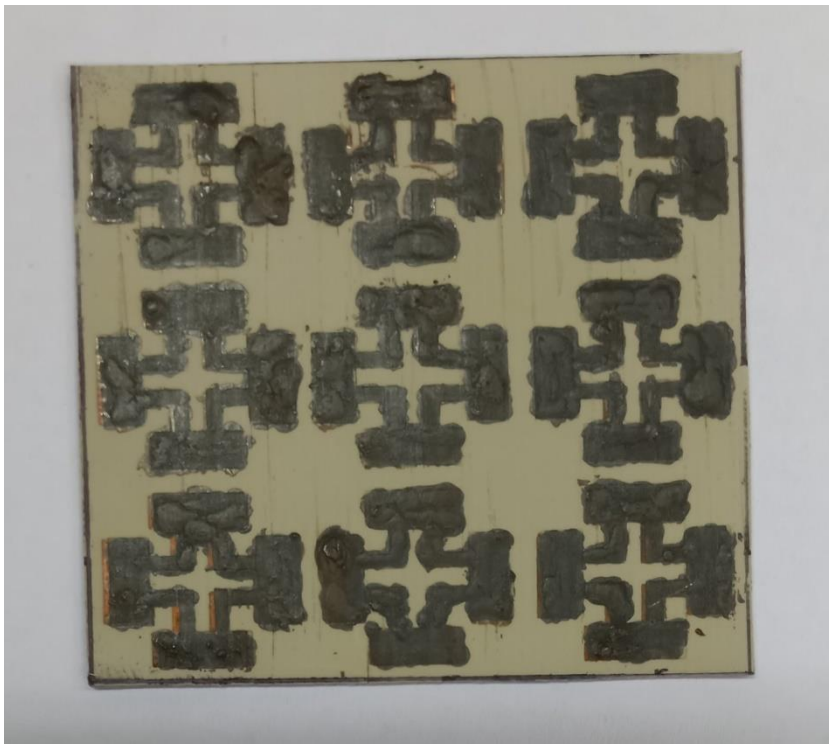

Fig 5.11: Metasurface.

5.3.2 Measurement of S_{11} and S_{12} of Metasurface

The measurement setup was done in anechoic chamber as shown in fig 5.12. The metasurface was kept in near field of horn antenna 1 as shown. The S_{11} and S_{12} were measure by vector network analyser. First took result of S_{11} and S_{12} without the metasurface and after that with metasurface with plane wave propagation. The measured S_{11} and S_{12} curves were shown in Fig 5.13 and fig 5.14.

Fig 5.12: Measurement setup of FSS.

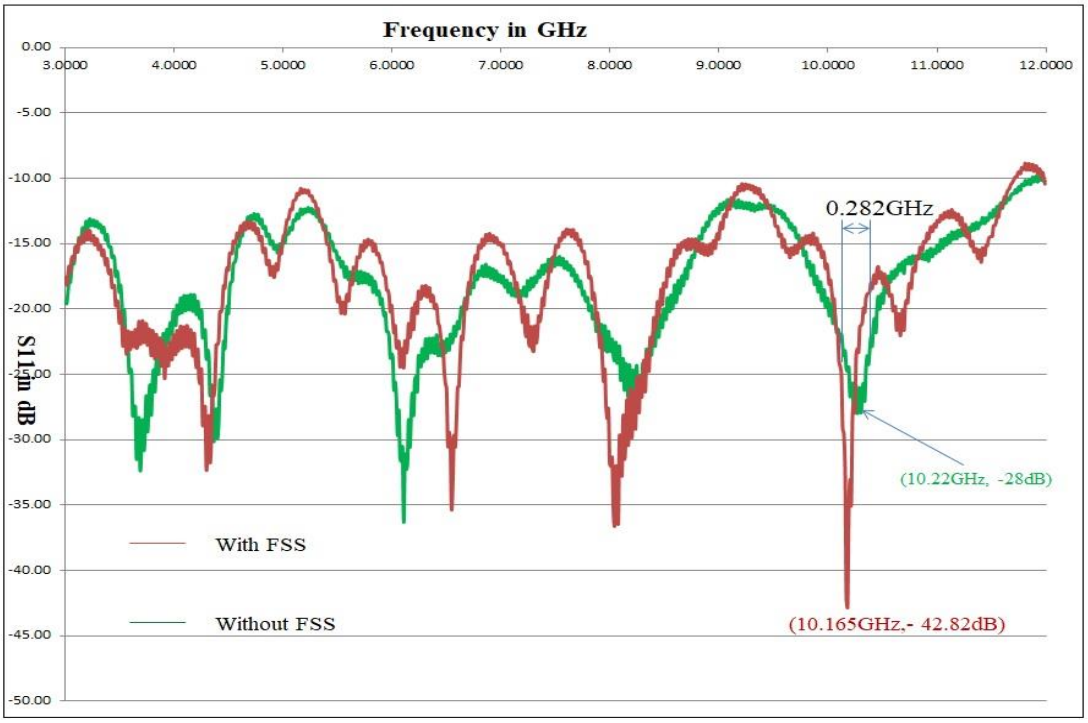

Fig 5.13: Measured S_{11} from VNA.

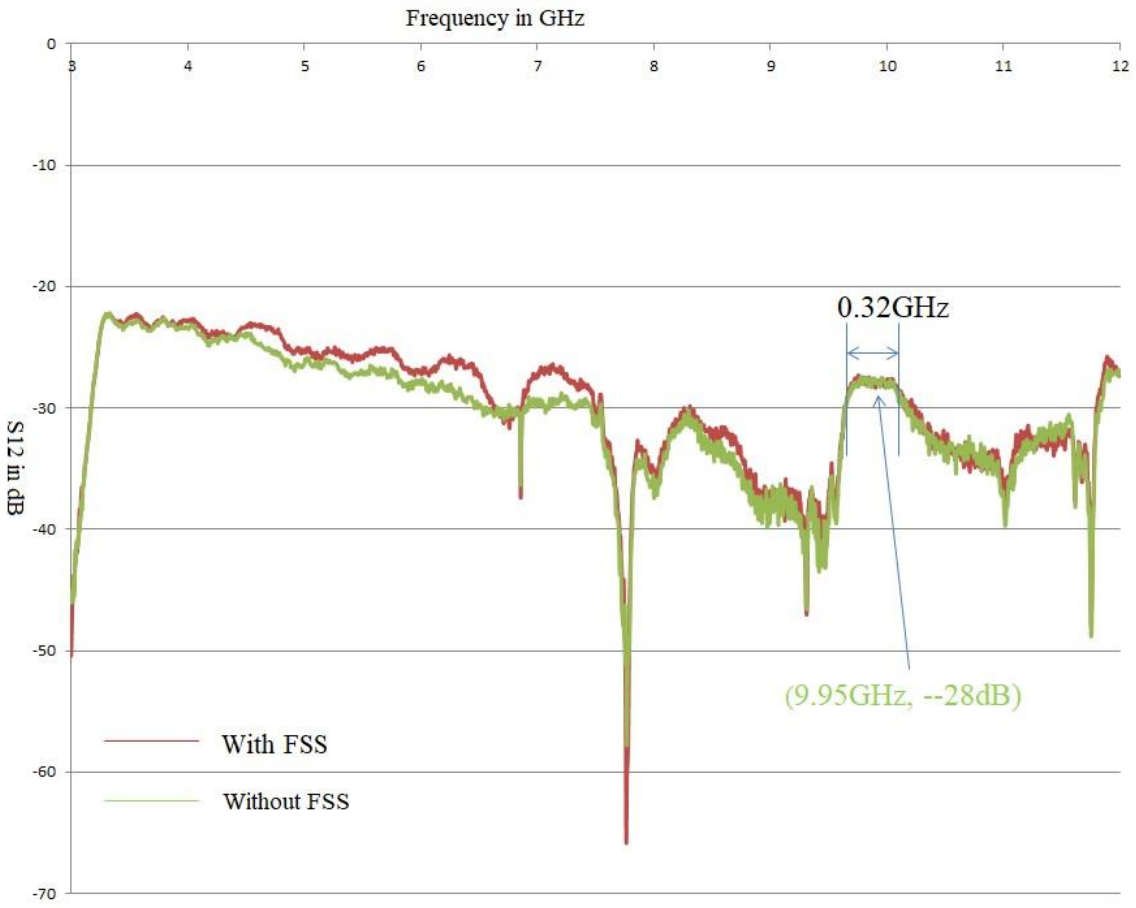

Fig 5.14: Measured S_{12} from VNA.

5.3.3 Discussion on Measured Results

From the above curves of the measured S_{11} and S_{12}, peak values of both were increased by 14dB and 8dB respectively from without metasurface to with metasurface, reflection was maximum where it was minimum transmission and transmission was maximum where it was minimum reflection.

5.4 Comparison of Simulated Results with Measurement Results of Metasurface

The compared measured results with simulated results with 30V bias voltage as shown in fig 5.15 and 5.16.

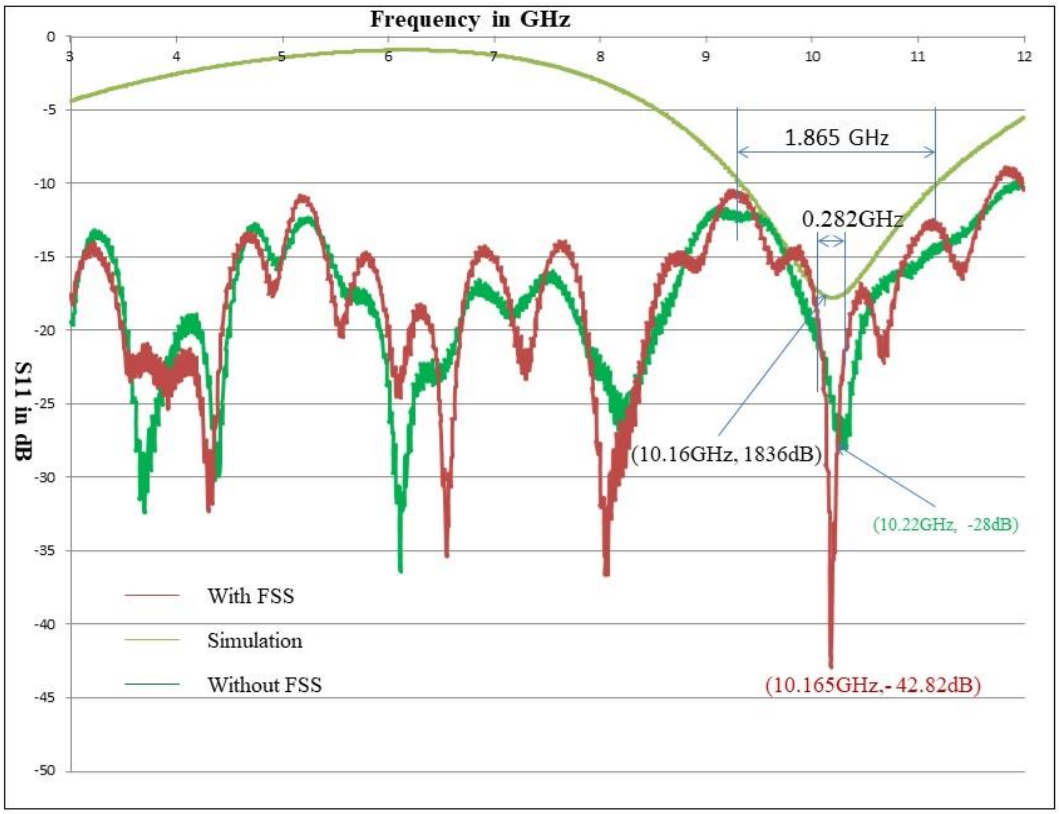

Fig 5.15: Comparison of measured results with simulated results of S_{11}.

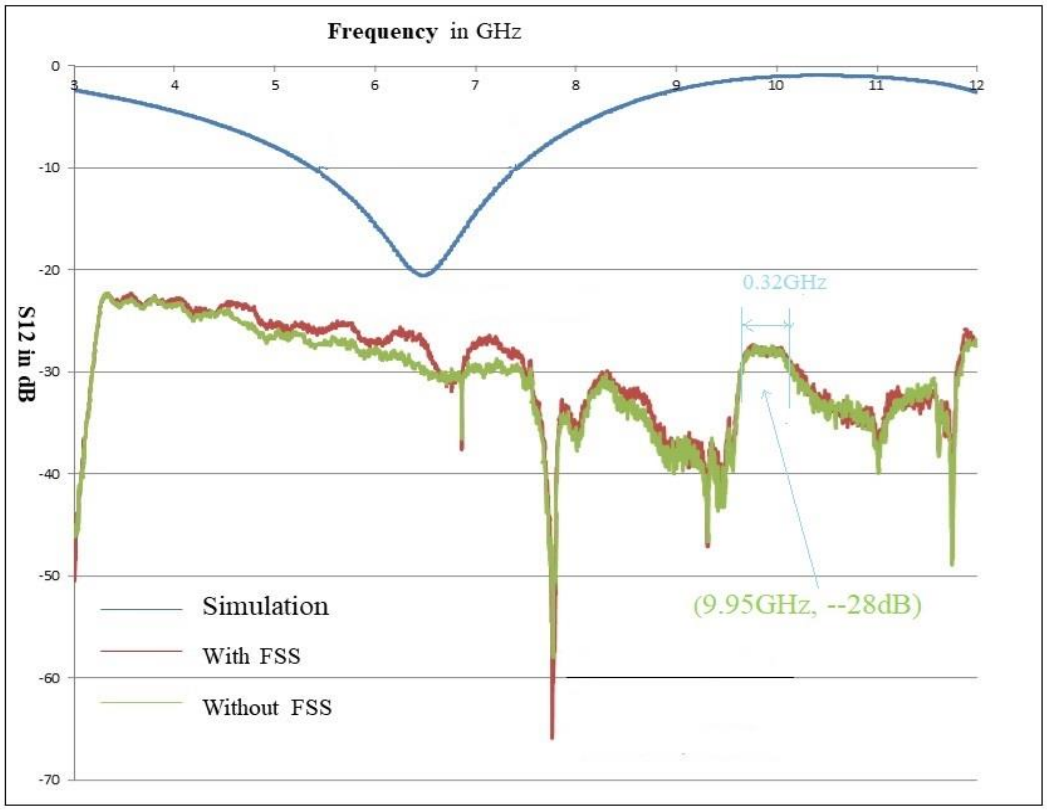

Fig 5.16: Comparison of measured results with simulated results of S_{12}.

From the above graph fig 5.15 and fig 5.16, the fabricated graphene metasurface was successfully reflected X-band frequency resonated at the same as in simulated results. But the 10dB band width was reduced significantly, S_{11} was maximum when S_{12} was minimum and S_{12} was maximum when S_{11} was minimum.

CHAPTER -6
CONCLUSION AND FUTURE WORK

6.1 Conclusions

The aim of this thesis was that designing of Graphene bases metasurface for X-band applications. For that first, the graphene production was tried lab using chemical vapour deposition method, by performing three experiments for grown of graphene on two different substrates. In the first experiment, the graphene was developed on Si/SiO_2 with growth timing 15min. in second experiment, the graphene was developed on Si/SiO_2 substrate with growth time 8min, and last experiment on Copper substrate with 8min. FTIR spectrum was analysed for these samples and found that there were different bonding components present along with C=C bonds on the samples of first and second experiments, there was no C-C bond formation on any these samples, that shows that graphene was not grown on any of the substrates. This may due to the flow of gases into the inlet of furnace was not in correct ratios.

The graphene based four legged Jerusalem shaped metasurface was designed in CST 2019 and fabricated in the lab for X-band applications. The results of reflection resonance was matched with the fabricated metasurface when measurement of reflection of metasurface with keeping metasurface in near field of horn antenna (resonant at 10.16GHz). But there was a significant bandwidth difference in both measured and simulated results. From the simulation results, the frequency Reconfigurability in both reflection and transmission band with respect to change in Fermi level of graphene was achieved.

Finally concluded that the designed metasurface can be used in X-band applications with need of reflections and C-Band applications for need of transmission and in both the cases small band of frequency Reconfigurability was achieved. The main advantages of graphene metasurface were that as the graphene was light weight, thermally, mechanically strong, stable and has excellent electrical and optical properties, so that it can used in satellite and space applications in X-band.

6.2 Future Work

This thesis was mainly focussed on the production of graphene using CVD method, design of graphene based metasurface for X-band applications with small range of frequency Reconfigurability only in simulation part. As it was Nano structured material the operating power level was also low and got less gain. By small changes in the shape of unit cell of metasurface or by introducing spurline in the structure to achieve polarisation Reconfigurability and sharp frequency cut off filter property for space applications. If defective ground structure added, the multiband frequency response will come according to defect shape of ground. By adding different layers of metal like gold or multi-layer graphene with separated by some materials to get good gain.

REFERENCES

[1] Freestone, I., Meeks, N., Sax, M., & Higgitt, C. (2007). The Lycurgus cup—a roman nanotechnology. *Gold bulletin*, *40*, 270-277.

[2] Reibold, M., Pätzke, N., Levin, A. A., Kochmann, W., Shakhverdova, I. P., Paufler, P., & Meyer, D. C. (2009). Structure of several historic blades at nanoscale. *Crystal Research and Technology: Journal of Experimental and Industrial Crystallography*, *44*(10), 1139-1146.

[3] Faraday, M. (1857). X. The Bakerian Lecture.—Experimental relations of gold (and other metals) to light. *Philosophical transactions of the Royal Society of London*, (147), 145-181.

[4] Horvath, H. (2009). Gustav Mie and the scattering and absorption of light by particles: Historic developments and basics. *Journal of Quantitative Spectroscopy and Radiative Transfer*, *110*(11), 787-799.

[5] Hulla, J. E., Sahu, S. C., & Hayes, A. W. (2015). Nanotechnology: History and future. *Human & experimental toxicology*, *34*(12), 1318-1321.

[6] Feynman, R. P. (1992). There's plenty of room at the bottom [data storage]. *Journal of microelectromechanical systems*, *1*(1), 60-66.

[7] Mota, E. G., & Subramani, K. (2012). Nanotechnology in Operative Dentistry: A Perspective Approach of History, Mechanical Behavior, and Clinical Application. In *Emerging Nanotechnologies in Dentistry* (pp. 49-69). William Andrew Publishing.

[8] Binnig, G., & Rohrer, H. (1987). Scanning tunneling microscopy—from birth to adolescence. *reviews of modern physics*, *59*(3), 615.

[9] Novoselov, Kostya S., et al. "Electric field effect in atomically thin carbon films." *science* 306.5696 (2004): 666-669.

[10] Novoselov, K. S., Jiang, D., Schedin, F., Booth, T. J., Khotkevich, V. V., Morozov, S. V., & Geim, A. K. (2005). Two-dimensional atomic crystals. *Proceedings of the National Academy of Sciences*, *102*(30), 10451-10453.

[11] Novoselov, K. S., Geim, A. K., Morozov, S. V., Jiang, D., Katsnelson, M. I., Grigorieva, I. V., ... & Firsov, A. (2005). Two-dimensional gas of massless Dirac fermions in graphene. *nature*, *438*(7065), 197-200.

[12] Schwierz, F. (2010). Graphene transistors. *Nature nanotechnology*, *5*(7), 487-496.

[13] Li, Q., Meng, H., Yu, J., Xiao, W., Zheng, Y., & Wang, J. (2014). Enhanced photocatalytic hydrogen-production performance of graphene–ZnxCd1− xS composites by using an organic S source. *Chemistry–A European Journal*, *20*(4), 1176-1185.

[14] Li, Q., Li, X., Wageh, S., Al-Ghamdi, A. A., & Yu, J. (2015). CdS/graphene nanocomposite photocatalysts. *Advanced Energy Materials*, *5*(14), 1500010.

[15] Xia, Y., Li, Q., Lv, K., Tang, D., & Li, M. (2017). Superiority of graphene over carbon analogs for enhanced photocatalytic H2-production activity of ZnIn2S4. *Applied Catalysis B: Environmental*, *206*, 344-352.

[16] Raad, S. H., & Atlasbaf, Z. (2021). Solar cell design using graphene-based hollow nano-pillars. *Scientific Reports*, *11*(1), 1-8.

[17] El-Kady, M. F., Shao, Y., & Kaner, R. B. (2016). Graphene for batteries, supercapacitors and beyond. *Nature Reviews Materials*, *1*(7), 1-14.

[18] Cohen-Tanugi, D., & Grossman, J. C. (2012). Water desalination across nanoporous graphene. *Nano letters*, *12*(7), 3602-3608.

[19] Akhavan, O., & Ghaderi, E. (2013). Graphene nanomesh promises extremely efficient in vivo photothermal therapy. *Small*, *9*(21), 3593-3601.

[20] Morales-Narváez, E., & Merkoçi, A. (2012). Graphene oxide as an optical biosensing platform. *Advanced Materials*, *24*(25), 3298-3308.

[21] Sun, X., Liu, Z., Welsher, K., Robinson, J. T., Goodwin, A., Zaric, S., & Dai, H. (2008). Nano-graphene oxide for cellular imaging and drug delivery. *Nano research*, *1*, 203-212.

[22] Zhang, H., Wu, H., Wang, J., Yang, Y., Wu, D., Zhang, Y., ... & Yang, S. (2015). Graphene oxide-BaGdF5 nanocomposites for multi-modal imaging and photothermal therapy. *Biomaterials*, *42*, 66-77.

[23] Yu, Y. H., Lin, Y. Y., Lin, C. H., Chan, C. C., & Huang, Y. C. (2014). High-performance polystyrene/graphene-based nanocomposites with excellent anti-corrosion properties. *Polymer Chemistry*, *5*(2), 535-550.

[24] Zu, H. R., Wu, B., Zhang, Y. H., Zhao, Y. T., Song, R. G., & He, D. P. (2020). Circularly polarized wearable antenna with low profile and low specific absorption rate using highly conductive graphene film. *IEEE Antennas and Wireless Propagation Letters*, *19*(12), 2354-2358.

[25] Ibanez-Labiano, I., Ergoktas, M. S., Kocabas, C., Toomey, A., Alomainy, A., & Ozden-Yenigun, E. (2020). Graphene-based soft wearable antennas. *Applied Materials Today*, *20*, 100727.

[26] Kopyt, P., Salski, B., Olszewska-Placha, M., Janczak, D., Sloma, M., Kurkus, T., ... & Gwarek, W. (2016). Graphene-based dipole antenna for a UHF RFID tag. *IEEE Transactions on Antennas and Propagation*, *64*(7), 2862-2868.

[27] Akbari, M., Khan, M. W. A., Hasani, M., Björninen, T., Sydänheimo, L., & Ukkonen, L. (2015). Fabrication and characterization of graphene antenna for low-cost and environmentally friendly RFID tags. *IEEE Antennas and Wireless Propagation Letters*, *15*, 1569-1572.

[28] Nag, A., Mitra, A., & Mukhopadhyay, S. C. (2018). Graphene and its sensor-based applications: A review. *Sensors and Actuators A: Physical*, *270*, 177-194.

[29] Wu, B., Fan, C., Feng, X., Zhao, Y. T., Ning, J., Wang, D., & Su, T. (2020). Dynamically tunable filtering attenuator based on graphene integrated microstrip resonators. *IEEE Transactions on Microwave Theory and Techniques*, *68*(12), 5270-5278.

[30] Chen, J., Wang, X., Lin, Z. C., Li, L., & Fan, C. (2022). Filtering power divider with tunable attenuation based on graphene nanoplates. *IEEE Microwave and Wireless Components Letters*, *32*(8), 960-963.

[31] Ma, L., Xu, H., Lu, Z., & Tan, J. (2022). Optically Transparent Broadband Microwave Absorber by Graphene and Metallic Rings. *ACS Applied Materials & Interfaces*, *14*(15), 17727-17738.

[32] Das, P., Deoghare, A. B., & Maity, S. R. (2020). Exploring the potential of graphene as an EMI shielding material–An overview. *Materials Today: Proceedings*, *22*, 1737-1744.

[33] Zhou, Q., Zha, S., Liu, P., Liu, C., Bian, L. A., Zhang, J., ... & Ding, L. (2018). Graphene based controllable broadband terahertz metamaterial absorber with transmission band. *Materials*, *11*(12), 2409.

[34] Deekonda, L. N., Sahu, S. K., & Panda, A. K. (2021, December). A Graphene-Based Broadband Metamaterial Absorber. In *2021 Advanced Communication Technologies and Signal Processing (ACTS)* (pp. 1-4). IEEE.

[35] Abadal, S., Hosseininejad, S. E., Cabellos-Aparicio, A., & Alarcón, E. (2017, July). Graphene-based terahertz antennas for area-constrained applications. In *2017 40th International Conference on Telecommunications and Signal Processing (TSP)* (pp. 817-820). IEEE.

[36] Abohmra, A., Jilani, F., Abbas, H., Imran, M. A., & Abbasi, Q. H. (2019, May). Terahertz antenna based on graphene for wearable applications. In *2019 IEEE MTT-S International Wireless Symposium (IWS)* (pp. 1-3). IEEE.

[37] Fakharian, M. M. (2022). A graphene-based multi-functional terahertz antenna. *Optik*, *251*, 168431.

[35] Sharma, A., & Vishwakarma, D. K. (2022, November). Circularly Polarized Diamond Shaped Graphene Plasmonic Antenna Array for Terahertz Communication. In *2022 IEEE 6th Conference on Information and Communication Technology (CICT)* (pp. 1-5). IEEE.

[39] Esfandiyari, M., Lalbakhsh, A., Jarchi, S., Ghaffari-Miab, M., Mahtaj, H. N., & Simorangkir, R. B. (2022). Tunable terahertz filter/antenna-sensor using graphene-based metamaterials. *Materials & Design*, *220*, 110855.

[40] Ram, G. C., Sambaiah, P., Yuvaraj, S., & Kartikeyan, M. V. (2022). Tunable bandstop filter using graphene in terahertz frequency band. *AEU-International Journal of Electronics and Communications*, *144*, 154047.

[41] Zhang, H., Hu, C., Yang, J., Tang, L., Huang, D., Shao, L., ... & Shi, H. (2019). Graphene-based active frequency selective surface in microwave frequency. *Journal of Applied Physics*, *125*(9), 094501.

[42] Ma, C., Xiao, B., Zhou, D., & Xiao, L. (2021). A novel tunable terahertz wave modulator based on graphene and frequency selective surface (FSS). *Optics Communications*, *478*, 126375.

[43] Yang, Y. J., Wu, B., & Zhao, Y. T. (2021). Dual-band beam steering THz antenna using active frequency selective surface based on graphene. *EPJ Applied Metamaterials*, *8*, 12.

[44] Taghvaee, H., Pitilakis, A., Tsilipakos, O., Tasolamprou, A. C., Kantartzis, N. V., Kafesaki, M., ... & Abadal, S. (2022). Multiwideband terahertz communications via tunable graphene-based metasurfaces in 6G networks: Graphene enables ultimate multiwideband THz wavefront control. *IEEE Vehicular Technology Magazine*, *17*(2), 16-25.

[45] Li, N., Mei, J., Gong, D., & Shi, Y. (2022). Broadband and tunable terahertz polarization converter based on graphene composite metasurface. *Optics Communications*, *521*, 128581.

[46] Roy, S., & Debnath, K. (2023). Electromechanically tunable graphene-based terahertz metasurface. *Optics Communications*, *534*, 129319.

[47] Geim, A. K., & Novoselov, K. S. (2007). The rise of graphene. *Nature materials*, *6*(3), 183-191

[48] Mermin, N. D. (1968). Crystalline order in two dimensions. *Physical review*, *176*(1), 250.

[49] Venables, J. A., Spiller, G. D. T., & Hanbucken, M. (1984). Nucleation and growth of thin films. *Reports on progress in physics*, *47*(4), 399.

[50] Evans, J. W., Thiel, P. A., & Bartelt, M. C. (2006). Morphological evolution during epitaxial thin film growth: Formation of 2D islands and 3D mounds. *Surface science reports*, *61*(1-2), 1-128.

[51] Ritchie, R. H. (1957). Plasma losses by fast electrons in thin films. *Physical review*, *106*(5), 874.

[52] Powell, C. J., & Swan, J. B. (1959). Origin of the characteristic electron energy losses in aluminum. *Physical Review*, *115*(4), 869.

[53] Stern, E. A., & Ferrell, R. A. (1960). Surface plasma oscillations of a degenerate electron gas. *Physical Review*, *120*(1), 130.

[54] Pendry, J. B., Martin-Moreno, L., & Garcia-Vidal, F. J. (2004). Mimicking surface plasmons with structured surfaces. *science*, *305*(5685), 847-848.

[55] Noguez, C. (2007). Surface plasmons on metal nanoparticles: the influence of shape and physical environment. *The Journal of Physical Chemistry C*, *111*(10), 3806-3819.

[56] Qin, P., Li, E. P., Yang, Y., Ma, H., Zheng, B., Gao, F., ... & Chen, H. (2018). Spoof surface plasmonic graphene for controlling the transports and emissions of electromagnetic waves. *IEEE Transactions on Microwave Theory and Techniques*, *67*(1), 50-56.

[57] Van Tuan, D., & Khanh, N. Q. (2013). Plasmon modes of double-layer graphene at finite temperature. *Physica E: Low-dimensional Systems and Nanostructures*, *54*, 267-272.

[58] Podunavac, I., Radonic, V., Bengin, V., & Jankovic, N. (2021). Microwave spoof surface plasmon polariton-based sensor for ultrasensitive detection of liquid analyte dielectric constant. *Sensors*, *21*(16), 5477.

[59] Inum, R., Rana, M. M., & Shushama, K. N. (2017). Development of graphene based tapered slot antennas for ultra-wideband applications. *Progress in Electromagnetics Research C*, *79*, 241-255.

[60] Zainud-Deen, S. H., Malhat, H. A., & Ghazi, A. M. (2018, December). High gain graphene-based magneto-electric antenna for 5G communications. In *2018 International Japan-Africa Conference on Electronics, Communications and Computations (JAC-ECC)* (pp. 21-24). IEEE.

[61] Zhang, J., Song, R., Zhao, X., Fang, R., Zhang, B., Qian, W., ... & He, D. (2020). Flexible graphene-assembled film-based antenna for wireless wearable sensor with miniaturized size and high sensitivity. *ACS omega*, *5*(22), 12937-12943.

[62] Sindhu, B., Kothuru, A., Sahatiya, P., Goel, S., & Nandi, S. (2021). Laser-induced graphene printed wearable flexible antenna-based strain sensor for wireless human motion monitoring. *IEEE Transactions on Electron Devices*, *68*(7), 3189-3194.

[63] Német, A., Alkaraki, S., Abassi, Q. H., & Jilani, S. F. (2021, December). A biodegradable textile-based graphene antenna for 5G wearable applications. In *2021 IEEE International Symposium on*

Antennas and Propagation and USNC-URSI Radio Science Meeting (APS/URSI) (pp. 1583-1584). IEEE.

[64] Pierantoni, L., Dragoman, M., & Mencarelli, D. (2013, October). Analysis of a microwave graphene-based patch antenna. In *2013 European Microwave Conference* (pp. 381-383). IEEE.

[65] Zheng, B., Wang, Z., & Li, N. (2021, May). A Small Size Microstrip Antenna Array Based on high-conductive Graphene Films for 5G applications. In *2021 International Conference on Microwave and Millimeter Wave Technology (ICMMT)* (pp. 1-3). IEEE.

[66] Wallace, P. R. (1947). The band theory of graphite. *Physical review*, *71*(9), 622.

[67] Kroto, H. W., Heath, J. R., O'Brien, S. C., Curl, R. F., & Smalley, R. E. (1985). C60: Buckminsterfullerene. *nature*, *318*(6042), 162-163.

[68] Andreoni, W. (Ed.). (2000). *The physics of fullerene-based and fullerene-related materials* (Vol. 23). Springer Science & Business Media.

[69] Charlier, J. C., Blase, X., & Roche, S. (2007). Electronic and transport properties of nanotubes. *Reviews of modern physics*, *79*(2), 677.

[70] Chang, S. L., Wu, B. R., Yang, P. H., & Lin, M. F. (2016). Geometric, magnetic and electronic properties of folded graphene nanoribbons. *RSC advances*, *6*(69), 64852-64860.

[71] Son, Y. W., Cohen, M. L., & Louie, S. G. (2006). Half-metallic graphene nanoribbons. *Nature*, *444*(7117), 347-349.

[72] Pykal, M., Jurečka, P., Karlický, F., & Otyepka, M. (2016). Modelling of graphene functionalization. *Physical Chemistry Chemical Physics*, *18*(9), 6351-6372.

[73] Pop, E., Varshney, V., & Roy, A. K. (2012). Thermal properties of graphene: Fundamentals and applications. *MRS bulletin*, *37*(12), 1273-1281.

[74] Balandin, A. A., Ghosh, S., Bao, W., Calizo, I., Teweldebrhan, D., Miao, F., & Lau, C. N. (2008). Superior thermal conductivity of single-layer graphene. *Nano letters*, *8*(3), 902-907.

[75] Frank, I. W., Tanenbaum, D. M., van der Zande, A. M., & McEuen, P. L. (2007). Mechanical properties of suspended graphene sheets. *Journal of Vacuum Science & Technology B: Microelectronics and Nanometer Structures Processing, Measurement, and Phenomena*, *25*(6), 2558-2561.

[76] Lee, C., Wei, X., Kysar, J. W., & Hone, J. (2008). Measurement of the elastic properties and intrinsic strength of monolayer graphene. *science*, *321*(5887), 385-388.

[77] Meyer, J. C., Kisielowski, C., Erni, R., Rossell, M. D., Crommie, M. F., & Zettl, A. (2008). Direct imaging of lattice atoms and topological defects in graphene membranes. *Nano letters*, *8*(11), 3582-3586.

[78] Sze, S. M., Li, Y., & Ng, K. K. (2021). *Physics of semiconductor devices*. John wiley & sons.

[79] Bolotin, K. I., Sikes, K. J., Jiang, Z., Klima, M., Fudenberg, G., Hone, J., ... & Stormer, H. L. (2008). Ultrahigh electron mobility in suspended graphene. *Solid state communications*, *146*(9-10), 351-355.

[80] Du, X., Skachko, I., Barker, A., & Andrei, E. Y. (2008). Approaching ballistic transport in suspended graphene. *Nature nanotechnology*, *3*(8), 491-495.

[81] Castro, E. V., Ochoa, H., Katsnelson, M. I., Gorbachev, R. V., Elias, D. C., Novoselov, K. S., ... & Guinea, F. (2010). Limits on charge carrier mobility in suspended graphene due to flexural phonons. *Physical review letters*, *105*(26), 266601.

[82] Farmer, D. B., Chiu, H. Y., Lin, Y. M., Jenkins, K. A., Xia, F., & Avouris, P. (2009). Utilization of a buffered dielectric to achieve high field-effect carrier mobility in graphene transistors. *Nano letters*, *9*(12), 4474-4478.

[83] Emani, N. K., Kildishev, A. V., Shalaev, V. M., & Boltasseva, A. (2015). Graphene: a dynamic platform for electrical control of plasmonic resonance. *Nanophotonics*, *4*(2), 214-223.

[84] Zomer, P. J., Dash, S. P., Tombros, N., & Van Wees, B. J. (2011). A transfer technique for high mobility graphene devices on commercially available hexagonal boron nitride. *Applied Physics Letters*, *99*(23), 232104.

[85] Ponomarenko, L. A., Yang, R., Mohiuddin, T. M., Katsnelson, M. I., Novoselov, K. S., Morozov, S. V., ... & Geim, A. K. (2009). Effect of a high-κ environment on charge carrier mobility in graphene. *Physical review letters*, *102*(20), 206603.

[86] Chen, J. H., Jang, C., Xiao, S., Ishigami, M., & Fuhrer, M. S. (2008). Intrinsic and extrinsic performance limits of graphene devices on SiO2. *Nature nanotechnology*, *3*(4), 206-209.

[87] Sounas, D. L., & Caloz, C. (2012). Gyrotropy and nonreciprocity of graphene for microwave applications. *IEEE transactions on microwave theory and techniques*, *60*(4), 901-914.

[88] Tamagnone, M., Gomez-Diaz, J. S., Mosig, J. R., & Perruisseau-Carrier, J. (2012). Reconfigurable terahertz plasmonic antenna concept using a graphene stack. *Applied Physics Letters*, *101*(21), 214102.

[89] Lin, I. T., Lai, Y. P., Wu, K. H., & Liu, J. M. (2014). Terahertz optoelectronic property of graphene: substrate-induced effects on plasmonic characteristics. *Applied Sciences*, *4*(1), 28-41.

[90] Llatser, I., Kremers, C., Cabellos-Aparicio, A., Jornet, J. M., Alarcón, E., & Chigrin, D. N. (2012). Graphene-based nano-patch antenna for terahertz radiation. *Photonics and Nanostructures-Fundamentals and Applications*, *10*(4), 353-358.

[91] Horng, J., Chen, C. F., Geng, B., Girit, C., Zhang, Y., Hao, Z., ... & Wang, F. (2011). Drude conductivity of Dirac fermions in graphene. *Physical Review B*, *83*(16), 165113.

[92] Esquius-Morote, M., Gómez-Dı, J. S., & Perruisseau-Carrier, J. (2014). Sinusoidally modulated graphene leaky-wave antenna for electronic beamscanning at THz. *IEEE Transactions on Terahertz Science and Technology*, *4*(1), 116-122.

[93] Llatser Martí, I., Kremers, C., Chigrin, D. N., Jornet Montaña, J. M., Lemme, M. C., Cabellos Aparicio, A., & Alarcón Cot, E. J. (2012). Radiation characteristics of tunable graphennas in the terahertz band. *Radioengineering*, *21*(4), 1-8.

[94] Balandin, A. A. (2017). Thermal Properties of Graphene, Carbon Nanotubes and Nanostructured Carbon Materials. *University of California*.

[95] Elias, D. C., Gorbachev, R. V., Mayorov, A. S., Morozov, S. V., Zhukov, A. A., Blake, P., ... & Geim, A. K. (2011). Dirac cones reshaped by interaction effects in suspended graphene. *Nature Physics*, *7*(9), 701-704.

[96] Hanson, G. W. (2008). Dyadic Green's functions and guided surface waves for a surface conductivity model of graphene. *Journal of Applied Physics*, *103*(6), 064302.

[97] Gómez-Díaz, J. S., Esquius-Morote, M., & Perruisseau-Carrier, J. (2013). Plane wave excitation-detection of non-resonant plasmons along finite-width graphene strips. *Optics express*, *21*(21), 24856-24872.

[98] Maier, S. A. (2007). *Plasmonics: fundamentals and applications* (Vol. 1, p. 245). New York: springer.

[99] Jabbarzadeh, F., Heydari, M., & Habibzadeh-Sharif, A. (2019). A comparative analysis of the accuracy of Kubo formulations for graphene plasmonics. *Materials Research Express*, *6*(8), 086209.

[100] Lima, J. R. (2015). Controlling the energy gap of graphene by Fermi velocity engineering. *Physics Letters A*, *379*(3), 179-182.

[101] Hanson, G. W. (2008). Quasi-transverse electromagnetic modes supported by a graphene parallel-plate waveguide. *Journal of Applied Physics*, *104*(8), 084314.

[102] Stauber, T., Peres, N. M. R., & Geim, A. K. (2008). Optical conductivity of graphene in the visible region of the spectrum. *Physical Review B*, *78*(8), 085432.

[103] Horng, J., Chen, C. F., Geng, B., Girit, C., Zhang, Y., Hao, Z., ... & Wang, F. (2011). Drude conductivity of Dirac fermions in graphene. *Physical Review B*, *83*(16), 165113.

[104] Edwards, R. S., & Coleman, K. S. (2013). Graphene synthesis: relationship to applications. *Nanoscale*, *5*(1), 38-51.

[105] Tour, J. M. (2014). Top-down versus bottom-up fabrication of graphene-based electronics. *Chemistry of Materials*, *26*(1), 163-171.

[106] Yi, M., & Shen, Z. (2015). A review on mechanical exfoliation for the scalable production of graphene. *Journal of Materials Chemistry A*, *3*(22), 11700-11715.

[107] Su, C. Y., Lu, A. Y., Xu, Y., Chen, F. R., Khlobystov, A. N., & Li, L. J. (2011). High-quality thin graphene films from fast electrochemical exfoliation. *ACS nano*, *5*(3), 2332-2339.

[108] Paton, K. R., Varrla, E., Backes, C., Smith, R. J., Khan, U., O'Neill, A., ... & Coleman, J. N. (2014). Scalable production of large quantities of defect-free few-layer graphene by shear exfoliation in liquids. *Nature materials*, *13*(6), 624-630.

[109] Lee, J. H., Shin, D. W., Makotchenko, V. G., Nazarov, A. S., Fedorov, V. E., Kim, Y. H., ... & Yoo, J. B. (2009). One-step exfoliation synthesis of easily soluble graphite and transparent conducting graphene sheets. *Advanced Materials*, *21*(43), 4383-4387.

[110] Van Noorden, R. (2012). Production: Beyond sticky tape. *Nature*, *483*(7389), S32-S33.

[111] Prakash, G., Capano, M. A., Bolen, M. L., Zemlyanov, D., & Reifenberger, R. G. (2010). AFM study of ridges in few-layer epitaxial graphene grown on the carbon-face of 4H–SiC (0001¯). *Carbon*, *48*(9), 2383-2393.

[112] Mbayachi, V. B., Ndayiragije, E., Sammani, T., Taj, S., & Mbuta, E. R. (2021). Graphene synthesis, characterization and its applications: A review. *Results in Chemistry*, *3*, 100163.

[113] Chen, L., Yu, H., Zhong, J., Song, L., Wu, J., & Su, W. (2017). Graphene field emitters: A review of fabrication, characterization and properties. *Materials Science and Engineering: B*, *220*, 44-58.

[114] Li, X., Cai, W., Jung, I. H., An, J. H., Yang, D., Velamakanni, A., ... & Ruoff, R. S. (2009, May). Synthesis, Characterization, and Properties of Large-area Few-layer Graphene Films with Tunable Thickness. In *ECS Meeting Abstracts* (No. 38, p. 1295). IOP Publishing.

[115] Xu, C., Wang, X., & Zhu, J. (2008). Graphene− metal particle nanocomposites. *The Journal of Physical Chemistry C*, *112*(50), 19841-19845.

[116] Yin, P. T., Shah, S., Chhowalla, M., & Lee, K. B. (2015). Design, synthesis, and characterization of graphene–nanoparticle hybrid materials for bioapplications. *Chemical reviews*, *115*(7), 2483-2531.

[117] Vandenabeele, P. (2013). *Practical Raman spectroscopy: an introduction*. John Wiley & Sons.

[118] Graves, P. R. G. D. J., & Gardiner, D. (1989). Practical raman spectroscopy. *Springer*, *10*, 978-3.

[119] Eklund, P. C., Holden, J. M., & Jishi, R. A. (1995). Vibrational modes of carbon nanotubes; spectroscopy and theory. *Carbon*, *33*(7), 959-972.

[120] Wang, Y. Y., Ni, Z. H., Yu, T., Shen, Z. X., Wang, H. M., Wu, Y. H., ... & Shen Wee, A. T. (2008). Raman studies of monolayer graphene: the substrate effect. *The Journal of Physical Chemistry C*, *112*(29), 10637-10640.

[121] Ferrari, A. C., & Robertson, J. (2000). Interpretation of Raman spectra of disordered and amorphous carbon. *Physical review B*, *61*(20), 14095.

[122] Dresselhaus, M. S., & Eklund, P. C. (2000). Phonons in carbon nanotubes. *Advances in physics*, *49*(6), 705-814.

[123] Le, H. D., Ngo, T. T. T., Le, D. Q., Nguyen, X. N., & Phan, N. M. (2013). Synthesis of multi-layer graphene films on copper tape by atmospheric pressure chemical vapor deposition method. *Advances in Natural Sciences: Nanoscience and Nanotechnology*, *4*(3), 035012.

[124] Seekaew, Y., Lokavee, S., Phokharatkul, D., Wisitsoraat, A., Kerdcharoen, T., & Wongchoosuk, C. (2014). Low-cost and flexible printed graphene–PEDOT: PSS gas sensor for ammonia detection. *Organic Electronics*, *15*(11), 2971-2981.

[125] Zhang, H. B., Zheng, W. G., Yan, Q., Yang, Y., Wang, J. W., Lu, Z. H., ... & Yu, Z. Z. (2010). Electrically conductive polyethylene terephthalate/graphene nanocomposites prepared by melt compounding. *polymer*, *51*(5), 1191-1196.

[126] Sun, Z., Yan, Z., Yao, J., Beitler, E., Zhu, Y., & Tour, J. M. (2010). Growth of graphene from solid carbon sources. *Nature*, *468*(7323), 549-552.

[127] Pendry, J. B., Holden, A. J., Robbins, D. J., & Stewart, W. J. (1998). Low frequency plasmons in thin-wire structures. *Journal of Physics: Condensed Matter*, *10*(22), 4785.

[128] Pendry, J. B., Holden, A. J., Robbins, D. J., & Stewart, W. J. (1999). Magnetism from conductors and enhanced nonlinear phenomena. *IEEE transactions on microwave theory and techniques*, *47*(11), 2075-2084.

[129] Pendry, J. B. (2007, June). Metamaterials and the control of electromagnetic fields. In *Conference on coherence and quantum optics* (p. CMB2). Optica Publishing Group.

[130] Engheta, N., & Ziolkowski, R. W. (Eds.). (2006). *Metamaterials: physics and engineering explorations*. John Wiley & Sons.

[131] Engheta, N. (2002). Ideas for potential applications of metamaterials with negative permittivity and permeability. In *Advances in Electromagnetics of Complex Media and Metamaterials* (Vol. 89, pp. 19-37). NATO Science.

[132] Engheta, N. (2002). An idea for thin subwavelength cavity resonators using metamaterials with negative permittivity and permeability. *IEEE Antennas and wireless propagation letters*, *1*, 10-13.

[133] Engheta, N., & Ziolkowski, R. W. (2005). A positive future for double-negative metamaterials. *IEEE Transactions on microwave theory and techniques*, *53*(4), 1535-1556.

[134] Alù, A., & Engheta, N. (2004). Guided modes in a waveguide filled with a pair of single-negative (SNG), double-negative (DNG), and/or double-positive (DPS) layers. *IEEE Transactions on Microwave Theory and Techniques*, *52*(1), 199-210.

[135] Pendry, J. B. (2000). Negative refraction makes a perfect lens. *Physical review letters*, *85*(18), 3966.

[136] Veselago, V. G. (1967). Electrodynamics of substances with simultaneously negative and. *Usp. fiz. nauk*, *92*(7), 517.

[137] Kuester, E. F., Mohamed, M. A., Piket-May, M., & Holloway, C. L. (2003). Averaged transition conditions for electromagnetic fields at a metafilm. *IEEE Transactions on Antennas and Propagation*, *51*(10), 2641-2651.

[138] Cai, W., & Shalaev, V. M. (2010). *Optical metamaterials* (Vol. 10, No. 6011). New York: Springer.

[139] Yu, N., & Capasso, F. (2014). Flat optics with designer metasurfaces. *Nature materials*, *13*(2), 139-150.

[140] Holloway, C. L., Kuester, E. F., Gordon, J. A., O'Hara, J., Booth, J., & Smith, D. R. (2012). An overview of the theory and applications of metasurfaces: The two-dimensional equivalents of metamaterials. *IEEE antennas and propagation magazine*, *54*(2), 10-35.

[141] Yoon, G., Kim, I., & Rho, J. (2016). Challenges in fabrication towards realization of practical metamaterials. *Microelectronic Engineering*, *163*, 7-20.

[142] Meinzer, N., Barnes, W. L., & Hooper, I. R. (2014). Plasmonic meta-atoms and metasurfaces. *Nature photonics*, *8*(12), 889-898.

[143] Kildishev, A. V., Boltasseva, A., & Shalaev, V. M. (2013). Planar photonics with metasurfaces. *Science*, *339*(6125), 1232009.

[144] Brorson, S. D., & Haus, H. A. (1988). Diffraction gratings and geometrical optics. *JOSA B*, *5*(2), 247-248.

[145] Gelman, D., & Spruch, L. (1969). Feynman Path Integrals and Scattering Theory. *Journal of Mathematical Physics*, *10*(12), 2240-2254.

[146] Albooyeh, M., Simovski, C., & Tretyakov, S. (2016, April). Homogenization and characterization of metasurfaces: General framework. In *2016 10th European Conference on Antennas and Propagation (EuCAP)* (pp. 1-3). IEEE.

[147] Holloway, C. L., & Kuester, E. F. (2016). A homogenization technique for obtaining generalized sheet-transition conditions for a metafilm embedded in a magnetodielectric interface. *IEEE Transactions on Antennas and Propagation*, *64*(11), 4671-4686.

[148] Glybovski, S. B., Tretyakov, S. A., Belov, P. A., Kivshar, Y. S., & Simovski, C. R. (2016). Metasurfaces: From microwaves to visible. *Physics reports*, *634*, 1-72.

[149] Pfeiffer, C., & Grbic, A. (2013). Metamaterial Huygens' surfaces: tailoring wave fronts with reflectionless sheets. *Physical review letters*, *110*(19), 197401.

[150] Monticone, F., Estakhri, N. M., & Alu, A. (2013). Full control of nanoscale optical transmission with a composite metascreen. *Physical review letters*, *110*(20), 203903.

[151] Yu, Q., Lian, J., Siriponglert, S., Li, H., Chen, Y. P., & Pei, S. S. (2008). Graphene segregated on Ni surfaces and transferred to insulators. *Applied physics letters*, *93*(11), 113103.

[152] Zhang, Y. I., Zhang, L., & Zhou, C. (2013). Review of chemical vapor deposition of graphene and related applications. *Accounts of chemical research*, *46*(10), 2329-2339.

[153] Seah, C. M., Chai, S. P., & Mohamed, A. R. (2014). Mechanisms of graphene growth by chemical vapour deposition on transition metals. *Carbon*, *70*, 1-21.

[154] Munoz, R., & Gómez-Aleixandre, C. (2013). Review of CVD synthesis of graphene. *Chemical Vapor Deposition*, *19*(10-11-12), 297-322.

[155] Kim, K. S., Zhao, Y., Jang, H., Lee, S. Y., Kim, J. M., Kim, K. S., ... & Hong, B. H. (2009). Large-scale pattern growth of graphene films for stretchable transparent electrodes. *nature*, *457*(7230), 706-710.

[156] Li, X., Cai, W., An, J., Kim, S., Nah, J., Yang, D., ... & Ruoff, R. S. (2009). Large-area synthesis of high-quality and uniform graphene films on copper foils. *science*, *324*(5932), 1312-1314.

[157] Coraux, J., N 'Diaye, A. T., Busse, C., & Michely, T. (2008). Structural coherency of graphene on Ir (111). *Nano letters*, *8*(2), 565-570.

[158] Kim, H. W., Song, I., Kim, T. H., Ahn, S. J., Shin, H. C., An, B. S., ... & Ahn, J. R. (2018). Millimeter-Scale Growth of Single-Oriented Graphene on a Palladium Silicide Amorphous Film. *ACS nano*, *13*(2), 1127-1135.

[159] Sutter, P. W., Flege, J. I., & Sutter, E. A. (2008). Epitaxial graphene on ruthenium. *Nature materials*, *7*(5), 406-411.

[160] Sutter, P., Sadowski, J. T., & Sutter, E. (2009). Graphene on Pt (111): Growth and substrate interaction. *Physical Review B*, *80*(24), 245411.

[161] Varykhalov, A., & Rader, O. (2009). Graphene grown on Co (0001) films and islands: Electronic structure and its precise magnetization dependence. *Physical Review B*, *80*(3), 035437.

[162] Chen, S., Ji, H., Chou, H., Li, Q., Li, H., Suk, J. W., ... & Ruoff, R. S. (2013). Millimeter-size single-crystal graphene by suppressing evaporative loss of Cu during low pressure chemical vapor deposition. *Advanced Materials*, *25*(14), 2062-2065.

[163] Dutta, D., Hazra, A., Hazra, S. K., Das, J., Bhattacharyya, S., Sarkar, C. K., & Basu, S. (2015). Performance of a CVD grown graphene-based planar device for a hydrogen gas sensor. *Measurement Science and Technology*, *26*(11), 115104.

[164] Çiplak, Z., Yildiz, N., & Çalimli, A. (2015). Investigation of graphene/Ag nanocomposites synthesis parameters for two different synthesis methods. *Fullerenes, Nanotubes and Carbon Nanostructures*, *23*(4), 361-370.

[165] Zhao, Y., Zhan, L., Tian, J., Nie, S., & Ning, Z. (2011). Enhanced electrocatalytic oxidation of methanol on Pd/polypyrrole–graphene in alkaline medium. *Electrochimica Acta*, *56*(5), 1967-1972.

[166] Shah, J., Jan, M. R., & Rahman, I. (2020). Dispersive solid phase microextraction of fenoxaprop-p-ethyl herbicide from water and food samples using magnetic graphene composite. *Journal of Inorganic and Organometallic Polymers and Materials*, *30*, 1716-1725.

[167] Naebe, M., Wang, J., Amini, A., Khayyam, H., Hameed, N., Li, L. H., ... & Fox, B. (2014). Mechanical property and structure of covalent functionalised graphene/epoxy nanocomposites. *Scientific reports*, *4*(1), 4375.

[168] Tang, Y., Guo, H., Xiao, L., Yu, S., Gao, N., & Wang, Y. (2013). Synthesis of reduced graphene oxide/magnetite composites and investigation of their adsorption performance of fluoroquinolone antibiotics. *Colloids and Surfaces A: Physicochemical and Engineering Aspects*, *424*, 74-80.